Microscopic theory of antiferromagnetic spin dynamics driven by magnetic field and electric current

Jotaro J Nakane

Nagoya University
Department of Physics
Japan

July 7, 2021

Publications

The main chapters of this thesis are based on the following works

- Chapter 2:
  J. J. Nakane and H. Kohno, *Magnetic-Field-Driven Antiferromagnetic Domain Wall Motion*, J. Phys. Soc. Japan **90**, 034702 (2021).

- Chapter 3:
  J. J. Nakane and H. Kohno, *Microscopic calculation of spin torques in textured antiferromagnets*, Phys. Rev. B **103**, L180405 (2021).

- Chapter 4:
  J. J. Nakane and H. Kohno, *Current-induced spin-wave Doppler shift in antiferromagnets*, Submitted to J. Phys. Soc. Japan.

Other publications that are not covered in this thesis

- J. J. Nakane and H. Kohno, *Angular momentum of phonons and its application to single-spin relaxation*, Phys. Rev. B **97**, 174403 (2018).

- J. J. Nakane, K. Nakazawa, and H. Kohno, *Topological Hall effect in weakly canted antiferromagnets*, Phys. Rev. B **101**, 174432 (2020).

My contribution to the papers.— As the first author, I have contributed significantly to all the parts of the papers. I am responsible for majority of the analytical work, numerical calculations, and figures. Compiling numerous discussions held with my co-authors, I have written most of the text in the papers.

Contents

Chapter 1

Introduction

1.1 Introduction

The key to modern human civilization lies, arguably, in the ability to exchange, store, and process information. Even before the common era, humans used to engrave texts on stones, presumably as a means of storing and communicating information. After the invention of letterpress printing in 15th century, paper become a major media for information storage. Analog recordings of sound and images were made available in the 19th and 20th century, and computers started to be developed around mid 20th century. The information age began and humans became capable of handling larger amounts of data. Computer chips are now so densely packed that we are now facing an inevitable challenge of quantum tunneling [1]. Another major issue is the energy consumption of computers; the amount of electricity used by large IT companies is comparable to the electricity consumption of whole nations [1]. We are now in desperate need for next generation computer devices that are more reliable and energy efficient.

Conventional computer components rely on electric charge as information bits, and are therefore by its very nature vulnerable to electric perturbations such as ionizing radiations. Spintronics was developed to overcome inherent weaknesses in electronics by exploiting the spin degrees of freedom

[1]Today, we have personalised computers that can compute 5×10^9 instructions per second. At such high frequencies, even light cannot travel further than 10cm during a cycle, so silicone based IC chips cannot be larger than a few cm^2. The chip components must therefore be packed as densely as possible, and modern day processors have their wirings less than ten nanometers apart.

in electrons. Spintronics based their development on ferromagnetic materials, and devices such as the racetrack memory [2] and magnetoresistive random access memories (MRAMs) were proposed. MRAMs have proven themselves useful in equipments that need high reliability such as aircraft and cars [3]. Although ferromagnetic memory devices are immune to electrical perturbations, they are weak against magnetic perturbations because information must be stored in the orientation of magnetization. Hence, recently researchers in the field of spintronics are starting to focus more on antiferromagnetic materials, because of their immunity to both electric and magnetic perturbations. Antiferromagnetic materials have additional advantages over ferromagnets, such as the versatility of materials and fast spin dynamics [4, 5, 6, 7, 8].

The immunity of antiferromagnets to external perturbations is a double-edged blade, because it makes the manipulation and detection of spin orientation extremely challenging. Observing antiferromagnetic spins is hard because they do not produce any stray fields, and are not accompanied by macroscopic angular momentum. Another reason why antiferromagnets are hard to tackle is because of the lack of an elucidating theoretical backbone. The number of theoretical calculations in antiferromagnets are scarce compared to ferromagnetic ones, mainly due to two reasons: first, a proper theoretical treatment of antiferromagnets necessitates the consideration of at least two sublattices which makes the theory more complicated, and second, macroscopic spin conservation arguments that were applicable in ferromagnets are absent in antiferromagnets. The goal of this thesis to establish a firm theoretical framework that allows for a better understanding of the dynamics of antiferromagnetic spins, and the means to control them.

In the body of this thesis, we explore different ways to manipulate antiferromagnetic spins. Chapter 2 of this thesis is concerned about the effect of magnetic fields on antiferromagnets, since magnetic field is the most fundamental external perturbation to manipulate magnetic materials. We show that inhomogeneous magnetic fields are capable of moving antiferromagnetic spin textures. Chapters 3 and 4 discusses the effect of conduction electrons on antiferromagnetic spins. Manipulation of spins using electrical currents is ideal from a scalability perspective. In chapter 3, we develop a theory that studies the motion of antiferromagnetic spin textures induced by conduction electrons. Quantum field theory is used for the treatment of conduction electrons. In chapter 4, the effect of conduction electrons on antiferromagnetic spin waves is explored, and the differences to ferromagnets is discussed in

detail. A short summary is given in chapter 5.

1.2 Spin dynamics

Before diving into antiferromagnets, we first go over the basics of spin dynamics. We show here the "derivation" of the Lagrangian of a single spin in the framework of classical mechanics. Consider a rigid body with cylindrical symmetry. Ignoring its translational motion, the Lagrangian for its orientational degrees of freedom can be written as

$$L = \frac{I_1}{2}(\dot{\theta}^2 + \dot{\phi}^2 \sin^2\theta) + \frac{I_3}{2}(\dot{\psi} + \dot{\phi}\cos\theta)^2 - H(\theta, \phi) \tag{1.1}$$

where I_1 and I_3 are moments of inertia orthogonal and parallel to the symmetry axis, θ and ϕ specify the orientation, and ψ is the angle around the symmetry axis. The dot represents a time derivative, and H denotes the potential energy. Now, let us shrink this cylinder to an infinitesimal size while retaining a constant angular momentum along the symmetry axis, i.e. I_1, $I_3 \to 0$ and $I_3\dot{\psi} = \hbar S$, just like an electron. Then, the Lagrangian takes the form

$$L = \hbar S\dot{\phi}\cos\theta - H(\theta, \phi) \tag{1.2}$$

where $\frac{(\hbar S)^2}{2I_3}$ has been dropped because it is a constant. This is nothing but the Lagrangian of a single spin [9]. From this Lagrangian, the equation of motion of the spin is derived as

$$\hbar\dot{\boldsymbol{S}} = \frac{\partial H}{\partial \boldsymbol{S}} \times \boldsymbol{S} \tag{1.3}$$

which describes the precession of the spin around an effective field $\frac{\partial H}{\partial \boldsymbol{S}}$.

One of the main missions of spintronics is to take full control of this equation of motion, and the most straight forward method is by using magnetic field. As it has been demonstrated by the Einstein-de Haas effect and Barnett effect [2], charged particles with spin give rise to magnetization. An

[2]Einstein-de Haas effect measured the change in mechanical angular momentum by changing the magnetization direction of a ferromagnet. The paper was published in 1915, before the discovery of electron spin in 1925. This experiment proved the connection between angular momentum and magnetization. Barnett effect is the inverse of the Einstein-de Haas effect.

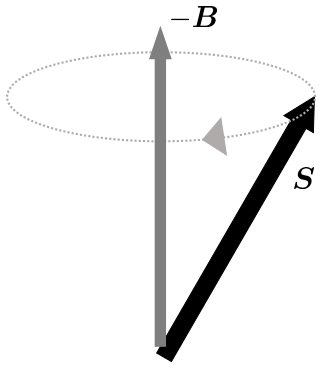

Figure 1.1: Illustration of a spin precessing around a magnetic field. Note that a spin likes to point opposite to the magnetic field.

electron spin couples to external magnetic field ($\boldsymbol{B}$) via the Zeeman coupling as

$$H_B = -\boldsymbol{\mu} \cdot \boldsymbol{B}, \tag{1.4}$$

$$\boldsymbol{\mu} = -g\mu_B \boldsymbol{S} = -\gamma\hbar \boldsymbol{S}, \tag{1.5}$$

where $\mu_B = e\hbar/(2m)$ is the Bohr magneton with $e > 0$ the elementary charge and m the particle mass. g is a dimensionless constant called the g-factor which is about 2.0023 for an electron in vacuum.

In quantum mechanics, the spin operator satisfies the commutation relation $[\hat{S}_i, \hat{S}_j] = i\varepsilon_{ijk}\hat{S}_k$ where ε_{ijk} is the Levi-Civita tensor. Using the Heisenberg equation of motion $i\hbar(d\hat{\boldsymbol{S}}/dt) = [\hat{\boldsymbol{S}}, \hat{H}]$, the equation of motion for a spin in a magnetic field (described by $\hat{H} = \hat{H}_B$) is given by

$$\frac{d}{dt}\hat{\boldsymbol{S}} = \gamma \boldsymbol{B} \times \hat{\boldsymbol{S}} \tag{1.6}$$

This describes the precession of a spin $\boldsymbol{S} = \langle\hat{\boldsymbol{S}}\rangle$ around the magnetic field $\boldsymbol{B}$, similar to the equation of a rotating cylinder (See Fig. 1.1).

1.2.1 Landau-Lifshitz-Gilbert equation

The precessional motion of the spin does not last forever in realistic systems, and some kind of damping is usually present. A phenomenological equation called the Landau-Lifshitz-Gilbert (LLG) equation is commonly used to

account for the relaxation of spins in realistic systems,

$$\frac{d}{dt}\hat{\boldsymbol{S}} = \gamma \boldsymbol{B} \times \hat{\boldsymbol{S}} - \frac{\alpha}{S}\Big(\boldsymbol{S} \times \frac{d}{dt}\boldsymbol{S}\Big) \tag{1.7}$$

where α is a dimensionless constant called the Gilbert damping constant. Note that the above equation of motion satisfies the constraint $\boldsymbol{S} \cdot \dot{\boldsymbol{S}} = 0$. With damping in consideration, the energy dissipation rate of a spin under magnetic field is given by

$$\frac{d}{dt}H_B = -\frac{\hbar\alpha}{S}\Big(\frac{d}{dt}\boldsymbol{S}\Big)^2 + O(\alpha^2) \tag{1.8}$$

so we have confirmed the Gilbert damping dissipates energy.

To account for damping in the Lagrangian formalism, one considers the Rayleigh dissipation function

$$W = \frac{\hbar\alpha}{2S}\Big(\frac{d}{dt}\boldsymbol{S}\Big)^2 \tag{1.9}$$

and calculate the equation of motion

$$\left(\frac{d}{dt}\frac{\delta L}{\delta \dot{\boldsymbol{S}}} - \frac{\delta L}{\delta \boldsymbol{S}} + \frac{\delta W}{\delta \dot{\boldsymbol{S}}}\right) \times \boldsymbol{S} = 0 \tag{1.10}$$

to retrieve the LLG equation [3]. The external product $\times \boldsymbol{S}$ ensures $\boldsymbol{S}$ does not change in length.

1.2.2 Ferromagnets

Let us now consider an array of spins that are interacting with each other. Though various types of interactions exist, here we consider the ferromagnetic exchange interaction dominant; this is described by the Hamiltonian

$$H_F = -J_F \sum_{\langle i,j \rangle} \boldsymbol{S}_i \cdot \boldsymbol{S}_j \tag{1.11}$$

where $J_F > 0$ is the ferromagnetic exchange constant and $\boldsymbol{S}_i$ is a localized spin placed at site i on the lattice. The summation, $\langle i, j \rangle$, is taken over the nearest neighboring sites. This Hamiltonian achieves lower energy when

[3] Note the relation $dH/dt = -2W$.

neighboring spins are parallel to each other (see Fig.1.2 (a)). With the ferromagnetic interaction dominating, the texture of spins in a ferromagnet can be considered relatively smooth, so we can employ the continuum approximation by $\boldsymbol{S}_i \cdot \boldsymbol{S}_j = -\frac{1}{2}(\boldsymbol{S}_i - \boldsymbol{S}_j)^2 + S^2 \simeq -\frac{1}{2}(\boldsymbol{a}_{ij} \cdot \nabla \boldsymbol{S})^2 + S^2$ where $\boldsymbol{a}_{ij}$ is a vector connecting the two sites i and j. The ferromagnetic exchange Hamiltonian in d-dimensions is written in the continuum limit as

$$H_F = \frac{J_F a^2}{2} \sum_i^d \int \frac{d^d r}{a^d} (\partial_i \boldsymbol{S})^2 \tag{1.12}$$

where a is the distance between the two nearest neighbors.

Although the ferromagnetic exchange interaction is adequate to make all spins point in the same direction via the spontaneous symmetry breaking, this cannot describe realistic magnets, since the spins have no way to know its orientation relative to the crystal lattice. (The needle of the compass must rotate with the magnetization.) This is accounted for by the magnetic anisotropy, often described by

$$H_K = -\frac{K}{2} \sum_i (S_i^z)^2, \tag{1.13}$$

where $K > 0$ is the anisotropy constant, and we chose the z axis to be the easy axis [4]. The microscopic origin of magnetic anisotropy lies in the spin-orbit coupling and magnetic dipole-dipole interaction. With the easy axis anisotropy, the ground state of the ferromagnet is achieved by pointing all spins in the positive (or negative) z direction.

With the anisotropy Hamiltonian, the equation of motion of the ferromagnetic spins is given by

$$\hbar \dot{\boldsymbol{S}} = -J_F a^2 (\nabla^2 \boldsymbol{S}) \times \boldsymbol{S} - K S^z \hat{z} \times \boldsymbol{S} \tag{1.14}$$

Let us solve this ferromagnetic spin equation of motion using the small amplitude method. That is, we assume the ferromagnetic spins to point mostly in the z direction, and consider the small deviation from it as $\boldsymbol{S} =$

[4] One also has the freedom to choose a hard axis, $H_{K'} = \frac{K'}{2} \sum_i (S_i^y)^2$, with $K' > 0$. This is also called the easy plane, because the spins happily point anywhere orthogonal to the hard axis. Other anisotropies that are not covered include magnetic shape anisotropy, which comes from the magnetic dipole-dipole interaction and is the dominant anisotropy in permalloy.

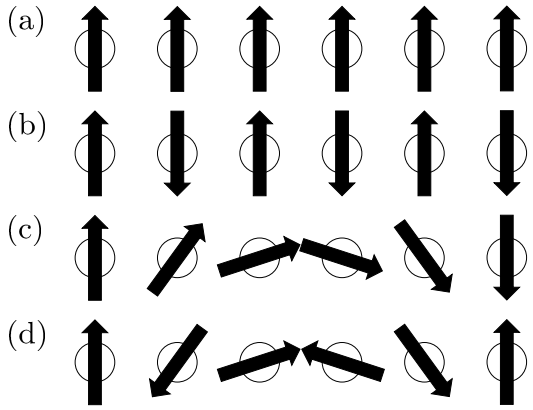

Figure 1.2: Illustration of various magnetic structures. (a) Uniform ferromagnet. (b) Uniform antiferromagnet. (c) A ferromagnetic domain wall. (d) An antiferromagnetic domain wall.

$S\hat{z} + \delta\boldsymbol{n}e^{i\boldsymbol{q}\cdot\boldsymbol{r}-i\omega t}$. To first order in $\delta\boldsymbol{n}$ ($\perp \hat{z}$), one obtains the equation of motion

$$-i\hbar\omega\delta\boldsymbol{n} = (J_F S a^2 q^2 + KS)\delta\boldsymbol{n} \times \hat{z}. \tag{1.15}$$

This equation of motion describes spin waves, which is the small precession of spins that propagate through the ferromagnet. The dispersion relation is given by a parabola

$$\hbar\omega = J_F S a^2 q^2 + KS. \tag{1.16}$$

This is known as the ferromagnetic spin wave dispersion relation. Note that the anisotropy constant gives rise to a gap in the spin wave dispersion.

1.2.3 Antiferromagnets

Changing the sign of the ferromagnetic exchange constant, one has the antiferromagnetic exchange interaction described by the following Hamiltonian

$$H_{AF} = J\sum_{\langle i,j\rangle} \boldsymbol{S}_i \cdot \boldsymbol{S}_j \tag{1.17}$$

where $J > 0$ is the antiferromagnetic exchange constant. This Hamiltonian achieves lowest energy when neighboring spins are aligned opposite to each

other (see Fig. 1.2 (b)). A detailed derivation of the antiferromagnetic spin equation of motion with anisotropy and magnetic field is given in chapter 2. The effect of electric current on the antiferromagnetic spins is discussed in chapters 3 and 4.

1.3 Spin textures

In the previous section, we have studied spin waves, which are the collective low-energy excitations of localized spins.

In this section, we look at another type of excitation in ferromagnets called domain walls (See Fig. 1.2 (c)). Domain walls are anticipated to play a crucial role in spintronic devices, for example as memory bits in race-track memories [2]. A domain wall solution can be obtained by solving the equation of motion of ferromagnetic spins in the static case.

$$\left(J_F a^2(\nabla^2 \boldsymbol{S}) + KS^z\hat{z}\right) \times \boldsymbol{S} = 0, \tag{1.18}$$

or

$$\lambda^2\nabla^2\theta - \sin\theta\cos\theta(1+\lambda^2(\nabla\phi)^2) = 0 \tag{1.19}$$

$$\sin\theta\nabla^2\phi + 2\cos\theta(\nabla\theta)(\nabla\phi) = 0 \tag{1.20}$$

where we wrote $\boldsymbol{S} = S\boldsymbol{n} = S(\sin\theta\cos\phi,\, \sin\theta\sin\phi,\, \cos\theta)$, and $\lambda = \sqrt{J_F a^2/K}$. A trivial solution is $\boldsymbol{S} = \pm S\hat{z}$. This is the lowest energy state of the Hamiltonian. A non-trivial solution with $\nabla\phi = 0$ and the only spatial variation in the x direction (i.e. $\partial_x\theta \neq 0$), also with a boundary condition $\boldsymbol{S}(x = \pm\infty) = \pm S\hat{z}$, is given by

$$\cos\theta = \tanh[(x-X)/\lambda], \quad \sin\theta = 1/\cosh[(x-X)/\lambda]. \tag{1.21}$$

This describes a ferromagnetic domain wall with domain wall width λ located at position X. Note that the magnetic anisotropy is essential for the domain wall to stabilise. Large magnetic anisotropy (or small exchange interaction) results in a shorter domain wall width, and vice versa.

1.4 Conduction electrons and the s-d model

Let us demonstrate in this section the basics of the treatment of conduction electrons, and model their interactions with ferromagnetic spins.

1.4.1 Electrical conductivity

In this thesis, all conduction electrons are considered in the tight-binding Hamiltonian

$$H_{\rm el} = -t \sum_{\langle i,j \rangle} \Big[c_i^\dagger c_j + \text{H.c.} \Big] + V_{\rm imp} \tag{1.22}$$

where t is the hopping integral, $c_i^\dagger = (c_{i,\uparrow}^\dagger, c_{i,\downarrow}^\dagger)$ is the electron creation operator at site i, and $V_{\rm imp}$ is the impurity potential. The kinetic energy part of this Hamiltonian can be solved by Fourier transformation

$$c_i = \sqrt{\frac{1}{N}} \sum_{\boldsymbol{k}} c_{\boldsymbol{k}} e^{i \boldsymbol{r}_i \cdot \boldsymbol{k}}, \quad c_j^\dagger = \sqrt{\frac{1}{N}} \sum_{\boldsymbol{k}} c_{\boldsymbol{k}}^\dagger e^{-i \boldsymbol{r}_j \cdot \boldsymbol{k}} \tag{1.23}$$

as

$$H_{\rm el} = \sum_{\boldsymbol{k}} c_{\boldsymbol{k}}^\dagger \varepsilon_{\boldsymbol{k}} c_{\boldsymbol{k}} + V_{\rm imp} \tag{1.24}$$

where $\varepsilon_{\boldsymbol{k}} = -2t \sum_{l=1}^{d} \cos(a k_l)$ for a d-dimensional lattice, where a is the distance to the nearest neighboring sites, and d the number of dimensions. The summation $\boldsymbol{k}$ is taken over the Brillouin zone. The dispersion relation of tight binding electrons in a 2-dimensional square lattice is given by $\varepsilon_{\boldsymbol{k}} = -2t[\cos(a k_x) + \cos(a k_y)]$.

Let us from now on consider a 1-dimensional system for simplicity. With the local charge density operator $n_i = -e c_i^\dagger c_i$ with $e > 0$, and the continuity equation $\dot{n}_i = i[H_{\rm el}, n_i] = -(j_{i+1} - j_i)$, we define the current operator as $j_i = it(-e)(c_i^\dagger c_{i-1} - c_{i-1}^\dagger c_i)$. The total current $J = \sum_i j_i$ in Fourier representation is given by

$$J = -e \sum_k c_k^\dagger (\partial_k \varepsilon_k) c_k. \tag{1.25}$$

The total electrical conductivity can be derived using the Kubo formula as

$$N\sigma = \lim_{\omega \to 0} \frac{K^R(\omega) - K^R(0)}{i\omega} \tag{1.26}$$

with

$$K^R(\omega) = i \int_0^\infty dt\, e^{i(\omega + i0)t} \langle [J(t), J(0)] \rangle. \tag{1.27}$$

The average is taken with $H_{\rm el}$ as $\langle(\cdots)\rangle = {\rm tr}[(\cdots)\exp(-\beta H_{\rm el})]\,/\,{\rm tr}[\exp(-\beta H_{\rm el})]$. Using the Green's functions for the conduction electrons, the conductivity can be written as

$$\sigma = \frac{1}{\pi}\frac{1}{N}\sum_{\boldsymbol{k}}(2te\sin k_x)^2 G^R G^A \tag{1.28}$$

where the Green's functions are given by $G^R = 1/(\mu - \varepsilon_{\boldsymbol{k}} + i\gamma)$ and $G^A = (G^R)^*$. μ is the chemical potential of the conduction electrons, and $\gamma = (2\tau)^{-1} > 0$ is the damping constant for which we shall see the derivation later. The electrical conductivity is calculated by approximating the Lorentzian as a delta function ($G^R G^A = \frac{\pi}{\gamma}\delta(\mu - \varepsilon_{\boldsymbol{k}})$), and we finally get our hands on the conductivity

$$\sigma = 2e^2 D\nu \tag{1.29}$$

where $D = \langle v_F^2\rangle\tau/d = \nu^{-1}\frac{1}{N}\sum_{\boldsymbol{k}}[(2t\sin k_x)^2]\delta(\mu - \varepsilon_{\boldsymbol{k}})\tau$ is the diffusion constant, and $\nu = \frac{1}{N}\sum_{\boldsymbol{k}}\delta(\mu - \varepsilon_{\boldsymbol{k}})$ is the density of states per spin. The factor 2 accounts for the spin degeneracy.

1.4.2 Born approximation

In this section, we go over the treatment of the impurity potential $V_{\rm imp}$, and determine the expression of the damping constant γ. For electric conductivity, it suffices to only consider non-magnetic point-like impurities

$$V_{\rm imp} = u_{\rm i}\sum_{i\in C} c_i^\dagger c_i \tag{1.30}$$

where C is a set of indices the impurities are placed at. The Fourier transformation gives

$$V_{\rm imp} = u_{\rm i}\sum_{\boldsymbol{k},\boldsymbol{q}} \rho_{\boldsymbol{q}} c_{\boldsymbol{k}}^\dagger c_{\boldsymbol{k}-\boldsymbol{q}} \tag{1.31}$$

with $\rho_{\boldsymbol{q}} = \frac{1}{N}\sum_{i\in C} e^{-i\boldsymbol{r}_i\cdot\boldsymbol{q}}$. Finite $\boldsymbol{q}$ implies that $V_{\rm imp}$ breaks translational symmetry. Performing an impurity average defined by $\langle(\cdots)\rangle_{\rm imp} = \frac{1}{{}_N C_{N_{\rm i}}}\sum_C(\cdots)$ recovers translational symmetry. The summation $\sum_C$ is performed over all the possible sets of indices for the position of impurity potentials, $N_{\rm i}$ is the

total number of impurities, and ${}_NC_{N_\mathrm{i}}$ is the number of possible combinations the impurities can be placed. Note that $\langle 1 \rangle_{\mathrm{imp}} = 1$, and

$$\langle \rho_{\boldsymbol{q}} \rangle_{\mathrm{imp}} = n_\mathrm{i} \delta_{\boldsymbol{q},0}, \tag{1.32}$$

$$\langle \rho_{\boldsymbol{q}} \rho_{\boldsymbol{q}'} \rangle_{\mathrm{imp}} \simeq \frac{n_\mathrm{i} - (n_\mathrm{i})^2}{N} \delta_{\boldsymbol{q}+\boldsymbol{q}',0} + (n_\mathrm{i})^2 \delta_{\boldsymbol{q},0} \delta_{\boldsymbol{q}',0} \tag{1.33}$$

$$\simeq \frac{n_\mathrm{i}}{N} \delta_{\boldsymbol{q}+\boldsymbol{q}',0} \tag{1.34}$$

where $n_\mathrm{i} = N_i/N$ is the impurity density (See Fig. 1.3) [5]. For the first equality (Eq. (1.33)) we wrote $\frac{N_\mathrm{i}(N_\mathrm{i}-1)}{N(N-1)} \simeq (n_\mathrm{i})^2$, and in the second equality (Eq. (1.34)) we have dropped higher contributions in n_i. In the Born approximation, only the contribution of Eq. (1.34) is considered for the self energy as

$$\gamma = -n_\mathrm{i} u_\mathrm{i}^2 \frac{1}{N} \sum_{\boldsymbol{k}} \mathrm{Im}\, G^{0,R} \tag{1.35}$$

$$= n_\mathrm{i} u_\mathrm{i}^2 \pi \nu \tag{1.36}$$

where the bare retarded and advanced Green's functions are given by $G^{0,R/A} = 1/(\mu - \varepsilon_{\boldsymbol{k}} \pm i0)$.

1.4.3 s-d exchange interaction

In chapters 3 and 4 of this thesis, we deal with antiferromagnetic metals that is composed of conduction electrons and localized antiferromagnetic spins. The interaction between the conduction electrons and localized spins is described by the s-d exchange interaction [6], which is written as the inner

[5] For the second order perturbation of the impurity potential, we need $\langle \rho_{\boldsymbol{q}} \rho_{\boldsymbol{q}'} \rangle_{\mathrm{imp}} = \frac{1}{{}_NC_{N_\mathrm{i}}} \sum_C \frac{1}{N^2} \left(\sum_{i \in C} e^{-i\boldsymbol{r}_i \cdot (\boldsymbol{q}+\boldsymbol{q}')} + \sum_{i \in C} \sum_{j(\neq i) \in C} e^{-i\boldsymbol{r}_i \cdot \boldsymbol{q} - i\boldsymbol{r}_j \cdot \boldsymbol{q}'} \right)$. In the first term, we have taken the same impurities from $\rho_{\boldsymbol{q}}$ and $\rho_{\boldsymbol{q}'}$, and in the second term we two different impurities. The second term equates to $\frac{N_\mathrm{i}(N_\mathrm{i}-1)}{N(N-1)} \frac{1}{N^2} \sum_i e^{-i\boldsymbol{r}_i \cdot \boldsymbol{q}} \left[\left\{ \sum_j e^{-i\boldsymbol{r}_j \cdot \boldsymbol{q}'} \right\} - e^{-i\boldsymbol{r}_i \cdot \boldsymbol{q}'} \right]$ which becomes $\frac{N_\mathrm{i}(N_\mathrm{i}-1)}{N(N-1)} \left[\delta_{\boldsymbol{q},0} \delta_{\boldsymbol{q}',0} - \frac{1}{N} \delta_{\boldsymbol{q}+\boldsymbol{q}',0} \right] \simeq (n_\mathrm{i})^2 \left[\delta_{\boldsymbol{q},0} \delta_{\boldsymbol{q}',0} - \frac{1}{N} \delta_{\boldsymbol{q}+\boldsymbol{q}',0} \right]$

[6] The s-d exchange interaction models the interaction between 3d orbital electrons and 4s orbital electrons, and is useful for understanding 3d transition metals. The electrons in the 3d orbital is assumed to give rise to the localized spins (magnetization), while only the 4s electrons are made responsible for electrical conductivity. The microscopic origin of the interaction is quantum, and comes from exchanging electrons. The strength of

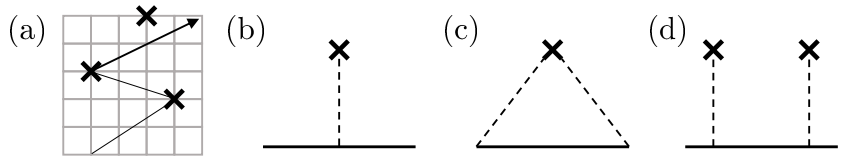

Figure 1.3: (a) Illustration of an electron scattered by impurities. (b) Feynman diagram representing the impurity average Eq. (1.32). (c) Feynman diagram representing the first term in Eq. (1.33). This is what will be considered in the Born approximation. A wave-vector summation is taken for the Green's function sandwiched by the impurity lines. (c) Feynman diagram representing the second term in Eq. (1.33).

product between the localized spins and conduction electron spins,

$$H_{\rm sd} = -J_{\rm sd} \sum_i \boldsymbol{S}_i \cdot c_i^\dagger \boldsymbol{\sigma} c_i \tag{1.37}$$

where $\boldsymbol{\sigma} = (\sigma^x, \sigma^y, \sigma^z)$ is a vector of Pauli matrices.

s-d interaction with ferromagnets When conduction electrons interact with a static and spatially uniform ferromagnetic background, the conduction electron has the Hamiltonian

$$H_0 = -t \sum_{\langle i,j \rangle} \Big[c_i^\dagger c_j + \text{H.c.} \Big] - J_{\rm sd} S \sum_i c_i^\dagger \sigma^z c_i + V_{\rm imp} \tag{1.38}$$

where the direction parallel to the ferromagnetic spins is chosen as the z axis. The dispersion relation is given by $\varepsilon_{\boldsymbol{k}} \pm J_{\rm sd} S$, where $\pm$ corresponds to the minority and majority spin electrons. See Fig. 1.4 for a graph of the dispersion relation, where one sees that the spin degeneracy is lifted due to the s-d exchange interaction.

s-d interaction with Antiferromagnets For antiferromagnets, the s-d exchange interaction is written as

$$H_{0,FM} = -t \sum_{\langle i,j \rangle} \Big[c_i^\dagger c_j + \text{H.c.} \Big] - J_{\rm sd} S \sum_i (-)^i c_i^\dagger \sigma^z c_i + V_{\rm imp} \tag{1.39}$$

---

the s-d exchange interaction is thought to be larger than 0.1eV [3]. (Although 3d orbital electrons are also responsible for electrical conductivity in reality, the s-d model suffices to understand the essence of metallic ferro and antiferromagnets.)

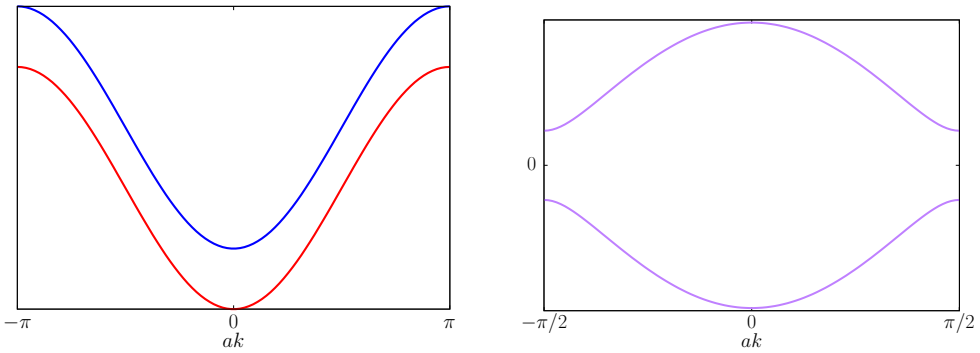

(a) Ferromagnetic (b) Antiferromagnetic

Figure 1.4: (a) Dispersion relation of conduction electrons interacting with ferromagnetic spins. The spin degeneracy is lifted because of the s-d exchange interaction. (b) Dispersion relation of 1-dimensional conduction electrons interacting with antiferromagnetic spins. The spin degeneracy is present and the electron band is two-fold degenerate. Also, the Brillouin is folded in half because of the larger unit-cell.

where $(-)^i$ is 1 when $i \in$ A sublattice (localized spin is pointing up), and -1 when $i \in$ B sublattice (localized spin is pointing down). The z axis is chosen along the direction of the localized spin at site A. To obtain the dispersion relation of this Hamiltonian, it is convenient to write the Hamiltonian in the sublattice representation

$$\begin{aligned} c_i = a_i &= \sqrt{\frac{2}{N}} \sum_{\boldsymbol{k}} a_{\boldsymbol{k}} e^{i\boldsymbol{r}_i \cdot \boldsymbol{k}}, \quad i \in \text{A sublattice} \\ c_i = b_i &= \sqrt{\frac{2}{N}} \sum_{\boldsymbol{k}} b_{\boldsymbol{k}} e^{i\boldsymbol{r}_i \cdot \boldsymbol{k}}, \quad i \in \text{B sublattice} \end{aligned} \tag{1.40}$$

where $2/N$ normalizes the summation, which is now taken over the reduced Brillouin zone. With this, the Hamiltonian can be written as

$$H_{0,AF} = \sum_{\boldsymbol{k}} \tilde{c}^{\dagger}_{\boldsymbol{k}} \Big[\varepsilon_{\boldsymbol{k}} \tau_x - J_{\text{sd}} S \sigma^z \tau_z \Big] \tilde{c}_{\boldsymbol{k}} + V_{\text{imp}} \tag{1.41}$$

where $\tilde{c}_{\boldsymbol{k}} = (a_{\boldsymbol{k}}, b_{\boldsymbol{k}})$, and τ_x, τ_z are Pauli matrices that act on the sublattice space. The dispersion relation of this Hamiltonian is given by $\pm E_{\boldsymbol{k}}$, where $E_{\boldsymbol{k}} = \sqrt{\varepsilon^2_{\boldsymbol{k}} + (J_{\text{sd}} S)^2}$ (See Fig. 1.4 (b)).

1.5 This thesis

Each chapter in this thesis is kept self-contained, and are organized as follows.

In chapter 2, we study the dynamics of antiferromagnetic spins under a magnetic field. We obtain the equation of motion of antiferromagnetic spins that corrects the ones derived in previous studies. Based on the obtained results, the dynamics of an antiferromagnetic domain wall under the influence of an inhomogeneous magnetic field is studied analytically. The domain wall motion predicted by our analytical equations are are verified by atomistic simulations.

In chapters 3 and 4 of this thesis, we discuss the effects of conduction electrons on antiferromagnetic spins. In chapter 3, we study the current induced spin torques in antiferromagnets. Despite the abundance in research on antiferromagnetic spin torques, the number of microscopic theories are miniscule. In this chapter, microscopic derivations of antiferromagnetic spin torques are given. Analytic expressions for the spin-transfer torque (for which the coefficient is denoted by $\boldsymbol{v}_n$), β-torque, and damping torques α_n, α_ℓ are derived. We further study the antiferromagnetic domain wall motion driven by an electrical current, and show that the domain wall velocity is opposite to the ferromagnetic case.

In chapter 4, we pursue the study on current induced spin torques in antiferromagnets. We show that the Doppler shift of antiferromagnetic spin waves (induced by spin-transfer torque) comes in two forms, expressed as $\boldsymbol{v}_n$ and $\boldsymbol{v}_\ell$. Microscopic calculations for the two spin-transfer torques are presented for electrons with nearest-neighbor (t) and next-nearest-neighbor (t') hopping considered (Fig. 1.5); the two hoppings interpolate the antiferromagnetic transport regime ($t'/t \ll 1$) and the ferromagnetic transport regime ($t'/t \gg 1$). Introduction of the two hoppings parameters allows us to study the smooth transition of the spin-transfer torque from the ferromagnetic regime to the antiferromagnetic regime. In the antiferromagnetic transport regime, $\boldsymbol{v}_n$ and $\boldsymbol{v}_\ell$ give opposite contributions, and $\boldsymbol{v}_\ell$ dominates around the antiferromagnetic band bottom while $\boldsymbol{v}_n$ dominates near the antiferromagnetic band gap edge. In the ferromagnetic transport regime, $\boldsymbol{v}_n$ and $\boldsymbol{v}_\ell$ coincide to form ferromagnetic spin-transfer torque.

This work is supported by JSPS KAKENHI Grant Numbers JP15H05702, JP17H02929 and JP19K03744. JJN is supported by a Program for Leading Graduate Schools "Integrative Graduate Education and Research in Green Natural Sciences" and Grant-in-Aid for JSPS Research Fellow Grant Number

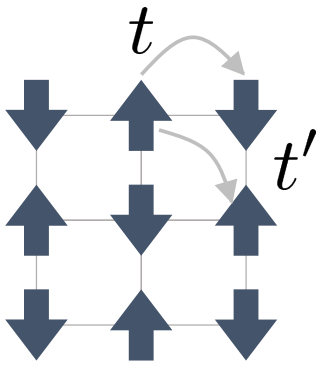

Figure 1.5: Illustration of conduction electrons hopping in a 2-dimensional antiferromagnetic lattice. The nearest-neighbor hopping t makes an electron jump from a site with up localized spin to a site with down localized spin (or vice versa), whereas the next-nearest-neighbor hopping t' connects the sites with the same direction of localized spins. When t dominates over t', it is called the antiferromagnetic transport regime, and the opposite is called the ferromagnetic transport regime.

19J23587.

Chapter 2

Magnetic-field-driven domain wall motion

In this chapter, we theoretically study the antiferromagnetic domain wall motion actuated by an inhomogeneous external magnetic field. First, we derive the Lagrangian and the equations of motion of antiferromagnetic spins with Zeeman coupling. Then, we obtain the equation of motion for an antiferromagnetic domain wall by using the method of collective coordinates. A solution is found that describes the actuation of a domain wall by an inhomogeneous field. The domain wall motion is initiated by a paramagnetic response of wall magnetization, which is then driven by a Stern-Gerlach like force. The effects of pinning potential are also investigated. These results are in good agreement with atomistic simulations. While the present formulation contains the so-called intrinsic magnetization associated with antiferromagnetic spin texture, a supplementary discussion is given to reformulate the theory in terms of physical magnetization without the intrinsic magnetization.

2.1 Introduction

This chapter explores the means to control antiferromagnetic spins using magnetic fields. Magnetic fields are one of the most fundamental perturbations used to control magnetic materials (modern hard-drives still rely on

external magnetic fields for writing information), so understanding their effect on antiferromagnetic spins is of fundamental importance. Although the effect of external magnetic field on uniform antiferromagnets is well understood, studies on textured antiferromagnets remain fairly limited. We focus on a specific antiferromagnetic texture, a domain wall, for its simplicity and applicational importance.

A domain wall is one of the topological objects in magnetic materials that may prove useful in memory devices, and its creation, manipulation and detection has been the scope in numerous studies. Some pioneering theoretical works show that antiferromagnetic domain walls can be driven by spin waves [10] and spin-orbit torques [11, 12]. Indirect experimental observations of antiferromagnetic domain wall motion are reported [13]. Domain walls in materials similar to antiferromagnets, such as synthetic antiferromagnets[14] and ferrimagnets around the angular momentum compensation temperature [15, 16], have also been studied, which allow for an easier observation and manipulation of domain walls.

It is known that ferromagnetic domain walls can be controlled with a uniform magnetic field [17], because one domain is energetically favoured over the other. In antiferromagnets however, different domains are degenerate under an applied magnetic field, so domain walls do not have an incentive to move. Recently, it was proposed that antiferromagnetic spin textures give rise to intrinsic magnetization [18]. It was demonstrated that this intrinsic magnetization couples to external magnetic fields, and may be used to actuate antiferromagnetic domain wall motion. In this chapter, we reinvestigate this problem starting from the same model. We found an additional coupling of the Néel vector to the inhomogeneous magnetic field, similar to the one in Ref. [19], which nullifies the effect of the above intrinsic magnetization. With the new Lagrangian obtained, we find an alternative mechanism for domain wall motion actuated by an inhomogeneous external magnetic field.

This chapter is organized as follows. After presenting in section 2 the Lagrangian and equations of motion for the antiferromagnetic order parameter (Néel vector) under an inhomogeneous magnetic field, we derive in section 3 the equations of motion in terms of collective coordinates of a domain wall. By solving the equations, we find a solution in which the domain wall position grows exponentially with time. Interestingly, there is no domain wall motion in the absence of damping. We also study the effects of pinning introduced by a local modulation of easy-axis magnetic anisotropy. Finally, we perform an atomistic simulation to test the analytical results, and see that they are

in good agreement. As a supplementary discussion, we identify the physical magnetization and reformulate the theory therewith.

2.2 Model

In this section, we derive an effective Lagrangian that describes low-frequency, long-wavelength spin dynamics of an antiferromagnet, starting from a lattice spin model. We closely follow the procedure described in Ref. [18], except that we consider the inhomogeneity of the external magnetic field from the beginning of the formulation.

2.2.1 Hamiltonian

We start with a Heisenberg Hamiltonian for classical spins on a one-dimensional lattice with antiferromagnetic exchange coupling $J > 0$, easy-axis anisotropy $K > 0$, and Zeeman coupling,

$$H = J\sum_i \boldsymbol{S}_i \cdot \boldsymbol{S}_{i+1} - K\sum_i (\boldsymbol{S}_i \cdot \boldsymbol{e}_z)^2 + \gamma\hbar \sum_i \boldsymbol{H}_i \cdot \boldsymbol{S}_i, \tag{2.1}$$

where γ is the gyromagnetic ratio. The localized spins and magnetic field at lattice site i are written as $\boldsymbol{S}_i$ and $\boldsymbol{H}_i$, respectively. In a typical easy-axis antiferromagnet, the exchange energy dominates $J \gg K$, giving rise to relatively thick domain walls (e.g. 150nm for NiO [20]). Therefore, we work in the exchange approximation $J \gg K$ (and $J \gg \gamma\hbar|H_i|$), and focus on spin textures with slow spatial/temporal variations.

Let us write the antiferromagnetic spins in terms of the Néel and uniform moments,

$$\boldsymbol{n}_n = \frac{\boldsymbol{S}_{2n} - \boldsymbol{S}_{2n+1}}{2S}, \qquad \boldsymbol{l}_n = \frac{\boldsymbol{S}_{2n} + \boldsymbol{S}_{2n+1}}{2S}, \tag{2.2}$$

respectively, where $|\boldsymbol{S}_i| = S$ is a constant. (i is the site index, and n is the unit-cell index.) The original spins are retrieved by

$$\boldsymbol{S}_{2n} = S(\boldsymbol{l}_n + \boldsymbol{n}_n), \quad \boldsymbol{S}_{2n+1} = S(\boldsymbol{l}_n - \boldsymbol{n}_n). \tag{2.3}$$

With $\boldsymbol{n}_n$ and $\boldsymbol{l}_n$, the Hamiltonian is written as $H = \sum_n h_n$, where

$$\begin{aligned} h_n = JS^2 \Bigg\{ & 2(\boldsymbol{l}_n^2 - \boldsymbol{n}_n^2) - \frac{(\boldsymbol{l}_n - \boldsymbol{l}_{n-1})^2}{2} + \frac{(\boldsymbol{n}_n - \boldsymbol{n}_{n-1})^2}{2} \\ & + (\boldsymbol{n}_n - \boldsymbol{n}_{n-1}) \cdot \boldsymbol{l}_n - \boldsymbol{n}_n \cdot (\boldsymbol{l}_n - \boldsymbol{l}_{n-1}) \Bigg\} \\ & - 2KS^2 \big\{ (l_n^z)^2 + (n_n^z)^2 \big\} \\ & + \gamma \hbar S \Big\{ (\boldsymbol{H}_{2n} + \boldsymbol{H}_{2n+1}) \cdot \boldsymbol{l}_n - (\boldsymbol{H}_{2n+1} - \boldsymbol{H}_{2n}) \cdot \boldsymbol{n}_n \Big\}. \end{aligned} \tag{2.4}$$

We adopt the continuum approximation and write $\boldsymbol{n}_n - \boldsymbol{n}_{n-1} \simeq 2a\partial_x \boldsymbol{n}$ and $\boldsymbol{l}_n - \boldsymbol{l}_{n-1} \simeq 2a\partial_x \boldsymbol{l}$, where a is the lattice constant. The magnetic field is also assumed slowly-varying (having no staggered component) and thus $\boldsymbol{H}_{2n} + \boldsymbol{H}_{2n+1} \simeq 2\boldsymbol{H}$, $\boldsymbol{H}_{2n+1} - \boldsymbol{H}_{2n} \simeq a\partial_x \boldsymbol{H}$, and the summation is replaced by an integration $\displaystyle\sum_n = \int \frac{dx}{2a}$. Thus the Hamiltonian is written as

$$\begin{aligned} H = JS^2 \int \frac{dx}{2a} \Bigg\{ & 2(\boldsymbol{l}^2 - \boldsymbol{n}^2) + \frac{(2a)^2}{2} \big[(\partial_x \boldsymbol{n})^2 - (\partial_x \boldsymbol{l})^2 \big] \\ & + (2a) \big[\boldsymbol{l} \cdot (\partial_x \boldsymbol{n}) - \boldsymbol{n} \cdot (\partial_x \boldsymbol{l}) \big] \Bigg\} \\ & - 2KS^2 \int \frac{dx}{2a} \big\{ (l^z)^2 + (n^z)^2 \big\} \\ & + \gamma \hbar S \int \frac{dx}{2a} \big\{ 2\boldsymbol{H} \cdot \boldsymbol{l} - a(\partial_x \boldsymbol{H}) \cdot \boldsymbol{n} \big\}. \end{aligned} \tag{2.5}$$

As we shall see later, $|\boldsymbol{l}| = O(a/\lambda)$ in the exchange approximation ($J \gg K$), where $\lambda = a\sqrt{J/2K}$ is the typical length scale of spatial variation. We discard the terms which are of higher order in l, such as $Kl^2 = O(Jl^4)$ and $(a\,\partial_x \boldsymbol{l})^2 = O(l^4)$. Using the constraints,

$$\boldsymbol{n}^2 + \boldsymbol{l}^2 = 1, \quad \boldsymbol{n} \cdot \boldsymbol{l} = 0, \tag{2.6}$$

or $\boldsymbol{n} \cdot \partial_x \boldsymbol{l} = -(\partial_x \boldsymbol{n}) \cdot \boldsymbol{l}$, which follow from $|\boldsymbol{S}_i| = \text{const.}$, we obtain

$$\begin{aligned} H \simeq 4JS^2 \int \frac{dx}{2a} & \left\{ \boldsymbol{l}^2 + \frac{a^2}{2} (\partial_x \boldsymbol{n})^2 + a\,\boldsymbol{l} \cdot (\partial_x \boldsymbol{n}) - \frac{K}{2J} (n^z)^2 \right\} \\ & + \gamma \hbar S \int \frac{dx}{2a} \left(2\boldsymbol{H} \cdot \boldsymbol{l} - a(\partial_x \boldsymbol{H}) \cdot \boldsymbol{n} \right). \end{aligned} \tag{2.7}$$

As seen, the magnetic field couples not only to $\boldsymbol{l}$ but also to $\boldsymbol{n}$ [19].

2.2.2 Lagrangian and equations of motion

To derive the Lagrangian, $L = L_0 - H$, we next look at its kinetic part,

$$\begin{aligned} L_0 &= \hbar S \sum_i \dot{\phi}_i \cos\theta_i \\ &= \hbar S \sum_n \left(\dot{\phi}_{2n} \cos\theta_{2n} + \dot{\phi}_{2n+1} \cos\theta_{2n+1} \right), \end{aligned} \tag{2.8}$$

where the spins are expressed as

$$\boldsymbol{S}_i = S(\sin\theta_i \cos\phi_i, \sin\theta_i \sin\phi_i, \cos\theta_i). \tag{2.9}$$

Let $\theta_{2n+1} = \pi - (\theta_{2n} + \delta\theta_{2n+1})$ and $\phi_{2n+1} = \pi + (\phi_{2n} + \delta\phi_{2n+1})$, so that the neighboring spins are totally antiparallel when $\delta\theta = \delta\phi = 0$. To leading order in $\delta\theta$ and $\delta\phi$, one finds[21, 22]

$$L_0 = 2\hbar S \int \frac{dx}{2a} \boldsymbol{l} \cdot (\boldsymbol{n} \times \dot{\boldsymbol{n}}), \tag{2.10}$$

up to a total time derivative. This shows that $2\hbar S(\boldsymbol{l} \times \boldsymbol{n})$ is the canonical momentum conjugate to $\boldsymbol{n}$. As a side note, the emergent gauge field, $A_{\mathrm{AF},i} = \boldsymbol{l} \cdot (\partial_i \boldsymbol{n} \times \boldsymbol{n})$, demonstrated in [23] for canted antiferromagnets complies with this kinetic term.

Damping is taken into account by Rayleigh's dissipation function,

$$W = \alpha \frac{\hbar}{2S} \sum_i \dot{\boldsymbol{S}}_i^2 = \alpha \hbar S \sum_n (\dot{\boldsymbol{l}}_n^2 + \dot{\boldsymbol{n}}_n^2). \tag{2.11}$$

In the continuum approximation, we write

$$W = 2\hbar S \int \frac{dx}{2a} \left(\frac{1}{2} \alpha_\ell \dot{\boldsymbol{l}}^2 + \frac{1}{2} \alpha_n \dot{\boldsymbol{n}}^2 \right), \tag{2.12}$$

where we introduced two damping constants, α_ℓ and α_n, for more generality [24].

By noting the constraints, Eq. (2.6), the equations of motion are obtained as

$$\begin{cases} \dot{\boldsymbol{n}} &= \left(\dfrac{1}{s_n} \dfrac{\delta H}{\delta \boldsymbol{n}} + \alpha_n \dot{\boldsymbol{n}} \right) \times \boldsymbol{l} + \left(\dfrac{1}{s_n} \dfrac{\delta H}{\delta \boldsymbol{l}} + \alpha_\ell \dot{\boldsymbol{l}} \right) \times \boldsymbol{n} \\ \dot{\boldsymbol{l}} &= \left(\dfrac{1}{s_n} \dfrac{\delta H}{\delta \boldsymbol{n}} + \alpha_n \dot{\boldsymbol{n}} \right) \times \boldsymbol{n} + \left(\dfrac{1}{s_n} \dfrac{\delta H}{\delta \boldsymbol{l}} + \alpha_\ell \dot{\boldsymbol{l}} \right) \times \boldsymbol{l} \end{cases}, \tag{2.13}$$

in agreement with Ref. [25]. Here, we defined the angular momentum density $s_n = 2\hbar S/(2a)$. Note that these equations of motion respect the constraints, Eq. (2.6). The first equation of Eq. (2.13) can be written as [18, 26]

$$\boldsymbol{l} = \frac{\hbar}{4JS}(\boldsymbol{n} \times \dot{\boldsymbol{n}} - \gamma \boldsymbol{H}_\perp) - \frac{a}{2}(\partial_x \boldsymbol{n}), \tag{2.14}$$

to leading order in $\boldsymbol{l}$, where $\boldsymbol{H}_\perp = \boldsymbol{n} \times (\boldsymbol{H} \times \boldsymbol{n})$ is the component perpendicular to $\boldsymbol{n}$. The first term ($\sim \boldsymbol{n} \times \dot{\boldsymbol{n}}$) embodies the momentum nature of $\boldsymbol{l}$ conjugate to $\boldsymbol{n}$, namely, it is proportional to the "velocity" $\dot{\boldsymbol{n}}$. The second term is due to canting induced by $\boldsymbol{H}$. The linear dependence on the field $\boldsymbol{H}_\perp$ indicates that the response to it is paramagnetic. The last term ($\sim \partial_x \boldsymbol{n}$) is referred to in Ref. [18] as the intrinsic magnetic moment induced by the Néel texture. Substituting this result into the second equation of Eq. (2.13), one obtains the equation of motion written solely by the Néel vector,

$$\begin{aligned} -\frac{\hbar^2}{2J}\,\ddot{\boldsymbol{n}} \times \boldsymbol{n} = \Big[& -2JS^2a^2(\partial_x^2 \boldsymbol{n}) - 4KS^2(\boldsymbol{n}\cdot\hat{z})\,\hat{z} + 2\hbar S\alpha_n \dot{\boldsymbol{n}} \\ & + \frac{\gamma\hbar^2}{J}(\boldsymbol{H}\cdot\boldsymbol{n})\,\dot{\boldsymbol{n}} \times \boldsymbol{n} + \frac{(\gamma\hbar)^2}{2J}(\boldsymbol{H}\cdot\boldsymbol{n})\,\boldsymbol{H} \\ & - \frac{\gamma\hbar^2}{2J}(\dot{\boldsymbol{H}} \times \boldsymbol{n}) \Big] \times \boldsymbol{n}. \end{aligned} \tag{2.15}$$

As an important observation, the terms with $\partial_x \boldsymbol{H}$ have been canceled out. To see what happened, let us go back to the Lagrangian L, or its density,

$$\begin{aligned} \mathcal{L} = {} & s_n\,\boldsymbol{l}\cdot(\boldsymbol{n}\times\dot{\boldsymbol{n}}) - s_n\gamma\left\{\boldsymbol{H}\cdot\boldsymbol{l} - \frac{a}{2}(\partial_x\boldsymbol{H})\cdot\boldsymbol{n}\right\} \\ & - \frac{2JS^2}{a}\left\{\boldsymbol{l}^2 + \frac{a^2}{2}(\partial_x\boldsymbol{n})^2 + a\,\boldsymbol{l}\cdot(\partial_x\boldsymbol{n}) - \frac{K}{2J}(n^z)^2\right\}. \end{aligned} \tag{2.16}$$

Since this is quadratic in $\boldsymbol{l}$, one can "integrate out" $\boldsymbol{l}$ and obtain the one written solely by the Néel vector,

$$\begin{aligned} \mathcal{L} = {} & \frac{\hbar^2}{8Ja}\dot{\boldsymbol{n}}^2 - \frac{JS^2a}{2}(\partial_x\boldsymbol{n})^2 + \frac{KS^2}{a}(n^z)^2 \\ & + \frac{(\gamma\hbar)^2}{8Ja}(\boldsymbol{H}\times\boldsymbol{n})^2 + \frac{\gamma\hbar S}{2}\,\partial_x(\boldsymbol{H}\cdot\boldsymbol{n}) \\ & - \frac{s_n}{2}(\boldsymbol{n}\times\dot{\boldsymbol{n}})\cdot\left[a\,\partial_x\boldsymbol{n} + \frac{\gamma\hbar}{2JS}\boldsymbol{H}\right]. \end{aligned} \tag{2.17}$$

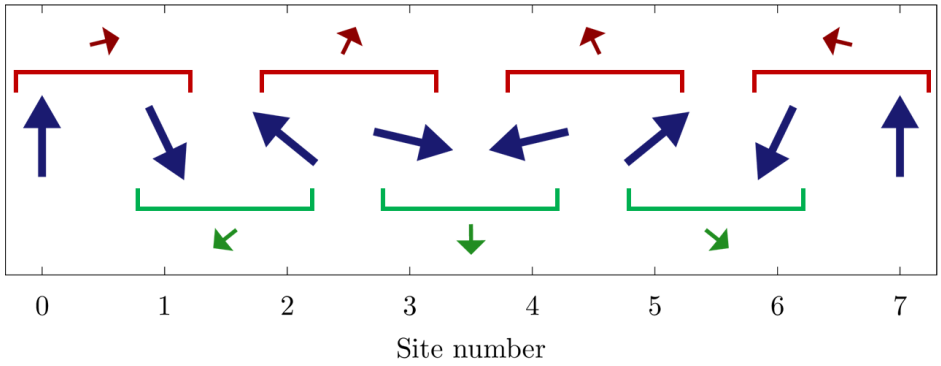

Figure 2.1: This figure illustrates that the uniform moment, Eq. (2.2), in the presence of antiferromagnetic spin texture depends on the choice of unit cell. The long arrows represent the atomic spins, $\boldsymbol{S}_i$. The top red arrows and the bottom green arrows represent the "uniform moments" locally defined by the average of the two neighboring spins, $(\boldsymbol{S}_i + \boldsymbol{S}_{i+1})/2$. Here, they arise from the antiferromagnetic spin texture, and as seen, they are mutually opposite. Such unit-cell-choice dependent components should not represent the physical magnetization.

Here, the Zeeman coupling of the "intrinsic magnetization" ($\sim \boldsymbol{H} \cdot \partial_x \boldsymbol{n}$) has been combined with the additional term[19] ($\sim \boldsymbol{n} \cdot \partial_x \boldsymbol{H}$ in Eq. (2.5)), forming a total derivative, $\partial_x(\boldsymbol{H} \cdot \boldsymbol{n})$. This is why the intrinsic moment does not appear in the equation of motion, Eq. (2.15). Intuitively, this can be understood from Fig. 2.1, which shows that the texture-induced uniform moment depends on the unit-cell choice; if another choice is made, it changes sign. This means that the texture-induced uniform moment is an artifact of the parametrization of Eq. (2.2), and does not appear in physical phenomena.

Two small notes. First, the quadratic term in $\boldsymbol{H}$, namely, the fifth term $\sim (\boldsymbol{H} \cdot \boldsymbol{n})\, \boldsymbol{H}$ in Eq. (2.15) or the fourth term $\sim (\boldsymbol{H} \times \boldsymbol{n})^2$ in Eq. (2.17), has the same form as the magnetic anisotropy term, hence the magnetic field acts as a hard-axis anisotropy. (But the effect is small, see below.) Second, the sixth term $\sim (\boldsymbol{n} \times \dot{\boldsymbol{n}}) \cdot \partial_x \boldsymbol{n}$ in Eq. (2.17) is "topological", and does not contribute to the equation of motion, hence can be omitted.

2.3 Domain wall motion

In this section, we study the domain wall motion in an inhomogeneous magnetic field using collective coordinates. We take the magnetic field to be in the easy-axis ($\hat{z}$-) direction with magnitude linearly varying in space,

$$\boldsymbol{H} = H_z \hat{z} = (H_0 + H_1 x)\, \hat{z}. \tag{2.18}$$

2.3.1 Static domain wall solution

To work with collective coordinates of the antiferromagnetic domain wall, one must first obtain a static domain wall solution. Dropping the time derivative terms, Eq. (2.15) becomes

$$0 = \left[-2Ja^2(\partial_x^2 \boldsymbol{n}) - 4K(\boldsymbol{n}\cdot\hat{z})\,\hat{z} + \frac{(\gamma\hbar)^2}{2JS^2}(\boldsymbol{H}\cdot\boldsymbol{n})\,\boldsymbol{H} \right] \times \boldsymbol{n}. \tag{2.19}$$

With Eq. (2.18) for the magnetic field,

$$0 = \left[-2Ja^2(\partial_x^2 \boldsymbol{n}) - 4K'(\boldsymbol{n}\cdot\hat{z})\,\hat{z} \right] \times \boldsymbol{n}, \tag{2.20}$$

where $K' = K - (\gamma\hbar H_z)^2/(8JS^2)$. Note that the Zeeman coupling $\gamma\hbar H_z$ is typically of the order of few kelvins (for H_z of few tesla), similar to the anisotropy energy. Thus, the difference between K' and K is of order $O(K^2/J)$ which is dismissed under our current approximation, $K' \simeq K$. We write the Néel vector using the polar and azimuthal angles,

$$\boldsymbol{n} = (\sin\theta\cos\phi, \sin\theta\sin\phi, \cos\theta), \tag{2.21}$$

under the assumption that the uniform moment is small (namely, $1 = \boldsymbol{n}^2 + \boldsymbol{l}^2 \simeq \boldsymbol{n}^2$). Assuming ϕ is spatially uniform, and noting that $\hat{z} = \boldsymbol{n}\cos\theta - \boldsymbol{e}_\theta \sin\theta$, the static texture satisfies

$$0 = -\lambda^2 \partial_x^2 \theta + \cos\theta \sin\theta, \tag{2.22}$$

where $\lambda = a\sqrt{J/2K}$. Note that the domain wall width in antiferromagnets differ to the ferromagnetic one by a factor of $1/\sqrt{2}$. A domain wall solution is given by [17]

$$\cos\theta = \tanh\left(\pm \frac{x - X}{\lambda} \right), \tag{2.23}$$

and thus $\sin\theta = \left[\cosh\frac{x-X}{\lambda}\right]^{-1}$, where X is the domain wall position. The $\pm$ sign is the topological charge of the domain wall. The position of the wall, X, and the angle of the wall plane, ϕ (= const.), will be promoted to dynamical variables in the next subsection.

2.3.2 Collective coordinate description

Using the domain wall solution for $\boldsymbol{n}$, Eq. (2.23), the kinetic part of the Lagrangian, L_0 in Eq. (2.10), is obtained as

$$L_{\mathrm{DW},0} = 2s_n\big(\pm l_\phi \dot{X} - \lambda l_\theta \dot{\phi}\big), \tag{2.24}$$

where we defined

$$l_\theta = \int \frac{dx}{2\lambda}\frac{\boldsymbol{e}_\theta\cdot\boldsymbol{l}(x)}{\cosh\frac{x-X}{\lambda}}, \quad l_\phi = \int \frac{dx}{2\lambda}\frac{\boldsymbol{e}_\phi\cdot\boldsymbol{l}(x)}{\cosh\frac{x-X}{\lambda}}. \tag{2.25}$$

Equation (2.24) indicates that l_θ and l_ϕ are canonical momenta conjugate to ϕ and X, respectively, which should be considered as new collective variables. Note that a uniform moment induced by the (longitudinal) field, Eq. (2.18), is localized at the domain wall (see Eq. (2.14)). In a more systematic treatment, this corresponds to expanding $\boldsymbol{l}$ with some complete set of functions $\{\varphi_n(x)\}$ [17],

$$\boldsymbol{l}(x) = (l_\theta \boldsymbol{e}_\theta + l_\phi \boldsymbol{e}_\phi)\,\varphi_0(x) + \sum_k \boldsymbol{l}_k\,\varphi_k(x), \tag{2.26}$$

where

$$\varphi_0(x) = \frac{1}{\cosh\frac{x-X}{\lambda}}, \tag{2.27}$$

and retain the first two terms. See Ref. [17] for other $\varphi_k(x)$'s, which, together with $\varphi_0(x)$, form a complete orthogonal basis.

The Hamiltonian, Eq. (2.7), then becomes

$$\begin{aligned} H_{\mathrm{DW}} = 4JS^2\frac{\lambda}{a}\left\{\left(l_\theta \mp \frac{a}{2\lambda}\right)^2 + l_\phi^2 + \frac{a^2}{2\lambda^2}\right\} \\ - \gamma\hbar S\left(\frac{2\lambda}{a}\,l_\theta \mp 1\right)(H_0 + H_1 X). \end{aligned} \tag{2.28}$$

The dissipation function Eq. (2.12), dismissing the $\alpha_\ell \dot{\boldsymbol{l}}^2$ term [27], is given by

$$W_{\rm DW} = s_n \alpha_n \lambda \left(\frac{\dot{X}^2}{\lambda^2} + \dot{\phi}^2 \right). \tag{2.29}$$

These results lead to the following four equations of motion,

$$\pm \dot{l}_\phi = -\alpha_n \dot{X}/\lambda + \gamma H_1 \lambda \left(l_\theta \mp \frac{a}{2\lambda} \right), \tag{2.30}$$

$$\dot{l}_\theta = \alpha_n \dot{\phi}, \tag{2.31}$$

$$\dot{\phi} = -(4JS/\hbar) \left(l_\theta \mp \frac{a}{2\lambda} \right) + \gamma (H_0 + H_1 X), \tag{2.32}$$

$$\dot{X} = \pm (4JS/\hbar) \lambda l_\phi. \tag{2.33}$$

Note that (X, l_ϕ) and (ϕ, l_θ) are coupled via H_1. However, l_θ and l_ϕ can be eliminated, resulting in two coupled equations for X and ϕ, or χ and φ defined by

$$\chi = \frac{X}{\lambda} + \frac{H_0}{H_1 \lambda}, \qquad \varphi = \phi + \phi_1, \tag{2.34}$$

as

$$\begin{cases} \ddot{\chi} &= -\tilde{\alpha} \dot{\chi} + \tilde{H}_1 \tilde{\alpha} \varphi \\ \dot{\varphi} &= \tilde{H}_1 \chi - \tilde{\alpha} \varphi \end{cases} . \tag{2.35}$$

Here, we defined

$$\tilde{\alpha} = \frac{4SJ}{\hbar} \alpha_n, \qquad \tilde{H}_1 = \gamma H_1 \lambda, \tag{2.36}$$

and $\phi_1 = \alpha_n^{-1}(l_\theta^0 \mp a/2\lambda) - \phi_0$, where l_θ^0 and ϕ_0 are initial values introduced when Eq. (2.31) is integrated in time. It is readily seen that the acceleration of the domain wall is absent if there is no damping, $\tilde{\alpha} = 0$. This feature is not seen in Refs. [18, 19]. Writing the equations of motion in matrix form,

$$\frac{d}{dt} \begin{pmatrix} \dot{\chi} \\ \chi \\ \varphi \end{pmatrix} = \begin{pmatrix} -\tilde{\alpha} & 0 & \tilde{H}_1 \tilde{\alpha} \\ 1 & 0 & 0 \\ 0 & \tilde{H}_1 & -\tilde{\alpha} \end{pmatrix} \begin{pmatrix} \dot{\chi} \\ \chi \\ \varphi \end{pmatrix}, \tag{2.37}$$

and assuming the solution of the form $\sim e^{\varepsilon t}$, the problem reduces to an eigenvalue problem with determinant,

$$\varepsilon(\varepsilon+\tilde{\alpha})^2-\tilde{\alpha}\tilde{H}_1^2=0. \tag{2.38}$$

Since $\tilde{\alpha}$ is positive, this equation has one real positive root ε_0, and two complex roots ε_1 and ε_2 $(=\varepsilon_1^*)$ with negative real parts. Using Cardano's method, the roots are written as

$$\varepsilon_n=-\frac{2\tilde{\alpha}}{3}+\omega^n\sqrt[3]{q+\sqrt{q^2-p^3}}+\omega^{2n}\sqrt[3]{q-\sqrt{q^2-p^3}},$$
$$n=0,\,1,\,2 \tag{2.39}$$

where $p=\frac{1}{9}\tilde{\alpha}^2$, $q=(\frac{1}{27}\tilde{\alpha}^2+\frac{1}{2}\tilde{H}_1^2)\tilde{\alpha}$, $\omega=-\frac{1}{2}+\frac{1}{2}\sqrt{3}i$, and the real branch of the cube roots are chosen. (Note that $q^2-p^3\geq 0$.) With these roots, the general solution is given by

$$\chi=C_0e^{\varepsilon_0 t}+\mathrm{Re}\left[C_1e^{\varepsilon_1 t}\right], \tag{2.40}$$

$$\varphi=C_0\frac{\tilde{H}_1}{\tilde{\alpha}+\varepsilon_0}e^{\varepsilon_0 t}+\mathrm{Re}\left[C_1\frac{\tilde{H}_1}{\tilde{\alpha}+\varepsilon_1}e^{\varepsilon_1 t}\right], \tag{2.41}$$

where a real constant C_0 and a complex constant C_1 are determined by initial conditions. Thus, we find that an inhomogeneous magnetic field drives domain wall motion, $X\sim\lambda C_0e^{\varepsilon_0 t}$, that grows exponentially in time.

When $\tilde{\alpha}\gg\tilde{H}_1$, the roots can be given as

$$\varepsilon_0\simeq\frac{3\tilde{H}_1^2}{\tilde{\alpha}},\qquad \varepsilon_1\simeq-\tilde{\alpha}+i\tilde{H}_1, \tag{2.42}$$

to leading order of $\tilde{\alpha}/\tilde{H}_1$. We expect most antiferromagnets under magnetic field satisfy this condition. For example, for $2S\alpha_n=10^{-3}$, $J=10^3$K, $\gamma\hbar H_1=$ 1K/cm, $\lambda=$ 100nm, and $S=1$, then, $\tilde{\alpha}=10^{11}\mathrm{s}^{-1}$, $\tilde{H}_1=10^5\mathrm{s}^{-1}$, and $\varepsilon_0=1\mathrm{s}^{-1}$. A plot of ε_0 in Eq. (2.39) is shown in Fig. 2.2 as a function of $\tilde{\alpha}$ and $\tilde{H}_1$.

The above solutions (and equations) are limited to the case, $|l_\theta|,|l_\phi|\ll 1$, in order for the exchange approximation to be valid. Since $l_\theta/\chi\sim\alpha_n\tilde{H}_1/(\tilde{\alpha}+\varepsilon_0)$, this requires $|\chi|\ll(\tilde{\alpha}+\varepsilon_0)/(\alpha_n|\tilde{H}_1|)$, or $|X-X_0|/\lambda\ll\max\{4SJ/\hbar,\varepsilon_0/\alpha_n\}/|\tilde{H}_1|\equiv b$, namely, the domain wall position should be within the distance $\sim\frac{1}{10}b\lambda$ from the position $X_0\equiv-H_0/H_1$ of vanishing external field,

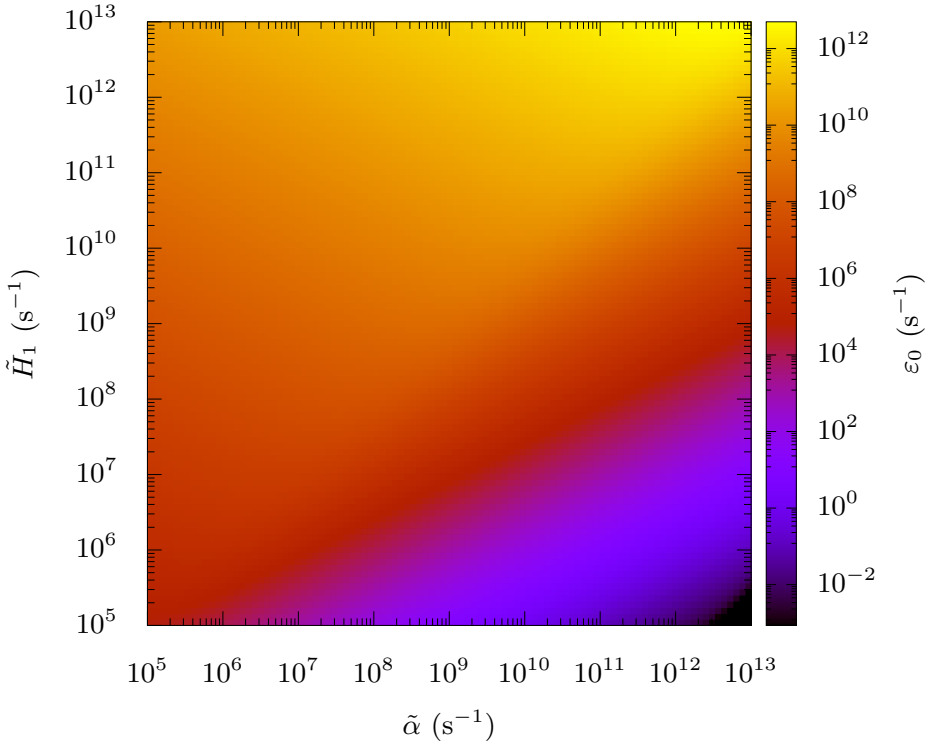

Figure 2.2: The real positive eigenvalue ε_0 [Eq. (2.39)] plotted as a function of $\tilde{\alpha}$ and $\tilde{H}_1$. It increases with $\tilde{H}_1$ as expected.

$H_z = 0$. Beyond this point, the nonlinearity of l_θ may not be neglected. With parameters given above, we have $b \sim 10^9$, hence $b\lambda$ is much larger than the domain wall width, and the above condition is always satisfied. We note that the above condition is equivalent to $\gamma\hbar|H_z| \ll J$ at the domain wall position, which is practically always satisfied.

2.3.3 With pinning potential

We introduce a pinning potential by a local modulation δK of the anisotropy K at the origin, $K \to K - 2a\delta(x)\delta K$ [17]. The pinning potential of the

domain wall is then given by

$$V_{\rm pin} = -2\delta K S^2 \frac{1}{\cosh^2(X/\lambda)} \simeq 2\delta K S^2((X/\lambda)^2 - 1)\,\Theta(\lambda - |X|), \tag{2.43}$$

which we approximated by a truncated parabola. (Θ is the Heaviside step function.) When $|X| < \lambda$, the equation of motion is altered as

$$\frac{d}{dt}\begin{pmatrix}\dot\chi\\ \chi\\ \varphi\end{pmatrix} = \begin{pmatrix}-\tilde\alpha & -\delta\tilde K & \tilde H_1\tilde\alpha\\ 1 & 0 & 0\\ 0 & \tilde H_1 & -\tilde\alpha\end{pmatrix}\begin{pmatrix}\dot\chi\\ \chi\\ \varphi\end{pmatrix}, \tag{2.44}$$

where

$$\delta\tilde K = 4\delta K S^2 \frac{a}{\lambda}\frac{2J}{\hbar^2}, \tag{2.45}$$

and we redefined

$$\chi = \frac{X}{\lambda} - \gamma H_0 \frac{\tilde H_1}{\delta\tilde K - \tilde H_1^2}, \tag{2.46}$$

$$\varphi = \phi + \phi_1 - \frac{1}{\tilde\alpha}\gamma H_0 \frac{\delta\tilde K}{\delta\tilde K - \tilde H_1^2}. \tag{2.47}$$

The determinant is now given by

$$(\varepsilon^2 + \varepsilon\tilde\alpha + \delta\tilde K)(\varepsilon + \tilde\alpha) - \tilde\alpha\tilde H_1^2 = 0. \tag{2.48}$$

A positive real root exists when

$$\delta\tilde K < \tilde H_1^2, \tag{2.49}$$

giving us the depinning condition. The analytical expression of the real root of the cubic equation is given by Eq. (2.39) with $p = \frac{1}{9}\tilde\alpha^2 - \frac{1}{3}\delta\tilde K$ and $q = (\frac{1}{27}\tilde\alpha^2 + \frac{1}{2}\tilde H_1^2 - \frac{1}{6}\delta\tilde K)\tilde\alpha$.

2.4 Numerical simulation

To test the validity of the approximations made above, such as the continuum description, the discarding of higher-order terms in $\boldsymbol{l}$, and the use of collective

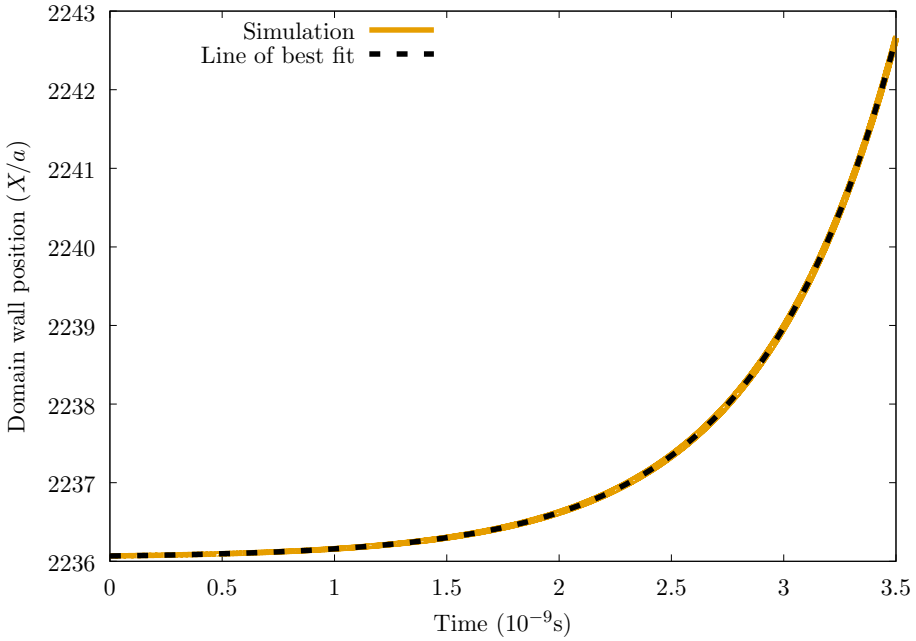

Figure 2.3: Domain wall position as a function of time under a linearly-varying magnetic field, Eq. (2.18). The simulation result (orange line) is fitted by an exponential curve (blue dashed line), with exponent $\varepsilon_0 = 1.627 \times 10^9 \mathrm{s}^{-1}$. The used parameters are as follows; $J = 10^3\mathrm{K}$, $K = 1\mathrm{K}$, $\gamma\hbar = 1\mathrm{K/T}$, $a = 10^{-10}\mathrm{m}$, $H_1 = 10\mathrm{mT}/a$, $H_0 + H_1 X(0) = H_1 \lambda \times 10^{-3}$ (field at the initial position $X(0)$), $\alpha = 10^{-3}$, and $S = 1$. The system is one-dimensional and has $N = 10^4$ spins (so the system size is $L = 10^4 a = 1\mu\mathrm{m}$), and the spins at both ends are fixed upwards ($\boldsymbol{S}_1 = \boldsymbol{S}_N = +\hat{z}$). The starting configuration is Eq. (2.23) with initial position $X(0) = 10^2\lambda \simeq 2236a$. A time discretization of $dt = 5 \times 10^{-15}\mathrm{s}$ is used.

coordinates, we perform an atomistic simulation based on the equation of motion for each $\boldsymbol{S}_i$,

$$\dot{\boldsymbol{S}}_i + \frac{\alpha}{S}\boldsymbol{S}_i \times \dot{\boldsymbol{S}}_i = \hbar^{-1}\left[J(\boldsymbol{S}_{i-1} + \boldsymbol{S}_{i+1}) - 2KS_i^z\hat{z} + \gamma\hbar\boldsymbol{H}_i\right] \times \boldsymbol{S}_i. \tag{2.50}$$

Using the approximate domain wall solution (2.23) as an initial configuration, we solved Eq. (2.50) under an inhomogeneous magnetic field, Eq. (2.18). The position of the domain wall is determined by linear interpolation as the point at which the profile of the staggered component $(-1)^i S_i^z$ vanishes, and it is plotted in Fig. 2.3 as a function of time. The values of the parameters used are described in the caption of Fig. 2.3. The width of the domain wall is $\lambda = a\sqrt{J/2K} \simeq 22.36a$. In accord with our analysis, the domain wall position changes exponentially with time. The exponent obtained from the simulation, $\varepsilon_0 = 1.627 \times 10^9 \mathrm{s}^{-1}$, is very close to the analytical result, $\varepsilon_0 = 1.626 \times 10^9 \mathrm{s}^{-1}$ [Eq. (2.39)]. The domain wall moves in the direction of stronger magnetic field.

We next simulate the motion of the domain wall with pinning potential located at the initial position of the domain wall. With the parameter values described in the caption of Fig. 2.3, Eq. (2.49) is satisfied when $\delta K \leq 1.398 \times 10^4 \mathrm{K}$. To test this value, we simulate the domain wall motion with "strong pinning" $\delta K = 2 \times 10^{-4}\mathrm{K}$, and "weak pinning" $\delta K = 1 \times 10^{-4}\mathrm{K}$. As shown in Fig. 2.4, the former pins the domain wall, while the latter cannot stop the exponential increase of the domain wall position.

2.5 Physical picture

Here, we discuss the physical mechanism of the domain wall actuation by an inhomogeneous magnetic field.

First, consider a static solution. Then, Eqs. (2.30), (2.32), and (2.33) lead to $l_\theta = \pm a/2\lambda$, $l_\phi = 0$, and $X = -H_0/H_1$. The first two relations show that only the artifactual texture-induced uniform moment is present, while the third relation tells us that the domain wall must be positioned where the magnetic field vanishes. When the domain wall is placed in a finite magnetic field, the Néel vector starts to precess ($\dot{\phi} \neq 0$) according to Eq. (2.32), and the uniform moment l_θ develops through damping [see Eq. (2.31)]. As seen from Eqs. (2.30) and (2.33), the development of l_θ in

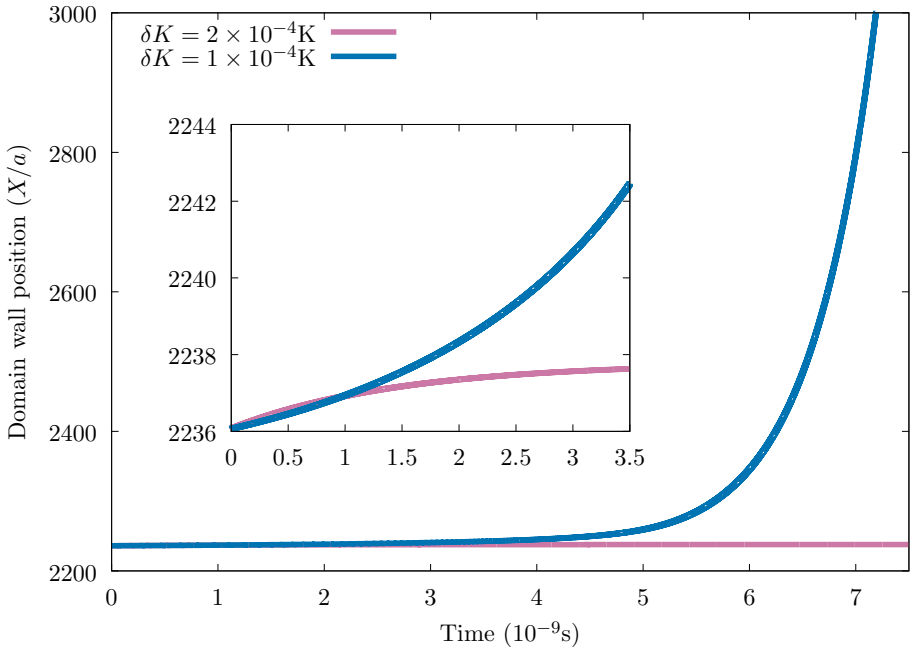

Figure 2.4: Domain wall position as a function of time in the presence of pinning potential. Using the same parameters as in Fig. 2.3, we added a pinning potential δK on the neighboring two sites at the initial position of the domain wall (i.e. $10^2\lambda$ from the left end). The domain wall remains pinned for $\delta K = 2 \times 10^{-4}$K [purple (or light) line], whereas it is depinned for $\delta K = 1 \times 10^{-4}$K [blue (or dark) line]. The inset shows a closeup.

conjunction with the field gradient applies a force on the domain wall; like in the Stern-Gerlach experiment, the domain wall feels a force towards the direction with stronger magnetic field to gain Zeeman energy. Thus, the antiferromagnetic domain wall can be thought of as a paramagnetic particle under an (inhomogeneous) applied magnetic field. Without damping, the uniform moment is not induced by the field, hence there is no actuation of domain wall motion. The present mechanism involves a dissipative process, hence is different from the purely reactive mechanisms discussed in Refs. [18, 19].

2.6 Reformulation

We have seen that the Zeeman coupling of the intrinsic magnetization ($\sim \boldsymbol{H}\cdot\partial_x\boldsymbol{n}$) is nullified by the coupling of the Néel vector to the field gradient ($\sim \boldsymbol{n}\cdot\partial_x\boldsymbol{H}$ in Eq. (2.5)). The reasoning behind this was given intuitively through Fig. 2.1, which indicates that the intrinsic magnetization is not a physical quantity.

In this section, we reformulate the theory in terms of "physical magnetization", eliminating the intrinsic magnetization. We first identify the physical magnetization by reexamining the interaction with external magnetic field, and therewith express the Lagrangian (Sec. 6.1). The result is applied to the collective coordinates of a domain wall (Sec. 6.2). Finally, the procedure is extended to general lattices (Sec. 6.3).

2.6.1 Physical magnetization

To identify the physical magnetization, we look at the interaction with the external magnetic field [the second line of Eq. (2.7)], and rewrite it as

$$2\gamma\hbar S\int\frac{dx}{2a}\left\{\left(\boldsymbol{l}+\frac{a}{2}\partial_x\boldsymbol{n}\right)\cdot\boldsymbol{H}-\frac{a}{2}\,\partial_x(\boldsymbol{H}\cdot\boldsymbol{n})\right\}. \tag{2.51}$$

The first term is the Zeeman coupling in the bulk, and the second (total-derivative) term describes that at the edges. Therefore, the physical magnetization is identified to be $-\gamma s_n\tilde{\boldsymbol{l}}$, with

$$\tilde{\boldsymbol{l}}\equiv\boldsymbol{l}+\frac{a}{2}(\partial_x\boldsymbol{n}). \tag{2.52}$$

This is the uniform moment with the intrinsic magnetization subtracted, and agrees with Haldane's definition[28] (according to the analysis made in Ref. [18]). In terms of $\tilde{\boldsymbol{l}}$, the Lagrangian density, Eq. (2.16), is simplified as

$$\begin{aligned}\mathcal{L}=&\,s_n\tilde{\boldsymbol{l}}\cdot(\boldsymbol{n}\times\dot{\boldsymbol{n}}-\gamma\boldsymbol{H})\\&-s_n\frac{2JS}{\hbar}\left\{\tilde{\boldsymbol{l}}^2+\frac{a^2}{4}(\partial_x\boldsymbol{n})^2-\frac{K}{2J}(n^z)^2\right\}.\end{aligned} \tag{2.53}$$

Here, we dropped the "topological" term $\sim\partial_x\boldsymbol{n}\cdot(\boldsymbol{n}\times\dot{\boldsymbol{n}})$ since it does not affect the equation of motion. Note that the exchange stiffness constant of the Néel vector (the coefficient of $(\partial_x\boldsymbol{n})^2$) has been reproduced correctly

(without eliminating the uniform moment), and the "sublattice symmetry" $(\tilde{\boldsymbol{l}}, \boldsymbol{n}) \to (\tilde{\boldsymbol{l}}, -\boldsymbol{n})$ has been recovered. Note also that the constraints are preserved, $\tilde{\boldsymbol{l}} \cdot \boldsymbol{n} = 0$ and $\boldsymbol{n}^2 + \tilde{\boldsymbol{l}}^2 = 1$, within the exchange approximation. These suggest that the theory is simplified if reformulated in terms of $\tilde{\boldsymbol{l}}$.

To complete this program, we need to examine the damping term. If the dissipation function has the form,

$$W = s_n \int dx \left(\frac{1}{2} \alpha_\ell \dot{\tilde{\boldsymbol{l}}}^2 + \frac{1}{2} \alpha_n \dot{\boldsymbol{n}}^2 \right), \tag{2.54}$$

in terms of $\tilde{\boldsymbol{l}}$ [instead of $\boldsymbol{l}$ as in Eq. (2.12)], the damping term is also simplified. To show that this is indeed the case, it is sufficient to observe that the spins $\boldsymbol{S}_i$ couple to other degrees of freedom ("environment") through $(\tilde{\boldsymbol{l}}, \boldsymbol{n})$ rather than $(\boldsymbol{l}, \boldsymbol{n})$. As an example, let us consider the s-d exchange coupling to conduction electrons,

$$H_{\rm sd} = -J_{\rm sd} \sum_i \boldsymbol{S}_i \cdot \boldsymbol{\sigma}_i, \tag{2.55}$$

where $\boldsymbol{\sigma}_i$ is the electron spin at site i, and $J_{\rm sd}$ is the coupling constant. This has the same form as the Zeeman coupling ($\boldsymbol{H}_i \to \boldsymbol{\sigma}_i$), and we can proceed in exactly the same way as Eq. (2.51). By noting that $\boldsymbol{\sigma}_i$ may have staggered component as well, we obtain the s-d coupling in the continuum approximation as

$$H_{\rm sd} = -J_{\rm sd} S \int d\boldsymbol{r} \left\{ \left(\boldsymbol{l} + \frac{a}{2} \partial_x \boldsymbol{n} \right) \cdot \boldsymbol{\sigma}_\ell + \boldsymbol{n} \cdot \boldsymbol{\sigma}_n \right\}, \tag{2.56}$$

where $\boldsymbol{\sigma}_\ell$ and $\boldsymbol{\sigma}_n$ are the uniform and staggered components of the electron spin density. (For simplicity, we dropped the total derivative terms.) As seen, there is a "correction" $a\,\partial_x \boldsymbol{n}/2$ in the first term, and the coupling to the electrons occurs through $(\tilde{\boldsymbol{l}}, \boldsymbol{n})$, instead of $(\boldsymbol{l}, \boldsymbol{n})$. (Precisely speaking, the "corrections" arise symmetrically between $\boldsymbol{l}$ and $\boldsymbol{n}$, but in the second term, we adopted the exchange approximation, $\boldsymbol{n} + a\,\partial_x \boldsymbol{l}/2 \simeq \boldsymbol{n}$.) Therefore, the resulting Gilbert damping, or the dissipation function, should have the form of Eq. (2.54) through $(\tilde{\boldsymbol{l}}, \boldsymbol{n})$.

Explicit calculations of Gilbert damping and spin-transfer torques are done in chapters 2 and 3, where we have found that the expectation value of $\boldsymbol{\sigma}_n$ is odd in $\boldsymbol{n}$ while that of $\boldsymbol{\sigma}_\ell$ is even [29]. Thus, the spin torques resulting from the s-d exchange interaction also possess the sublattice symmetry under $(\tilde{\boldsymbol{l}}, \boldsymbol{n}) \to (\tilde{\boldsymbol{l}}, -\boldsymbol{n})$.

2.6.2 Domain wall

For a domain wall in the collective coordinate description, the physical magnetization, Eq. (2.52), is given by

$$\tilde{l}_\theta \equiv l_\theta \mp \frac{a}{2\lambda}, \tag{2.57}$$

and l_ϕ (not altered). With these, the equations of motion are written as

$$\pm \dot{l}_\phi = -\alpha_n \dot{X}/\lambda + \gamma H_1 \lambda \tilde{l}_\theta, \tag{2.58}$$

$$\dot{\tilde{l}}_\theta = \alpha_n \dot{\phi}, \tag{2.59}$$

$$\dot{\phi} = -(4JS/\hbar)\, \tilde{l}_\theta + \gamma(H_0 + H_1 X), \tag{2.60}$$

$$\dot{X} = \pm(4JS/\hbar)\lambda l_\phi. \tag{2.61}$$

The sign $\pm$ represents the topological charge. We see that a static domain wall has $\tilde{l}_\theta = \gamma\hbar H_0/4JS$ for $H_1 = 0$, and $\tilde{l}_\theta = 0$ for $H_1 \neq 0$.

2.6.3 General case

The procedure described in Sec. 6.1 can be generalized to arbitrary bipartite lattices. We assume a nearest-neighbor exchange interaction J and a uniaxial magnetic anisotropy K. Taking the unit cell along the x direction, the Hamiltonian density (without Zeeman coupling terms) is calculated as

$$\mathcal{H}_{d,z} = s_n \frac{zJS}{\hbar} \left\{ \tilde{\boldsymbol{l}}^2 + \frac{a^2}{4d} \sum_{i=1}^{d} (\partial_i \boldsymbol{n})^2 - \frac{K}{zJ} (n^z)^2 \right\}, \tag{2.62}$$

where $\tilde{\boldsymbol{l}}$ is given by Eq. (2.52), d is the space dimensionality, and z is the number of nearest-neighbor sites. For example, $(d, z) = (2, 3), (2, 4)$, and (3,6) for honeycomb, square, and simple cubic lattices, respectively. The Zeeman coupling is the same as Eq. (2.51), hence $\tilde{\boldsymbol{l}}$ is identified as the physical magnetization. The Lagrangian density is given by $\mathcal{L} = s_n \tilde{\boldsymbol{l}} \cdot (\boldsymbol{n} \times \dot{\boldsymbol{n}} - \gamma \boldsymbol{H}) - \mathcal{H}_{d,z}$.

2.7 Summary

In chis chapter, we have investigated the motion of an antiferromagnetic domain wall under inhomogeneous magnetic field. Starting from the lattice Heisenberg model with antiferromagnetic exchange coupling, easy-axis

anisotropy, and Zeeman coupling, we constructed a continuum model by closely following Ref. [18]. We first retrieved a term that was missing in Ref. [18], in which the Néel vector couples to the field gradient. We have shown that this retrieved term nullifies the previously demonstrated coupling of the intrinsic magnetization, attributed to the Néel spin texture, to the magnetic field, and found an alternative mechanism for domain wall motion actuated by an inhomogeneous field.

As a supplemetary discussion, we pointed out that the uniform moment $\boldsymbol{l}$ defined by Eq. (2.2) contains unphysical component (intrinsic magnetization). We have reformulated the theory by properly defining the physical magnetization.

Chapter 3

Microscopic calculation of spin torques in textured antiferromagnets

In this chapter, we investigate the effect of conduction electrons on antiferromagnetic (AF) spins. In the first part of this chapter, we present a microscopic calculation for the spin-transfer torques (STT) and damping torques. It is found that the sign of the STT is opposite to that in ferromagnets because of the AF transport character, and the current-to-STT conversion factor is enhanced near the AF gap edge. The dissipative torque parameter β_n and the damping parameter α_n for the Néel vector arise from spin relaxation of electrons. In the second part of this chapter, physical consequences are demonstrated for the AF domain wall motion using collective coordinates. Similarities to the ferromagnetic case are pointed out such as intrinsic pinning and the specialty of $\alpha_n = \beta_n$. A recent experiment on a ferrimagnetic GdFeCo near its angular-momentum compensation temperature is discussed.

3.1 Introduction

In the previous chapter, we explored the effect of inhomogeneous magnetic fields on antiferromagnetic domain walls. In this chapter, we investigate the effect of conduction electrons on antiferromagnetic spins. Torque exerted by

conduction electrons on antiferromagnetic or ferromagnetic spins is referred to as spin torques. Spin torques are favored over magnetic field from a scalability perspective; while the magnetic field strength is proportional to total current, spin torques are proportional to current density [17].

Spin torques in textured ferromagnets (FM) is well-understood through the spin angular momentum transfer between the conduction electrons and magnetization [30, 31, 32]. However, a similar picture is not feasible in antiferromagnets (AFs) [6, 33, 4] since the magnetic order parameter and conduction electrons do not carry macroscopic spin angular momenta [34, 35, 24, 27, 36, 37, 38]. This makes microscopic studies indispensable for understanding spin torques in AFs.

In FM, electrons moving in a spin texture with exchange coupling exhibit a spin polarization,

$$\langle \hat{\boldsymbol{\sigma}} \rangle \ \propto \ \boldsymbol{n} \times (\boldsymbol{v} \cdot \nabla) \boldsymbol{n}, \tag{3.1}$$

where $\boldsymbol{n}$ is the magnetic order parameter (magnetization vector for FM) and $\boldsymbol{v}$ is a velocity that characterizes the electron flow (spin current for FM). The spin polarization arises as a reactive response [39] and exerts a reaction torque, known as the spin-transfer torque (STT), on the FM spins. In AF, Xu *et al.* [34] and Swaving and Duine [35] numerically obtained the same form of spin polarization as Eq. (3.1) with $\boldsymbol{n}$ now representing the Néel vector. Analogous to FM, this spin polarization emerges through a reactive process, and gives rise to a torque that conserves total angular momentum, which may thus be called the STT. However, in contrast to FM, the coefficient cannot be determined by a macroscopic argument based on the conservation law. Moreover, there is in general another type of torque, called the β torque, that arises as a dissipative response due to spin relaxation [40, 2], the analytic expression of which is yet to be determined for AFs.

In this chapter, we present a microscopic calculation of the STT, the β torque, and the damping torques in AF metals. A careful treatment is given to the effects of spin relaxation, which we model by magnetic impurities. We find a STT proportional to the electric current but with a coefficient different from that in FM. The β torque is proportional to the spin-relaxation rate. Interestingly, both torques in AFs drive the texture in the opposite direction compared to those in FMs. Using collective coordinates, it is shown that only the β torque drives AF domain walls (DWs) [24, 27], because the effect of STT is nullified by an effect similar to the intrinsic pinning in FM. Finally,

a recent experiment on the current-assisted DW motion in ferrimagnets at the angular-momentum compensation temperature [16] is discussed.

3.2 Model

We consider the s-d model consisting of localized spins (H_S), conduction electrons ($H_{\rm el}$), and the s-d exchange interaction ($H_{\rm sd}$) between them,

$$H = H_S + H_{\rm el} + H_{\rm sd}. \tag{3.2}$$

The space dimensionality, d, can be arbitrary in the general formulation, but explicit calculations will be done for a two-dimensional square lattice, $d = 2$.

We first sketch the derivation of the equations that describe long-wavelength, low-frequency dynamics of AF spins coupled to conduction electrons. We start with the lattice model,

$$H_S = J \sum_{\langle i,j \rangle} \boldsymbol{S}_i \cdot \boldsymbol{S}_j - K \sum_i (S_i^z)^2, \tag{3.3}$$

$$H_{\rm sd} = -J_{\rm sd} \sum_i \boldsymbol{S}_i \cdot c_i^\dagger \boldsymbol{\sigma}\, c_i, \tag{3.4}$$

where $\boldsymbol{S}_i$ is a localized, classical spin at site i, $J > 0$ is the AF exchange coupling constant between nearest-neighbor (n.n.) sites $\langle i, j \rangle$, and $K > 0$ is the easy-axis magnetic anisotropy constant. In $H_{\rm sd}$, $c_i^\dagger = (c_{i\uparrow}^\dagger, c_{i\downarrow}^\dagger)$ is the electron creation operator at site i, $\boldsymbol{\sigma}$ is a vector of Pauli matrices, and $J_{\rm sd}$ is the s-d exchange coupling constant.

We consider a two-sublattice unit cell m with localized spins, $\boldsymbol{S}_{A,m}$ and $\boldsymbol{S}_{B,m}$, on each sublattice, and define the Néel component $\boldsymbol{n}_m$ and the uniform component $\boldsymbol{l}_m$ by [41]

$$\boldsymbol{n}_m = \frac{\boldsymbol{S}_{A,m} - \boldsymbol{S}_{B,m}}{2S}, \qquad \boldsymbol{l}_m = \frac{\boldsymbol{S}_{A,m} + \boldsymbol{S}_{B,m}}{2S}, \tag{3.5}$$

where $S = |\boldsymbol{S}_i|$ is the (constant) magnitude of the localized spins. We assume the spatial variations are slow for $\boldsymbol{n}_m$ and $\boldsymbol{l}_m$, and adopt a continuum description, $\boldsymbol{n}_m \to \boldsymbol{n}(\boldsymbol{r})$ and $\boldsymbol{l}_m \to \boldsymbol{l}(\boldsymbol{r})$. We also exploit the exchange approximation, $|\boldsymbol{l}| \ll 1$, and neglect higher order terms in $\boldsymbol{l}$ [42]. It then follows from $|\,\boldsymbol{l} \pm \boldsymbol{n}| = 1$ that $|\boldsymbol{n}| = 1$ and $\boldsymbol{n} \cdot \boldsymbol{l} = 0$.

Since the magnetization $\boldsymbol{l}$ in Eq. (3.5) contains a texture-induced unphysical component [18], it is convenient to work with the physical magnetization [43],

$$\tilde{\boldsymbol{l}} \equiv \boldsymbol{l} + \frac{a}{2}(\partial_x \boldsymbol{n}), \tag{3.6}$$

where a is the lattice constant, and the x axis is chosen along the bond connecting two sites in the unit cell. This preserves the constraints, $\tilde{\boldsymbol{l}} \cdot \boldsymbol{n} = 0$ and $|\boldsymbol{n}| = 1$, within the exchange approximation, and simplifies the formalism. In terms of $\tilde{\boldsymbol{l}}$ and $\boldsymbol{n}$, the Lagrangian density is given by [43]

$$\mathcal{L}_S = s_n \left\{ \tilde{\boldsymbol{l}} \cdot (\boldsymbol{n} \times \dot{\boldsymbol{n}}) - \mathcal{H}_S - \mathcal{H}_{\rm sd} \right\}, \tag{3.7}$$

$$\mathcal{H}_S = \frac{zJS}{\hbar} \left\{ \tilde{\boldsymbol{l}}^2 + \frac{a^2}{4d} \sum_{i=1}^{d} (\partial_i \boldsymbol{n})^2 - \frac{K}{zJ} n_z^2 \right\}, \tag{3.8}$$

$$\mathcal{H}_{\rm sd} = -\frac{M}{s_n} \left(\tilde{\boldsymbol{l}} \cdot \hat{\boldsymbol{\sigma}}_\ell + \boldsymbol{n} \cdot \hat{\boldsymbol{\sigma}}_n \right), \tag{3.9}$$

where $s_n = 2\hbar S/(2a^d)$ is the density of staggered angular momentum, z is the number of n.n. sites of a given site, $\hat{\boldsymbol{\sigma}}_\ell$ and $\hat{\boldsymbol{\sigma}}_n$ are the uniform and staggered components of the electron spin density, and $M = J_{\rm sd} S$. The equations of motion are obtained as

$$\begin{cases} \dot{\boldsymbol{n}} &= \boldsymbol{H}_\ell \times \boldsymbol{n} + \boldsymbol{t}_n, \\ \dot{\tilde{\boldsymbol{l}}} &= \boldsymbol{H}_n \times \boldsymbol{n} + \boldsymbol{H}_\ell \times \tilde{\boldsymbol{l}} + \boldsymbol{t}_\ell, \end{cases} \tag{3.10}$$

where $\boldsymbol{H}_n = \partial \mathcal{H}_S / \partial \boldsymbol{n}$ and $\boldsymbol{H}_\ell = \partial \mathcal{H}_S / \partial \tilde{\boldsymbol{l}}$ are the effective fields coming from the spin part ($\mathcal{H}_S$), and

$$\boldsymbol{t}_n = \frac{M}{s_n} \boldsymbol{n} \times \langle \hat{\boldsymbol{\sigma}}_\ell \rangle, \tag{3.11}$$

$$\boldsymbol{t}_\ell = \frac{M}{s_n} \left\{ \boldsymbol{n} \times \langle \hat{\boldsymbol{\sigma}}_n \rangle + \tilde{\boldsymbol{l}} \times \langle \hat{\boldsymbol{\sigma}}_\ell \rangle \right\}, \tag{3.12}$$

are the spin torques from electrons ($\mathcal{H}_{\rm sd}$). We calculate $\langle \hat{\boldsymbol{\sigma}}_\ell \rangle$ and $\langle \hat{\boldsymbol{\sigma}}_n \rangle$ in response to an applied electric field $\boldsymbol{E}$ or to the time-dependent $\boldsymbol{n}$ and $\tilde{\boldsymbol{l}}$ using the Kubo formula [44, 45].

To be explicit, we consider tight-binding electrons on a two-dimensional square lattice described by

$$H_{\rm el} = -t \sum_{\langle i,j \rangle} (c_i^\dagger c_j + {\rm h.c.}) + V_{\rm imp}, \tag{3.13}$$

where the first term expresses n.n. hopping, and

$$V_{\rm imp} = u_{\rm i} \sum_l c_l^\dagger c_l + u_{\rm s} \sum_{l'} \boldsymbol{S}_{l'}^{\rm imp} \cdot c_{l'}^\dagger \boldsymbol{\sigma}\, c_{l'}, \tag{3.14}$$

defines coupling to nonmagnetic and magnetic impurities. Combined with $H_{\rm sd}$, the hopping term gives upper and lower (spin-degenerate) bands, $\pm E_{\boldsymbol{k}} = \pm\sqrt{\varepsilon_{\boldsymbol{k}}^2 + M^2}$, in a uniform AF state, where $\varepsilon_{\boldsymbol{k}} = -2t(\cos k_x + \cos k_y)$. We take a directional average of $\boldsymbol{S}_j^{\rm imp}$ with second moment $\overline{S_z^2}$ ($\overline{S_\perp^2}$) for the component parallel (perpendicular) to $\boldsymbol{n}$. In the Born approximation, they appear through $\gamma_{\rm n} = \pi n_{\rm i} u_{\rm i}^2 \nu$, $\gamma_\perp = \pi n_{\rm s} u_{\rm s}^2\, \overline{S_\perp^2}\, \nu$, and $\gamma_z = \pi n_{\rm s} u_{\rm s}^2\, \overline{S_z^2}\, \nu$, where $n_{\rm i}$ and $n_{\rm s}$ are the respective impurity concentrations, and $\nu = \frac{1}{N}\sum_{\boldsymbol{k}} \delta(|\mu| - E_{\boldsymbol{k}})$ is the density of states per spin (N is the total number of sites) with the chemical potential μ measured from the AF gap center.

Vertex correction is necessary for a proper account of spin conservation, or its weak violation. Here, it is evaluated in the ladder approximation,

$$\Pi_{\sigma\bar{\sigma}} = \frac{2}{\pi\nu\tau^2} \frac{\mu^2}{\mu^2 - M^2} \frac{1}{Dq^2 - i\omega + \tau_\varphi^{-1} + \tau_{\rm s}^{-1}}. \tag{3.15}$$

This describes diffusion, dephasing, and relaxation of transverse spin density, generalizing the result of Ref. [23] to include the effect of magnetic impurities. Here, $\tau^{-1} = 2\,[\gamma_+ + (M/\mu)^2\gamma_-]$, with $\gamma_\pm = \gamma_{\rm n} + \gamma_z \pm 2\gamma_\perp$, is the electron scattering rate, and

$$\frac{1}{\tau_\varphi} = \frac{4M^2}{\mu^2} \left[\frac{\mu^2 + M^2}{\mu^2 - M^2}\gamma_{\rm n} + 3\gamma_\perp + \frac{2(2\mu^2 + M^2)}{\mu^2 - M^2}\gamma_z \right], \tag{3.16}$$

$$\frac{1}{\tau_{\rm s}} = 4\,(\gamma_\perp + \gamma_z), \tag{3.17}$$

are, respectively, the spin-dephasing rate [46, 23] and the (transverse) spin-relaxation rate. In Eq. (3.15), q^{-1} (ω^{-1}) is the typical length (time) scale of the AF spin texture (dynamics), and D is the diffusion constant. We assume $q\ell_\varphi \ll 1$ and $\omega\tau_\varphi \ll 1$, where $\ell_\varphi = \sqrt{D\tau_\varphi}$ is the spin-dephasing length,

and let $q, \omega \to 0$ in the results. The constant terms in the denominator, $\tau_\varphi^{-1} + \tau_{\rm s}^{-1}$, reflect spin nonconservation in the electron system. The spin dephasing (τ_φ^{-1}), characteristic of AF and absent in FM, is dominated by nonmagnetic impurities and vanishes at $M = 0$ [46], whereas $\tau_{\rm s}^{-1}$ comes solely from magnetic impurities and is essentially the same as that in FM [44]. It is convenient to decompose the former as $\tau_\varphi^{-1} = \tau_{\varphi 0}^{-1} + \tau_{\varphi 1}^{-1}$, where $\tau_{\varphi 0}^{-1}$ ($\propto \gamma_{\rm n}$) is the contribution from nonmagneic impurities and $\tau_{\varphi 1}^{-1}$ is from magneic impurities. The "dissipated" spin angular momentum via $\tau_{\varphi 0}^{-1}$ is actually transferred to the AF spin system.

We calculate electron spin density induced by an external electric field $\boldsymbol{E}$ in the presence of spin texture (for current-induced torques), or induced by time-dependent spins, $\dot{\boldsymbol{n}}$ and $\dot{\tilde{\boldsymbol{l}}}$ (for damping torques). We assume weak spin relaxation, $\gamma_z, \gamma_\perp \ll \gamma_{\rm n}$, and retain terms of lowest nontrivial order. The calculations are straightforward along the lines of Refs. [44, 45, 23]; see Appendix for details.

3.3 Results

We obtained

$$\langle \hat{\boldsymbol{\sigma}}_n \rangle = -(s_n/M)\{\beta_n (\boldsymbol{v}_n \cdot \nabla)\, \boldsymbol{n} + \alpha_n \dot{\boldsymbol{n}}\}, \tag{3.18}$$

$$\langle \hat{\boldsymbol{\sigma}}_\ell \rangle = (s_n/M)\{\boldsymbol{n} \times (\boldsymbol{v}_n \cdot \nabla)\, \boldsymbol{n} - \alpha_\ell\, \dot{\tilde{\boldsymbol{l}}}\}, \tag{3.19}$$

which are consistent with previous studies [34, 35, 24, 27, 36, 37], and lead to the torques,

$$\boldsymbol{t}_n = -(\boldsymbol{v}_n \cdot \nabla)\boldsymbol{n} - \alpha_\ell\, \boldsymbol{n} \times \dot{\tilde{\boldsymbol{l}}}, \tag{3.20}$$

$$\boldsymbol{t}_\ell = -\beta_n\, \boldsymbol{n} \times (\boldsymbol{v}_n \cdot \nabla)\boldsymbol{n} - \alpha_n\, \boldsymbol{n} \times \dot{\boldsymbol{n}}. \tag{3.21}$$

We retained dominant contributions, which come from $\langle \hat{\boldsymbol{\sigma}}_\ell \rangle$ for $\boldsymbol{t}_n$, and $\langle \hat{\boldsymbol{\sigma}}_n \rangle$ for $\boldsymbol{t}_\ell$.

3.3.1 Current-induced torques

The first terms in $\boldsymbol{t}_\ell$ and $\boldsymbol{t}_n$ are current-induced torques, which are proportional to the charge current density, $\boldsymbol{j} = \sigma_{xx}\boldsymbol{E} = 2e^2 D\nu \boldsymbol{E}$, via

$$\boldsymbol{v}_n = -\frac{\hbar}{2e s_n} \mathcal{P}_n \boldsymbol{j}. \tag{3.22}$$

The velocity $\boldsymbol{v}_n$ quantifies the STT, and we identify

$$\mathcal{P}_n = \frac{\mu M}{\mu^2 - M^2}, \tag{3.23}$$

to be the conversion factor from a charge current to STT. Note that $|\mathcal{P}_n|$ can be significantly larger than unity near the AF gap edge ($|\mu| \gtrsim |M|$). This contrasts to the case of FM, in which the corresponding factor $|P|$ is less than or equal to unity. The current-induced torque in $\boldsymbol{t}_\ell$ is characterized by a dimensionless parameter,

$$\beta_n = \frac{2(\gamma_\perp + \gamma_z)}{M} = \frac{\hbar}{2M\tau_{\rm s}}, \tag{3.24}$$

which originates from magnetic impurities, i.e., from spin relaxation, and is therefore a dissipative torque. The spin dephasing due to nonmagnetic impurities ($\tau_{\varphi 0}^{-1}$) is microscopically a reactive process and does not contribute to β_n, whereas that from $\tau_{\varphi 1}^{-1}$, combined with the self-energy terms, results in a contribution proportional to $\tau_{\rm s}^{-1}$. Along with the contribution originating from $\tau_{\rm s}^{-1}$ in Eq. (3.15), it leads to Eq. (3.24). The obtained two current-induced torques are related via $\beta_n \boldsymbol{n}\times$, which is reminiscent of the relation between the reactive and dissipative torques in FM; we call the former $[-(\boldsymbol{v}_n\cdot\nabla)\boldsymbol{n}]$ the STT in AF, and the latter $[-\beta_n \boldsymbol{n}\times(\boldsymbol{v}_n\cdot\nabla)\boldsymbol{n}]$ the β_n torque. The expression of β_n in terms of $\tau_{\rm s}$ and $M = J_{sd}S$ is also shared by FM [44, 40].

The above two current-induced torques change their signs across the AF gap [see Eq. (3.23)], reflecting the fact that electrons in the upper and lower AF bands have mutually opposite spin directions. This feature of the STT was suggested in Ref. [35]. Interestingly, the driving direction is opposite to the naive expectation based on the two-FM picture of AF. Namely, for $\mu < 0$, the spin polarization on the Fermi surface is positive (dominated by majority spin carriers) but the driving direction is opposite to the direction of electron flow. This is due to the intersublattice hopping in AF, namely, the electron spins exert torques on oppositely pointing neighboring spins, so the sign of the torques is reversed from that of FMs [1]. The same is true for $\mu > 0$.

[1] We have confirmed this by introducing the next n.n. hopping t'. As t' starts dominating, the sign of the STT changes from negative to positive in the $\mu < 0$ region, and vice versa for $\mu > 0$, in conformity with the change of transport character from AF like to FM like [47]. The derivation for this is given in the next chapter. Note that the torques in FM also change their signs in a tight-binding model as μ is increased from the band bottom to the top since the majority/minority spins are switched and the sign of P is reversed.

3.3.2 Damping torques

The second terms in Eqs. (3.20) and (3.21) describe damping. The damping parameters are calculated as

$$\alpha_n = \left\{ \gamma_\perp + \gamma_z + \frac{M^2}{\mu^2}(\gamma_\perp - \gamma_z) \right\} \frac{2\hbar\nu}{s_n}, \tag{3.25}$$

$$\alpha_\ell = \frac{(\mu^2 - M^2)(\mu^2 + M^2)}{\mu^2} \frac{\nu}{s_n} \tau. \tag{3.26}$$

While α_n arises from spin relaxation (magnetic impurities), α_ℓ does not necessitate it. Rather, α_ℓ is proportional to τ, like conductivity, hence can be very large in good metals. These features were pointed out in Refs. [48, 49, 50] based on the first-principles calculation.

It is interesting to compare α_n with the Gilbert damping in FM,

$$\alpha_{\rm F} = \sum_\sigma (\gamma_{z,\sigma}\nu_{\bar\sigma} + \gamma_{\perp,\sigma}\nu_\sigma) \frac{\hbar}{s_0}, \tag{3.27}$$

obtained based on the same spin-relaxation model (magnetic impurities) [44]. Here, $\gamma_{\alpha,\sigma} = \pi n_s u_s^2 \overline{S_\alpha^2} \nu_\sigma$ ($\alpha = \perp, z$), ν_σ ($\sigma = \uparrow, \downarrow$) is the density of states of electrons with spin σ, and $s_0 = \hbar S/a^d$ is the angular-momentum density. We see that in the limit of spin-degenerate bands ($\nu_\uparrow = \nu_\downarrow$) and isotropic magnetic impurities ($\gamma_\perp = \gamma_z$), the above expressions of α_n (for AF) and $\alpha_{\rm F}$ (for FM) coincide. Therefore, in the current model of AF, the ratio β_n/α_n is of order unity, similar to FM [39].

3.3.3 Equations of AF spin dynamics

With the obtained torques and $\mathcal{H}_S$ [Eq. (3.8)], the equations of motion are explicitly written as

$$\dot{\boldsymbol{n}} = \tilde{J}\, \tilde{\boldsymbol{l}} \times \boldsymbol{n} - (\boldsymbol{v}_n \cdot \nabla)\, \boldsymbol{n}, \tag{3.28}$$

$$\begin{aligned} \dot{\tilde{\boldsymbol{l}}} = & -(c^2 \tilde{J}^{-1} \nabla^2 \boldsymbol{n} + \tilde{K} n^z \hat{z}) \times \boldsymbol{n} \\ & + (\alpha_n \dot{\boldsymbol{n}} + \beta_n (\boldsymbol{v}_n \cdot \nabla)\, \boldsymbol{n}) \times \boldsymbol{n} \\ & + \boldsymbol{n}\, [\tilde{\boldsymbol{l}} \cdot (\boldsymbol{v}_n \cdot \nabla) \boldsymbol{n}], \end{aligned} \tag{3.29}$$

with $c = (zJSa)/(\hbar\sqrt{d})$, $\tilde{J} = 2zJS/\hbar$, and $\tilde{K} = 2SK/\hbar$. Damping terms in the first equation are dropped as they are higher order in $\tilde{\boldsymbol{l}}$. Solving Eq. (3.28)

for $\tilde{\boldsymbol{l}}$ as $\tilde{\boldsymbol{l}} = \tilde{J}^{-1}\boldsymbol{n}\times[\dot{\boldsymbol{n}} + (\boldsymbol{v}_n\cdot\nabla)\,\boldsymbol{n}]$, and substituting it in Eq. (3.29), one can obtain a closed equation for $\boldsymbol{n}$,

$$\begin{aligned}\ddot{\boldsymbol{n}}\times\boldsymbol{n} = (c^2\,\nabla^2\boldsymbol{n} + \tilde{J}\tilde{K}n_z\hat{z})\times\boldsymbol{n} \\ - \tilde{J}(\alpha_n\dot{\boldsymbol{n}} + \beta_n(\boldsymbol{v}_n\cdot\nabla)\,\boldsymbol{n})\times\boldsymbol{n} \\ - [(\boldsymbol{v}_n\cdot\nabla)\,\dot{\boldsymbol{n}}]\times\boldsymbol{n}.\end{aligned} \tag{3.30}$$

This differs slightly from Ref. [35] due to the difference in $H_{\rm sd}$ (i.e., $\boldsymbol{l}$ vs. $\tilde{\boldsymbol{l}}$), and leads to the magnon dispersion,

$$\begin{aligned}\omega = \sqrt{c^2\boldsymbol{q}^2 + \tilde{J}\tilde{K} + (\boldsymbol{v}_n\cdot\boldsymbol{q} - i\tilde{J}\alpha_n)^2/4 + i\tilde{J}\beta_n\boldsymbol{v}_n\cdot\boldsymbol{q}} \\ \pm\,(\boldsymbol{v}_n\cdot\boldsymbol{q} - i\tilde{J}\alpha_n)/2,\end{aligned} \tag{3.31}$$

where damping enters only through α_n and β_n.

3.3.4 Domain wall motion

Here we study the AF DW motion using collective coordinates. Since $\mathcal{L}_S$ [Eq. (3.7)] is written with $\boldsymbol{n}$ and $\tilde{\boldsymbol{l}}$, we consider collective coordinates for both $\boldsymbol{n}$ and $\tilde{\boldsymbol{l}}$ [43]. Assuming for $\boldsymbol{n} = (\sin\theta\cos\phi, \sin\theta\sin\phi, \cos\theta)$ a DW form, $\cos\theta(x,t) = \pm\tanh\left(\frac{x-X(t)}{\lambda}\right)$ and $\phi(x,t) = \phi_0(t)$, where $\lambda = a\sqrt{zJ/4Kd}$ is the DW width, we treat the DW position $X(t)$ and the angle $\phi_0(t)$ as dynamical variables [17]. As for $\tilde{\boldsymbol{l}}$, we expand it as [43]

$$\tilde{\boldsymbol{l}}(x,t) = [\,l_\theta(t)\,\boldsymbol{e}_\theta + l_\phi(t)\,\boldsymbol{e}_\phi\,]\,\varphi_0(x) + \cdots, \tag{3.32}$$

where $\boldsymbol{e}_\theta \equiv \partial_\theta\boldsymbol{n}$ and $\boldsymbol{e}_\phi \equiv \boldsymbol{n}\times\boldsymbol{e}_\theta$ are orthonormal vectors normal to $\boldsymbol{n}$. The function $\varphi_0(x) = \left[\cosh\frac{x-X}{\lambda}\right]^{-1}$ reflects the spatial profile of $\boldsymbol{n}\times\dot{\boldsymbol{n}}$, and naturally extracts l_θ and l_ϕ in the first term of $\mathcal{L}_S$ [Eq. (3.7)]. The obtained Lagrangian, $L_{\rm DW} = 2s_n(\pm\dot{X}l_\phi - \lambda\dot{\phi}_0 l_\theta) - H_S$, shows that l_ϕ and l_θ are canonical conjugate to X and ϕ_0, respectively. The equations of motion are given by

$$\pm\lambda\,\dot{l}_\phi = \beta_n v_n - \alpha_n\dot{X}, \tag{3.33}$$

$$\pm\dot{X} = \pm v_n + v_J\,l_\phi + \alpha_\ell\lambda\dot{l}_\phi, \tag{3.34}$$

$$\dot{l}_\theta = \alpha_n\,\dot{\phi}_0, \tag{3.35}$$

$$\lambda\,\dot{\phi}_0 = -v_J l_\theta - \alpha_\ell\lambda\dot{l}_\theta, \tag{3.36}$$

where $v_J = 4JS\lambda/\hbar$, and $\pm$ is the topological charge of the AF DW. The first two equations describe the translational motion, and the remaining two describe the rotational motion of the DW plane (defined by the Néel vector). Unlike in FM [51], these two motions are decoupled in AF. The term $\pm v_n$ in Eq. (3.34) describes the spin-transfer effect, and $\beta_n v_n$ in Eq. (3.33) describes the momentum-transfer effect (a force on the DW). The terms with α_ℓ are negligible in effect, but retained here for the sake of comparison with FM (see below).

Let us overview the translational motion of AF DW under a stationary v_n [24]. When $\alpha_n = \beta_n = 0$, l_ϕ is a constant of motion. With an initial condition $l_\phi = 0$ (no canting), the DW moves at a constant velocity $\dot{X} = v_n$ by the spin-transfer effect [35]. If the DW is initially canted, $l_\phi = l_\phi^0$, the constant velocity is modified to $\dot{X} = v_n \pm v_J\, l_\phi^0$. For finite α_n, l_ϕ is no longer conserved, and approaches a terminal value, $l_\phi \to \mp(1 - \beta_n/\alpha_n)(v_n/v_J)$. Then, from Eq. (3.34), the DW velocity approaches

$$\dot{X} \;\to\; v_n - \left(1 - \frac{\beta_n}{\alpha_n}\right) v_n = \frac{\beta_n}{\alpha_n}\, v_n, \tag{3.37}$$

which is solely determined by the β_n torque. If $\beta_n = 0$, the spin-transfer effect is completely nullified by the canting $l_\phi = \pm v_n/v_J$, and the aforementioned steady movement eventually ceases [24]. This is quite similar to the intrinsic pinning in FM. For finite β_n, canting l_ϕ is reduced, and the cancellation of the spin-transfer effect is incomplete. Finally, the case $\beta_n = \alpha_n$ is special in that there is no canting, and the spin-transfer effect is undisturbed.

It is instructive to make a more detailed comparison with FM. In FM, the current-driven DW motion is described by

$$\pm\lambda\,\dot{\phi}_0 = \beta v_{\rm s} - \alpha\dot{X}, \tag{3.38}$$

$$\pm\dot{X} = \pm v_{\rm s} + v_K \sin 2\phi_0 + \alpha\lambda\dot{\phi}_0, \tag{3.39}$$

where, now, X and ϕ_0 are coupled. (ϕ_0 here is defined by the uniform magnetization, and $\pm$ is the topological charge of the FM DW.) A close similarity to Eqs. (3.33) and (3.34) is evident, and here ϕ_0 plays the role of l_ϕ. The effect of current appears in $v_{\rm s} = -(\hbar/2es_0)Pj$, where P is the current polarization factor, and the velocity $v_K = K_\perp S\lambda/2\hbar$ is defined with the hard-axis anisotropy constant $K_\perp$. At low current, $v_{\rm s} < v_K$, and with $\beta = 0$, the DW plane tilts by $\phi_0 = (1/2)\sin^{-1}(v_{\rm s}/v_K)$ and the DW ceases to

move, $\dot{X} = 0$. This is the intrinsic pinning in FM [51, 52]. If $v_{\rm s}$ exceeds v_K, v_K can not nullify the spin-transfer effect $v_{\rm s}$ and the DW is released from intrinsic pinning. The corresponding term in Eq. (3.34) has the linearised form, $v_J\, l_\phi$, which is justified since v_J of AF is much larger than v_K of FM (by 2-3 orders of magnitude), and the intrinsic pinning is robust in AF. It is interesting to note the contrasting origins of intrinsic pinning; in FM it is the explicit breaking of spin rotation symmetry, $K_\perp$, whereas in AF it is the AF order itself, i.e., spontaneous breaking. Finally, the case $\alpha = \beta$ provides a special solution $\phi_0 = 0$ and $\dot{X} = v_s$, similar to the case $\alpha_n = \beta_n$ for AF.

Recently, current-assisted field-driven DW motion was experimentally studied in a *ferrimagnetic* GdFeCo near its angular-momentum compensation temperature [16]. The authors analyzed the data by the Landau-Lifshitz-Gilbert equation for the *uniform moment* $\boldsymbol{m}$ (parallel to $\boldsymbol{n}$), and obtained a very large, negative value of $\beta/\alpha \simeq -100$. They assumed $\sim \beta P \boldsymbol{j}$ for the β-torque coefficient (that acts on $\boldsymbol{m}$), with a small factor P ($\simeq 0.1$) included. If, however, the main driving is the β_n torque that acts on the *Néel vector* $\boldsymbol{n}$, as studied in the present work, we would conclude $\mathcal{P}_n \beta_n/\alpha_n \simeq -10$ (see Appendix for details). While $\beta_n/\alpha_n \simeq 1$ as in FM (for positive $J_{\rm sd}$ [2] [53]), $|\mathcal{P}_n|$ can be significantly larger than unity near the AF gap edge. Therefore, the large value of $|\mathcal{P}_n| \sim 10$ may lie within the scope of the present results. The negative sign can be explained likewise from $\mathcal{P}_n$ with a negative μ, which reflects intersublattice hopping in AF. Such "antiferromagnetic transport" in GdFeCo is supported by a recent magnetoresistance measurement [54].

In conclusion, we have presented a microscopic model calculation of current-induced torques and damping torques in AF metals, paying attention to the effects of spin relaxation (and spin dephasing). A formulation in terms of the Néel vector and physical magnetization is given to study the AF spin dynamics in metallic AFs with s-d exchange interaction. The current-induced torques are found to be opposite in direction to those of FMs, reflecting the AF transport character, and the current-to-STT conversion factor can be significantly larger than that in FM. These results seem to be relevant to the recent experiment on GdFeCo.

[2] A negative β (or β_n) parameter is realized if $J_{\rm sd}$ is negative [53], where the STT is reversed but the β torque is not. In contrast, the sign change in μ across the AF gap in our present result brings a sign change in both STT and the β_n torque, and their ratio, i.e., the β_n parameter remains positive (if $J_{\rm sd} > 0$).

3.A Appendix: Model of electrons

The conduction electrons are considered in the tight-binding Hamiltonian and s-d exchange interaction,

$$H_{\rm el} = -t \sum_{\langle i,j \rangle} (c_i^\dagger c_j + {\rm h.c.}) + V_{\rm imp}, \tag{3.40}$$

$$H_{\rm sd} = -J_{\rm sd} \sum_i \boldsymbol{S}_i \cdot c_i^\dagger \boldsymbol{\sigma}\, c_i \tag{3.41}$$

where $c_i^\dagger = (c_{i\uparrow}^\dagger, c_{i\downarrow}^\dagger)$ is the electron creation operator at site i. The first term in $H_{\rm el}$ describes the electron hopping (with amplitude t). The second term describes the coupling to nonmagnetic and magnetic impurities,

$$V_{\rm imp} = u_{\rm i} \sum_{i \in {\rm C}} c_i^\dagger c_i + u_{\rm s} \sum_{j \in {\rm C}'} \boldsymbol{S}_j^{\rm imp} \cdot c_j^\dagger \boldsymbol{\sigma}\, c_j, \tag{3.42}$$

where $u_{\rm i}$ and $u_{\rm s}$ are the strengths of the coupling, and C and C$'$ are the sets of positions of nonmagnetic and magnetic impurities, respectively. The number of impurities on A and B sublattices are assumed equal.

The coupling of conduction electrons to the localized spins is introduced by $H_{\rm sd}$, where $\boldsymbol{\sigma} = {}^t(\sigma_x, \sigma_y, \sigma_z)$ are Pauli matrices and $J_{\rm sd}$ is the coupling constant. With $\tilde{\boldsymbol{l}}$ and $\boldsymbol{n}$, its density is written as

$$\mathcal{H}_{\rm sd} = -\frac{M}{s_n} (\tilde{\boldsymbol{l}} \cdot \hat{\boldsymbol{\sigma}}_\ell + \boldsymbol{n} \cdot \hat{\boldsymbol{\sigma}}_n), \tag{3.43}$$

where $\hat{\boldsymbol{\sigma}}_\ell$ ($\hat{\boldsymbol{\sigma}}_n$) is the uniform (staggered) spin density of electrons, $s_n = 2\hbar S/(2a^2)$, and $M = J_{\rm sd} S$.

We introduce a local unitary transformation in the electron spin space that sorts the Néel vector at each site i to the $\hat{z}$ direction [45, 55],

$$U_i^\dagger (\boldsymbol{n}_i \cdot \boldsymbol{\sigma})\, U_i = \sigma^z. \tag{3.44}$$

We define an $SU(2)$ spin gauge field A_{ij} by

$$U_i^\dagger U_j = e^{iA_{ij}}. \tag{3.45}$$

This is associated with the hopping from site j to i, and satisfies $A_{ij} = -A_{ji}$. It contains information about the texture of the Néel vector. We

assume slow spatial variation for $\boldsymbol{n}_i$, therefore, A_{ij} is small and can be treated perturbatively. We define the Fourier component $A_\mu(\boldsymbol{q})$ by

$$A_{ij} = \sum_{\boldsymbol{q}} A_\mu(\boldsymbol{q})\, e^{i\boldsymbol{q}\cdot(\boldsymbol{r}_i+\boldsymbol{r}_j)/2}, \tag{3.46}$$

where $\hat{\mu} = \boldsymbol{r}_j - \boldsymbol{r}_i$, and expand it with Pauli matrices,

$$A_\mu(\boldsymbol{q}) = \sum_{\alpha=x,y,z} A_\mu^\alpha(\boldsymbol{q})\,\frac{\sigma^\alpha}{2} \equiv \boldsymbol{A}_\mu \cdot \frac{\boldsymbol{\sigma}}{2}. \tag{3.47}$$

The corresponding 3×3 matrix $\mathcal{R}_i$ is defined by

$$U_i^\dagger \sigma^\alpha U_i = \mathcal{R}_i^{\alpha\beta}\sigma^\beta. \tag{3.48}$$

To first order in the spin gauge field, the Hamiltonian in the Fourier representation is written as [23]

$$\tilde{H}_{\rm el} = \sum_{\boldsymbol{k}} \psi_{\boldsymbol{k}}^\dagger \varepsilon_{\boldsymbol{k}} \tau_1 \psi_{\boldsymbol{k}} + \frac{1}{2}\sum_{i=x,\,y}\sum_{\boldsymbol{k},\boldsymbol{q}} (\partial_i \varepsilon_{\boldsymbol{k}})(\psi_{\boldsymbol{k}_+}^\dagger \sigma^\alpha \tau_1\, \psi_{\boldsymbol{k}_-}) A_i^\alpha(\boldsymbol{q}) + \tilde{H}_{\rm imp}, \tag{3.49}$$

$$\tilde{H}_{\rm sd} = -M\sum_{\boldsymbol{k}} \psi_{\boldsymbol{k}}^\dagger \sigma^z \tau_3 \psi_{\boldsymbol{k}}, \tag{3.50}$$

where τ_n and σ^α are Pauli matrices that act in sublattice (A or B) and spin ($\uparrow$ or $\downarrow$) spaces, respectively, $\varepsilon_{\boldsymbol{k}} = -2t(\cos k_x + \cos k_y)$, $\boldsymbol{k}_\pm = \boldsymbol{k} \pm \frac{\boldsymbol{q}}{2}$, and we set the lattice constant to unity. The electron creation operator in the sublattice representation is now given by $\psi_{\boldsymbol{k}}^\dagger = (\tilde{c}_{{\rm A}\boldsymbol{k}\uparrow}^\dagger, \tilde{c}_{{\rm A}\boldsymbol{k}\downarrow}^\dagger, \tilde{c}_{{\rm B}\boldsymbol{k}\uparrow}^\dagger, \tilde{c}_{{\rm B}\boldsymbol{k}\downarrow}^\dagger)$, where $\tilde{c}_{{\rm A/B}\boldsymbol{k}\sigma}^\dagger$ is the Fourier representation of the electron creation operator in the rotated frame with spin σ and on sublattice A/B. The $\boldsymbol{k}$-integral is taken in the reduced Brillouin zone, $|k_x + k_y| \le \pi$. Note that in $\tilde{H}_{\rm sd}$, the coupling to $\boldsymbol{l}$ is dropped since it only gives higher order terms in $\tilde{\boldsymbol{l}}$.

3.B Appendix: Calculation of spin torques

3.B.1 Formalism

We calculate the conduction electron spin density, $\tilde{\boldsymbol{\sigma}}\tau_\beta = \sum_{\boldsymbol{k}} \psi_{\boldsymbol{k}}^\dagger \boldsymbol{\sigma}\tau_\beta \psi_{\boldsymbol{k}}$, in response to an applied electric field E_i using the Kubo formula. In particular, we are interested in the uniform density, $\langle \hat{\boldsymbol{\sigma}}_\ell \rangle = \frac{1}{2}\mathcal{R}\langle \tilde{\boldsymbol{\sigma}}\tau_0 \rangle$, and the

staggered density, $\langle \hat{\boldsymbol{\sigma}}_n \rangle = \frac{1}{2}\mathcal{R}\langle \tilde{\boldsymbol{\sigma}}\tau_3 \rangle$. We dropped the wave vector carried by the spin density operator since the spin gauge field already contains a spatial derivative. The Kubo formula is given by

$$\langle O \rangle_{\rm ne} = \lim_{\omega\to 0} \frac{K_i(\omega + i0) - K_i(0)}{i\omega} E_i, \tag{3.51}$$

$$K_i(i\omega_\lambda) = \int_0^\beta d\tau e^{i\omega_\lambda \tau} \langle T_\tau O(\tau) \tilde{J}_i \rangle, \tag{3.52}$$

where $O = \sigma^\alpha$ or $\sigma^\alpha\tau_3$. The current operator in the rotated frame is given to first order in spin gauge field by

$$\tilde{J}_i = -e\sum_{\boldsymbol{k}} \psi^\dagger_{\boldsymbol{k}}[(\partial_i \varepsilon_{\boldsymbol{k}})\tau_1]\psi_{\boldsymbol{k}} - e\sum_{\boldsymbol{k},\boldsymbol{q}} \psi^\dagger_{\boldsymbol{k}+\frac{\boldsymbol{q}}{2}}[(\partial_i^2 \varepsilon_{\boldsymbol{k}})\sigma^\alpha\tau_1]\psi_{\boldsymbol{k}-\frac{\boldsymbol{q}}{2}} A_i^\alpha(\boldsymbol{q}). \tag{3.53}$$

The average $\langle \cdots \rangle$ is taken in the thermal equilibrium state, determined by $\tilde{H}_{\rm el} + \tilde{H}_{\rm sd}$, to first order in the spin gauge field.

The calculation is executed using the Green's function of the tight-binding electrons in a homogeneous antiferromagnetic state. The retarded Green's function is given by

$$G^R_{\boldsymbol{k}} = \mu^R_{\boldsymbol{k}} + T^R_{\boldsymbol{k}}\tau_1 + J^R_{\boldsymbol{k}}\sigma^z\tau_3, \tag{3.54}$$

where $\mu^R = (\mu + i\gamma_0)/D^R_{\boldsymbol{k}}$, $T^R = \varepsilon_{\boldsymbol{k}}/D^R_{\boldsymbol{k}}$, $J^R = (-M + i\gamma_3)/D^R_{\boldsymbol{k}}$, and $D^R_{\boldsymbol{k}} = (\mu + i\gamma_0)^2 - \varepsilon^2_{\boldsymbol{k}} - (M - i\gamma_3)^2$. The damping constants are calculated in the Born approximation (see Fig. 4.1 (a)) as $\gamma_0 = \gamma_{\rm n} + \gamma_z + 2\gamma_\perp$ and $\gamma_3 = (\gamma_{\rm n} + \gamma_z - 2\gamma_\perp)M/\mu$, with $\gamma_{\rm n} = \pi n_{\rm i} u_{\rm i}^2 \nu$ from nonmagnetic impurities and

$$\gamma_\perp = \pi n_{\rm s} u_{\rm s}^2 \, \overline{S^2_\perp} \, \nu, \quad \gamma_z = \pi n_{\rm s} u_{\rm s}^2 \, \overline{S^2_z} \, \nu, \tag{3.55}$$

from magnetic impurities. We wrote $n_{\rm i}$ ($n_{\rm s}$) for the nonmagnetic (magnetic) impurity concentration, and we took the directional average of magnetic impurity spins in the rotated frame, $\tilde{\boldsymbol{S}}^{\rm imp} = \mathcal{R}^{-1}\boldsymbol{S}^{\rm imp}$, as $\langle \tilde{S}^{\rm imp}_\alpha \rangle_{\rm imp} = 0$, $\langle (\tilde{S}^{\rm imp}_{j,z})^2 \rangle_{\rm imp} \equiv \overline{S^2_z}$, and $\langle (\tilde{S}^{\rm imp}_{j,x})^2 \rangle_{\rm imp} = \langle (\tilde{S}^{\rm imp}_{j,y})^2 \rangle_{\rm imp} \equiv \overline{S^2_\perp}$. The density of states is given by $\nu = \nu(\mu) = \frac{1}{N}\sum_{\boldsymbol{k}} \delta(|\mu| - E_{\boldsymbol{k}})$ where $E_{\boldsymbol{k}} = \sqrt{\varepsilon^2_{\boldsymbol{k}} + M^2}$, and μ is the chemical potential.

To work in consistency with the Born approximation, we consider the impurity-ladder vertex correction as shown in Fig. 4.1 (b). The relevant

correction comes from retarded and advanced Green's functions with opposite spins, and is obtained as

$$\Pi_{\sigma\bar{\sigma}} = \frac{2}{\pi\nu}\frac{4\gamma^2\mu^2}{\mu^2 - M^2}\,\frac{1}{Dq^2 - i\omega + \tau_\varphi^{-1} + \tau_{\rm s}^{-1}} \tag{3.56}$$

$$\simeq \frac{2\gamma}{\pi\nu}\cdot\frac{\gamma_{\rm n} - \gamma_z}{\frac{M^2}{\mu^2}\gamma_{\rm n} + \gamma_z + (1 - \frac{M^2}{\mu^2})\gamma_\perp}, \tag{3.57}$$

where $\gamma = \gamma_0 + (M/\mu)\gamma_3$ is the electron scattering rate,

$$\frac{1}{\tau_\varphi} = \frac{4M^2}{\mu^2}\left[\frac{\mu^2 + M^2}{\mu^2 - M^2}\,\gamma_{\rm n} + 3\gamma_\perp + \frac{2(2\mu^2 + M^2)}{\mu^2 - M^2}\,\gamma_z\right], \tag{3.58}$$

$$\frac{1}{\tau_{\rm s}} = 4\,(\gamma_\perp + \gamma_z), \tag{3.59}$$

are the spin-dephasing and spin-relaxation rates, respectively. We decompose the former into

$$\frac{1}{\tau_{\varphi 0}} = \frac{4M^2}{\mu^2}\frac{\mu^2 + M^2}{\mu^2 - M^2}\,\gamma_{\rm n}, \tag{3.60}$$

$$\frac{1}{\tau_{\varphi 1}} = \frac{4M^2}{\mu^2}\left[3\gamma_\perp + \frac{2(2\mu^2 + M^2)}{\mu^2 - M^2}\,\gamma_z\right]. \tag{3.61}$$

3.B.2 Uniform spin density

The uniform spin density is finite without magnetic impurities, so magnetic impurities are not considered here. The first two diagrams in Fig. 4.1 (d) give

$$\begin{aligned}\text{(d1)} + \text{(d2)} &= \frac{1}{i\omega}\frac{-\omega}{2\pi i}\frac{1}{2}A_i^\alpha\sum_{\boldsymbol{k}}(\partial_i\varepsilon_{\boldsymbol{k}})^2\mathrm{tr}(\boldsymbol{\sigma}^\perp G^R\sigma^\alpha\tau_1 G^R\tau_1 G^A) + \text{c.c.}\\ &= \boldsymbol{A}_i^\perp\frac{2\nu\tau}{\mu}\left[\frac{-2M^2}{\mu^2 + M^2}\langle\!\langle(\partial_i\varepsilon_{\boldsymbol{k}})^2\rangle\!\rangle - \langle\!\langle\varepsilon_{\boldsymbol{k}}(\partial_i^2\varepsilon_{\boldsymbol{k}})\rangle\!\rangle\right],\end{aligned} \tag{3.62}$$

where $\boldsymbol{A}_i^\perp = \boldsymbol{A}_i - A_i^z\hat{z}$ and $\langle\!\langle\cdots\rangle\!\rangle = \nu^{-1}\frac{1}{N}\sum_{\boldsymbol{k}}(\cdots)\delta(|\mu| - E_{\boldsymbol{k}})$. The third diagram (d3) gives

$$\begin{aligned}\text{(d3)} &= \frac{1}{i\omega}\frac{-\omega}{2\pi i}\frac{1}{2}A_i^\alpha\sum_{\boldsymbol{k}}(\partial_i^2\varepsilon_{\boldsymbol{k}})\,\mathrm{tr}\left[\boldsymbol{\sigma}^\perp G^R\sigma^\alpha\tau_1 G^A\right]\\ &= \boldsymbol{A}_i^\perp\frac{2\nu\tau}{\mu}\langle\!\langle\varepsilon_{\boldsymbol{k}}(\partial_i^2\varepsilon_{\boldsymbol{k}})\rangle\!\rangle,\end{aligned} \tag{3.63}$$

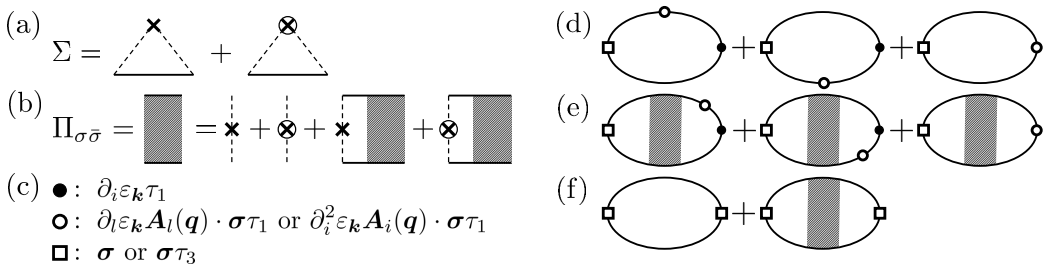

Figure 3.1: Feynman diagrams for the current-induced spin torques and damping torques. (a) and (b) show the treatment of random impurities, and (c)-(f) show the response functions (electron spin density in response to the electric field $\boldsymbol{E}$ or time-dependent uniform/staggered magnetization, $\boldsymbol{n}$ or $\tilde{\boldsymbol{l}}$). The solid line represents the electron Green's function, and the dashed line with a cross (circled cross) represents nonmagnetic (magnetic) impurity scattering. (a) Self-energy in the Born approximation. (b) Four-point vertex with impurity ladder. The upper (lower) electron line is in the retarded (advanced) branch and has spin σ ($\bar{\sigma}$). (c) Definition of vertices. The filled circle represents the current vertex $(\partial_i \varepsilon_{\boldsymbol{k}})\tau_1$, where the direction i is coupled to the external electric field E_i. The empty circles represent vertices that contain the spin gauge field $\boldsymbol{A}$ coming either from the perturbation Hamiltonian $(\partial_l \varepsilon_{\boldsymbol{k}})\boldsymbol{A}_l(\boldsymbol{q}) \cdot \boldsymbol{\sigma}\tau_1$ or from the current vertex $(\partial_i^2 \varepsilon_{\boldsymbol{k}})\boldsymbol{A}_i(\boldsymbol{q}) \cdot \boldsymbol{\sigma}\tau_1$. The empty square is the uniform ($\boldsymbol{\sigma}$) or staggered ($\boldsymbol{\sigma}\tau_3$) spin density. Diagrams in (d) and (e) represent current-induced torques, in which the right vertex represents the charge current that couples to $\boldsymbol{E}$. (d) Diagrams first order in $\boldsymbol{A}$. The so-called Fermi-sea terms, consisting of only retarded or advanced Green's functions, also need to be retained for the staggered spin density. (e) Diagrams first order in $\boldsymbol{A}$ with ladder vertex corrections. Diagrams in (f) represent damping torques.

which cancels the term $\sim \langle\!\langle \varepsilon_{\boldsymbol{k}} (\partial_i^2 \varepsilon_{\boldsymbol{k}}) \rangle\!\rangle$ in (d1)+(d2). In Fig. 4.1 (e), the first two diagrams, (e1) and (e2), give

$$\begin{aligned}
\text{(e1)} + \text{(e2)} &= \frac{1}{4^2} \frac{1}{i\omega} \frac{-\omega}{2\pi i} \frac{1}{2} A_i^\alpha \sum_{\boldsymbol{k}'} \mathrm{tr} \left[\sigma^\perp G^R \sigma^\perp G^A \right] \Pi_{\sigma\bar{\sigma}} \\
&\quad \times \left\{ \sum_{\boldsymbol{k}} (\partial_i \varepsilon_{\boldsymbol{k}})^2 \mathrm{tr} (\sigma^\perp G^R \sigma^\alpha \tau_1 G^R \tau_1 G^A) + \text{c.c.} \right\} \\
&= \boldsymbol{A}_i^\perp \frac{2\nu\tau_{\varphi 0}}{\mu} \left[\frac{-2M^2}{\mu^2 + M^2} \langle\!\langle (\partial_i \varepsilon_{\boldsymbol{k}})^2 \rangle\!\rangle - \langle\!\langle \varepsilon_{\boldsymbol{k}} (\partial_i^2 \varepsilon_{\boldsymbol{k}}) \rangle\!\rangle \right], \qquad (3.64)
\end{aligned}$$

where $\Pi_{\sigma\bar{\sigma}}$ is the ladder vertex part [Eq. (3.57)], and we defined $\frac{\mu^2 - M^2}{2M^2} \tau = \tau_{\varphi 0}$. The third diagram (e3) can be similarly calculated,

$$\text{(e3)} = \boldsymbol{A}_i^\perp \frac{2\nu\tau_{\varphi 0}}{\mu} \langle\!\langle \varepsilon_{\boldsymbol{k}} (\partial_i^2 \varepsilon_{\boldsymbol{k}}) \rangle\!\rangle. \qquad (3.65)$$

Thus, the total uniform spin density in the rotated frame is obtained as

$$\begin{aligned}
\langle \tilde{\boldsymbol{\sigma}}^\perp \rangle_{\text{ne}} = \text{Fig. 4.1 (d)+(e)} &= \boldsymbol{A}_i^\perp (\tau + \tau_{\varphi 0}) \frac{2\nu}{\mu} \frac{-2M^2}{\mu^2 + M^2} \langle\!\langle (\partial_i \varepsilon_{\boldsymbol{k}})^2 \rangle\!\rangle (-eE_i) \\
&= \boldsymbol{A}_i^\perp \tau \frac{2\nu}{\mu} \langle\!\langle (\partial_i \varepsilon_{\boldsymbol{k}})^2 \rangle\!\rangle e E_i \\
&= \boldsymbol{A}_i^\perp \frac{2\mu}{\mu^2 - M^2} \frac{j_i}{2e}, \qquad (3.66)
\end{aligned}$$

where $\boldsymbol{j} = 2e^2 D \nu \boldsymbol{E} = 2e^2 \frac{\mu^2 - M^2}{\mu^2} \langle\!\langle (\partial_i \varepsilon_{\boldsymbol{k}})^2 \rangle\!\rangle \nu\tau \boldsymbol{E}$ is the electric current density [23]. The spin density in the laboratory frame is obtained from $\mathcal{R} \boldsymbol{A}_i^\perp = -\boldsymbol{n} \times \partial_i \boldsymbol{n}$,

$$\langle \boldsymbol{\sigma}^\perp \rangle_{\text{ne}} = \mathcal{R} \langle \tilde{\boldsymbol{\sigma}}^\perp \rangle_{\text{ne}} = -\boldsymbol{n} \times \partial_i \boldsymbol{n} \frac{2\mu}{\mu^2 - M^2} \frac{j_i}{2e}. \qquad (3.67)$$

3.B.3 Staggered spin density

The staggered spin density vanishes without magnetic impurities, so they must be considered. Note that since the staggered spin density is zeroth order in the scattering time τ, the so-called "Fermi-sea terms" that contain only advanced or retarded Green's functions need to be retained.

Let us first calculate the Fermi-surface terms. The first two diagrams in Fig. 4.1 (d) without vertex correction are calculated as

$$\begin{aligned}[(\mathrm{d1})+(\mathrm{d2})]^{\mathrm{surf}} &= \frac{1}{i\omega}\frac{-\omega}{2\pi i}\frac{1}{2}A_i^\alpha \sum_{\boldsymbol{k}}(\partial_i\varepsilon_{\boldsymbol{k}})^2\,\mathrm{tr}\left[\sigma^\perp\tau_3 G^R\sigma^\alpha\tau_1 G^R\tau_1 G^A\right]+\mathrm{c.c.}\\ &= \boldsymbol{A}_i\times\hat{z}\sum_{\boldsymbol{k}}2\delta(\mu^2-E_{\boldsymbol{k}}^2)\frac{\tau}{|\mu|}\Bigg\{-(\partial_i\varepsilon_{\boldsymbol{k}})^2\gamma_3\\ &\quad+(\mu\gamma_3+M\gamma_0)\left[2(\partial_i\varepsilon_{\boldsymbol{k}})^2\gamma_0\frac{\tau}{\mu}-\mu\frac{\varepsilon_{\boldsymbol{k}}(\partial_i^2\varepsilon_{\boldsymbol{k}})-(\partial_i\varepsilon_{\boldsymbol{k}})^2}{\mu^2-M^2}\right]\Bigg\}.\end{aligned} \tag{3.68}$$

The anomalous velocity term (the third diagram) without vertex correction is calculated as

$$\begin{aligned}(\mathrm{d3})^{\mathrm{surf}} &= \frac{1}{i\omega}\frac{-\omega}{2\pi i}\frac{1}{2}A_i^\alpha\sum_{\boldsymbol{k}}(\partial_i^2\varepsilon_{\boldsymbol{k}})\mathrm{tr}(\sigma^\perp\tau_3 G^R\sigma^\alpha\tau_1 G^A)\\ &= \boldsymbol{A}_i\times\hat{z}\sum_{\boldsymbol{k}}(\partial_i^2\varepsilon_{\boldsymbol{k}})\varepsilon_{\boldsymbol{k}}2\gamma_3\frac{\tau}{|\mu|}\delta(\mu^2-E_{\boldsymbol{k}}^2).\end{aligned} \tag{3.69}$$

The Fermi-sea terms in (d1)+(d2) are given by

$$\begin{aligned}[(\mathrm{d1})+(\mathrm{d2})]^{\mathrm{sea}} &= \frac{1}{i\omega}\frac{1}{2\pi i}\frac{1}{2}A_i^\alpha\sum_{\boldsymbol{k}}(\partial_i\varepsilon_{\boldsymbol{k}})^2\\ &\quad\times\int d\varepsilon\Big\{f(\varepsilon_-)\,\mathrm{tr}\left[\,\sigma^\perp\tau_3 G_+^R\left(\tau_1 G_-^R\sigma^\alpha\tau_1+\sigma^\alpha\tau_1 G_+^R\tau_1\right)G_-^R\right]\\ &\qquad-f(\varepsilon_+)\,\mathrm{tr}\left[\,\sigma^\perp\tau_3 G_+^A\left(\tau_1 G_-^A\sigma^\alpha\tau_1+\sigma^\alpha\tau_1 G_+^A\tau_1\right)G_-^A\right]\Big\}\\ &= \boldsymbol{A}_i\times\hat{z}\,\frac{M\,(\mathrm{sgn}\mu)}{\mu^2-M^2}\sum_{\boldsymbol{k}}\left\{\varepsilon_{\boldsymbol{k}}(\partial_i^2\varepsilon_{\boldsymbol{k}})-(\partial_i\varepsilon_{\boldsymbol{k}})^2\right\}\delta(\mu^2-E_{\boldsymbol{k}}^2),\end{aligned} \tag{3.70}$$

where $f(\varepsilon)=\theta(-\varepsilon)$ is the Fermi-Dirac distribution function at zero temperature, $\varepsilon_\pm=\varepsilon\pm\omega/2$, and $G_\pm^{R/A}=G^{R/A}(\varepsilon\pm\omega/2)$.

The Fermi-sea term from the anomalous velocity diagram vanishes,

$$\begin{aligned}(\mathrm{d3})^{\mathrm{sea}} &= \frac{1}{2\pi i}\frac{1}{2}A_i^\alpha \sum_{\boldsymbol{k}}(\partial_i^2\varepsilon_{\boldsymbol{k}})\int d\varepsilon\Big\{ f(\varepsilon_-)\,\mathrm{tr}\left[\,\sigma^\perp\tau_3 G_+^R\sigma^\alpha\tau_1 G_-^R\right] \\ &\qquad\qquad - f(\varepsilon_+)\,\mathrm{tr}\left[\,\sigma^\perp\tau_3 G_+^A\sigma^\alpha\tau_1 G_-^A\right]\Big\} \\ &= 0. \end{aligned} \tag{3.71}$$

Adding up the Fermi-surface and Fermi-sea terms, we obtain

$$[(\mathrm{d1})+(\mathrm{d2})+(\mathrm{d3})]^{\mathrm{surf\ \&\ sea}} = \boldsymbol{A}_i\times\hat{z}\,\frac{2\nu}{\mu}\langle\!\langle(\partial_i\varepsilon_{\boldsymbol{k}})^2\rangle\!\rangle\frac{2\tau^2\gamma_0}{\mu^2}(\mu\gamma_3+M\gamma_0). \tag{3.72}$$

Next, the diagrams with vertex corrections, shown in Fig. 4.1 (e), give

$$\begin{aligned}&(\mathrm{e1})+(\mathrm{e2})+(\mathrm{e3}) = \\ &\frac{1}{i\omega}\frac{-\omega}{2\pi i}\frac{1}{4^2}\frac{1}{2}A_i^\alpha\left(\sum_{\boldsymbol{k}}\mathrm{tr}(\sigma^\perp\tau_3 G^R\sigma^\lambda G^A)\right)\frac{2\gamma}{\pi\nu}\cdot\frac{\gamma_{\mathrm{n}}-\gamma_z}{\frac{M^2}{\mu^2}\gamma_{\mathrm{n}}+\gamma_z+(1-\frac{M^2}{\mu^2})\gamma_\perp} \\ &\times\left\{\sum_{\boldsymbol{k}}(\partial_i\varepsilon_{\boldsymbol{k}})^2\,\mathrm{tr}\left[\sigma^\lambda G^R\sigma^\alpha G^R\tau_1 G^A\right]+\mathrm{c.c.}+(\partial_i^2\varepsilon_{\boldsymbol{k}})\,\mathrm{tr}\left[\sigma^\lambda G^R\sigma^\alpha\tau_1 G^A\right]\right\}.\end{aligned} \tag{3.73}$$

The first trace is evaluated as

$$\sum_{\boldsymbol{k}}\mathrm{tr}\left[\sigma^\perp\tau_3 G^R\sigma^\lambda G^A\right] = -i\,\mathrm{tr}(\sigma^\perp\sigma^\lambda\sigma^z)(\gamma_3\mu+\gamma_0 M)\frac{2\pi\tau\nu}{\mu^2}. \tag{3.74}$$

The second trace is the same as calculation of the uniform spin density. Thus, we have

$$\begin{aligned}&(\mathrm{e1})+(\mathrm{e2})+(\mathrm{e3}) = \\ &\boldsymbol{A}_i\times\hat{z}\,\frac{2\nu}{\mu}\langle\!\langle(\partial_i\varepsilon_{\boldsymbol{k}})^2\rangle\!\rangle\frac{\gamma_{\mathrm{n}}-\gamma_z}{\frac{M^2}{\mu^2}\gamma_{\mathrm{n}}+\gamma_z+(1-\frac{M^2}{\mu^2})\gamma_\perp}\left(\frac{-M(\mu\gamma_3+M\gamma_0)^2}{4\mu^4\gamma^2}\right).\end{aligned} \tag{3.75}$$

Therefore, the total staggered spin density in the rotated frame is obtained as

$$\begin{aligned}\langle\tilde{\boldsymbol{\sigma}}^{\perp}\tau_3\rangle_{\rm ne} =\ & [(\mathrm{d1})+(\mathrm{d2})+(\mathrm{d3})]^{\text{surf \& sea}}+(\mathrm{e1})+(\mathrm{e2})+(\mathrm{e3})\\ &= \boldsymbol{A}_i\times\hat{z}\,\frac{2\nu\tau}{\mu}\langle\!\langle(\partial_i\varepsilon_{\boldsymbol{k}})^2\rangle\!\rangle(\gamma_\perp+\gamma_z)\frac{2M(\gamma_{\rm n}+\gamma_z)}{M^2\gamma_{\rm n}+\mu^2\gamma_z+(\mu^2-M^2)\gamma_\perp}(-eE_i)\\ &= \boldsymbol{A}_i\times\hat{z}\,\frac{2\nu\tau}{\mu}\langle\!\langle(\partial_i\varepsilon_{\boldsymbol{k}})^2\rangle\!\rangle\frac{2(\gamma_\perp+\gamma_z)}{M}(-eE_i)\\ &= -\boldsymbol{A}_i\times\hat{z}\,\frac{2(\gamma_\perp+\gamma_z)}{M}\frac{2\mu}{\mu^2-M^2}\,\frac{j_i}{2e},\end{aligned}\tag{3.76}$$

where in the third equality, we retained lowest-order terms in spin relaxation (magnetic impurities). In the laboratory frame, we have

$$\langle\boldsymbol{\sigma}^{\perp}\tau_3\rangle_{\rm ne}=\mathcal{R}\langle\tilde{\boldsymbol{\sigma}}^{\perp}\tau_3\rangle_{\rm ne}=\beta_n\,\partial_i\boldsymbol{n}\,\frac{2\mu}{\mu^2-M^2}\,\frac{j_i}{2e},\tag{3.77}$$

where $\beta_n=2(\gamma_\perp+\gamma_z)/M$.

3.B.4 Damping torques for staggered moment

To calculate the damping term due to conduction electrons, we use the small amplitude method and consider

$$\mathcal{H}_{\rm sd}^{\delta n}=-M\sum_{\boldsymbol{k}}\psi_{\boldsymbol{k}}^{\dagger}\boldsymbol{\sigma}\tau_3\psi_{\boldsymbol{k}}\cdot\delta\boldsymbol{n}\tag{3.78}$$

to be the perturbing Hamiltonian, with the dynamic deviation of the Néel vector $\delta\boldsymbol{n}$ in the xy plane [44]. We calculate the ω-linear terms of the staggered spin density in response to $\mathcal{H}_{\rm sd}^{\delta n}$ using the Kubo formula

$$\langle\boldsymbol{\sigma}\tau_3(\omega)\rangle_{\rm ne}^{\delta n}=-\frac{i}{\hbar}\int_{-\infty}^{\infty}e^{i\omega t}\theta(t)\langle[\hat{\boldsymbol{\sigma}}_n(t),\mathcal{H}_{\rm sd}^{\delta n}(0)]\rangle\,dt.\tag{3.79}$$

The terms without vertex correction is given by

$$\begin{aligned}\langle\boldsymbol{\sigma}\tau_3\rangle^{\delta n}=-M\delta n^{\alpha}\frac{1}{2\pi i}\int d\varepsilon\Big[&\left(-f(\varepsilon_+)+f(\varepsilon_-)\right)\boldsymbol{\sigma}\tau_3G^R(\varepsilon_+)\sigma^{\alpha}\tau_3G^A(\varepsilon_-)\\ &+f(\varepsilon_+)\boldsymbol{\sigma}\tau_3G^A(\varepsilon_+)\sigma^{\alpha}\tau_3G^A(\varepsilon_-)-f(\varepsilon_-)\boldsymbol{\sigma}\tau_3G^R(\varepsilon_+)\sigma^{\alpha}\tau_3G^R(\varepsilon_-)\Big].\end{aligned}\tag{3.80}$$

The RA term gives

$$\langle \boldsymbol{\sigma}\tau_3\rangle^{\delta n}_{RA} = -M\delta\boldsymbol{n}\frac{\omega}{2\pi i}4(\mu^R\mu^A - T^RT^A - J^RJ^A) \tag{3.81}$$

$$= 2i\omega M\delta\boldsymbol{n}\frac{2\nu\tau}{\mu^2}(\gamma_0^2 - \gamma_3^2) \tag{3.82}$$

The RR and AA terms give

$$\langle \boldsymbol{\sigma}\tau_3\rangle^{\delta n}_{RR} + \langle \boldsymbol{\sigma}\tau_3\rangle^{\delta n}_{AA} = \frac{1}{2}M\delta n^\alpha\frac{\omega}{2\pi i}\left(\boldsymbol{\sigma}\tau_3G^R\sigma^\alpha\tau_3G^R + \boldsymbol{\sigma}\tau_3G^A\sigma^\alpha\tau_3G^A\right) \tag{3.83}$$

$$= 0 \tag{3.84}$$

With vertex correction the RA term is given by,

$$\langle \boldsymbol{\sigma}\tau_3\rangle^{\delta n}_{RA,V} = -\frac{1}{4^2}M\delta n^\alpha\frac{\omega}{2\pi i}\mathrm{tr}(\boldsymbol{\sigma}\tau_3G^R\sigma^\beta G^A)\,\Pi\,\mathrm{tr}(\sigma^\beta G^R\sigma^\alpha\tau_3G^A) \tag{3.85}$$

$$= -i\omega M\delta\boldsymbol{n}(\gamma_3\mu + \gamma_0 M)^2\frac{2\nu\tau}{\mu^2}\frac{\gamma_\mathrm{n} - \gamma_z}{M^2\gamma_\mathrm{n} + \mu^2\gamma_z + (\mu^2 - M^2)\gamma_\perp} \tag{3.86}$$

Lastly, let us consider the vertex correction on the RR and AA terms.

$$\langle \boldsymbol{\sigma}\tau_3\rangle^{\delta n}_{RR,V} + \langle \boldsymbol{\sigma}\tau_3\rangle^{\delta n}_{AA,V}$$

$$= \frac{1}{2\cdot 4^2}M\delta n^\alpha\frac{\omega}{2\pi i}\left(\mathrm{tr}[\boldsymbol{\sigma}\tau_3G^A\sigma^\beta\tau_3G^A]\,\Pi_1\,\mathrm{tr}[\sigma^\beta\tau_3G^A\sigma^\alpha\tau_3G^A] + \mathrm{c.c.}\right) \tag{3.87}$$

$$= M\delta\boldsymbol{n}i\omega(\gamma_\mathrm{n} - \gamma_z)\frac{2\nu}{\mu^2} \tag{3.88}$$

where Π_1 is the vertex correction with one non-magnetic and magnetic impurity, $\Pi_1 = \frac{4}{\pi\nu}(\gamma_\mathrm{n} - \gamma_z)$. Finally, adding up the terms obtained

$$\langle \boldsymbol{\sigma}\tau_3\rangle^{\delta n}_{\mathrm{ne}} = \langle \boldsymbol{\sigma}\tau_3\rangle^{\delta n}_{RA} + \langle \boldsymbol{\sigma}\tau_3\rangle^{\delta n}_{RR} + \langle \boldsymbol{\sigma}\tau_3\rangle^{\delta n}_{AA} + \langle \boldsymbol{\sigma}\tau_3\rangle^{\delta n}_{RA,V} + \langle \boldsymbol{\sigma}\tau_3\rangle^{\delta n}_{RR,V} + \langle \boldsymbol{\sigma}\tau_3\rangle^{\delta n}_{AA,V} \tag{3.89}$$

$$= -2\,\delta\dot{\boldsymbol{n}}\frac{2\nu}{M}\left[\gamma_z + \gamma_\perp + \frac{M^2}{\mu^2}(\gamma_\perp - \gamma_z)\right] \tag{3.90}$$

to the leading order in magnetic impurities. This gives the damping parameter

$$\alpha_n = \left[\gamma_z + \gamma_\perp + \frac{M^2}{\mu^2}(\gamma_\perp - \gamma_z)\right]\frac{2\nu}{s_n} \tag{3.91}$$

where $s_n = 2\hbar S/(2a^2)$.

3.B.5 Damping torques for uniform moment

The uniform damping torque parameter α_ℓ is similarly calculated using the small amplitude method as the ω-linear terms of the uniform spin density in response to the s-d coupling to $\tilde{\boldsymbol{l}}$. The result is given by

$$\langle \boldsymbol{\sigma} \rangle_{\rm na} = 2Mi\omega\tilde{\boldsymbol{l}}(\mu^2 - M^2)\frac{2(\tau + \tau_\phi^0)\nu}{\mu^2} \tag{3.92}$$

$$= i\omega\tilde{\boldsymbol{l}}\frac{(\mu^2 + M^2)(\mu^2 - M^2)}{M}\frac{2\nu\tau}{\mu^2}, \tag{3.93}$$

so

$$\alpha_\ell = \frac{(\mu^2 + M^2)(\mu^2 - M^2)}{\mu^2}\frac{\nu\tau}{s_n}. \tag{3.94}$$

3.C Appendix: Domain wall motion in ferrimagnet

To discuss the experiment reported in Ref. [16], we study here the dynamics of a domain wall (DW) in a *ferrimagnet*. We use the collective coordinates which are essentially the same as those for antiferromagnetic (AF) DW defined in the text, by noting that the Néel vector is associated with a (longitudinal) ferromagnetic (FM) component. Near the angular-momentum compensation point, the dynamics is dominated by the AF component with a slight mixture of the FM component. Denoting the fraction of the latter by δ, which is a small dimensionless parameter ($|\delta| \ll 1$) and vanishes at the angular-momentum compensation point, the equations of motion under a steady current are given by [16]

$$\frac{1}{v_J}\ddot{X} \pm \delta\dot{\phi}_0 + \tilde{\alpha}\frac{\dot{X}}{\lambda} = \frac{\beta_n v_n + \beta v_{\rm s}}{\lambda}, \tag{3.95}$$

$$\frac{1}{v_J}\lambda^2\ddot{\phi}_0 \mp \delta\dot{X} + \tilde{\alpha}\lambda\dot{\phi}_0 = \mp v_{\rm s} - v_K \sin 2\phi_0. \tag{3.96}$$

Here, $\tilde{\alpha} \simeq \alpha_n$ is the effective damping parameter. Other notations are the same as in Eqs. (33)-(36), (38) and (39) in the text. Note that these equations reduce to those in AF at $\delta = 0$, except for the terms with $v_{\rm s}$ (including $\beta v_{\rm s}$), which do not necessarily vanish at $\delta = 0$ [16]. (Similarly, the difference $\tilde{\alpha} - \alpha_n$

is finite in general, but this would be small compared to α_n, or, at most, of the same order as α_n.) Following Ref. [16], we obtain the terminal velocity as

$$\langle \dot{X} \rangle = -\frac{\tilde{\alpha}\beta_n v_n + (\tilde{\alpha}\beta + \delta) v_{\rm s}}{\delta^2 + \tilde{\alpha}^2}, \tag{3.97}$$

which is decomposed into the even part (with respect to δ),

$$\langle \dot{X} \rangle_{\rm even} = -\frac{\tilde{\alpha}(\beta_n v_n + \beta v_{\rm s})}{\delta^2 + \tilde{\alpha}^2} \simeq -\frac{\beta_n v_n + \beta v_{\rm s}}{\alpha_n}, \tag{3.98}$$

which comes from the β torques, and the odd part (not shown) coming from the spin-transfer torque. In the last expression, we set $\delta = 0$ and approximated $\tilde{\alpha}$ by α_n. Of the two terms in Eq. (3.98), the analysis in Ref. [16] was done only with the second one ($\sim \beta v_{\rm s}$), whereas we found in the present work that the first term ($\sim \beta_n v_n$) also exists. In the text, a discussion is given that considering the latter ($\sim \beta_n v_n$) allows a reasonable interpretation of the experimental results.

Chapter 4

Current-induced spin-wave Doppler shift

In this chapter, we theoretically study the influence of an electric current on antiferromagnetic spin waves. One of the effects electric current has on spin waves is spin-transfer torque induced Doppler shift in spin wave dispersion. It has been believed that there is only one spin-transfer torque in antiferromagnets, similar to ferromagnets, hence only one source of spin-wave Doppler shift. In this chapter, we identify two different sources of spin-transfer torques that stem from uniform ($\boldsymbol{v}_n$) and staggered ($\boldsymbol{v}_\ell$) electron spin densities. While the former is well recognized, the latter is often overlooked. We show that both $\boldsymbol{v}_n$ and $\boldsymbol{v}_\ell$ contribute equally to the spin-wave Doppler shift. Microscopic calculations are presented for electrons on a two-dimensional square lattice with nearest-neighbor (t) and next-nearest-neighbor (t') hopping, which interpolate two opposite transport regimes of strongly-coupled AF ($t'/t \ll 1$) and two decoupled ferromagnets ($t'/t \gg 1$). In the AF transport regime ($t'/t \ll 1$), $\boldsymbol{v}_n$ and $\boldsymbol{v}_\ell$ have opposite signs, and the sign of the Doppler shift depends on band filling. As t'/t is increased, $\boldsymbol{v}_n$ undergoes a sign change whereas $\boldsymbol{v}_\ell$ does not. In the limit of vanishing t, $\boldsymbol{v}_n$ and $\boldsymbol{v}_\ell$ coincide and the spin-transfer torque reduces to that of ferromagnets.

4.1 Introduction

In the previous two chapters, we looked at the dynamics of antiferromagnetic domain walls. In this chapter, we focus on spin waves, which is another fundamental dynamics in magnetic materials. Spin waves are small perturbations of spins from their equilibrium positions that collectively propagate as a wave, They carry heat and angular momentum, and are expected to play an important role in spintronics. Unlike electric currents that can also carry heat and angular momentum, spin waves do not suffer Joule heating and can be more energy efficient.

Much of the work done so far on spin waves are focused on ferromagnets (FMs) and the understanding of antiferromagnetic (AF) spin waves remain relatively poor. As it was previously noted, AFs have the advantage of fast spin dynamics compared to FMs [1], so AF spin wave-based devices can operate at frequencies higher by orders of magnitude. AF spin waves come with another big perk that might revolutionize magnonics, which is the chirality or isospin degree of freedom [56]. In contrast to FM spin waves that can only encode information in its amplitude, AF spin waves have multiple modes with different chiralities. Specifically, collinear AFs possess two degenerate eigenmodes with opposite chiralities. Despite the highly anticipated features of AF spin waves, the means to control them remain limited.

From a scalability perspective, electrical manipulation of spin waves is ideal. In FMs, the effects of electric current on spin waves are relatively well known [57, 58, 59, 60, 61]. In particular, the adiabatic spin-transfer torque (STT) causes a Doppler shift on spin waves, which can be used as a probe of spin-polarized transport in magnetic materials [58], to realize effective black holes [62], and so on. Spin-wave Doppler shifts also realize in AFs [35]. Pioneering theories have elucidated key properties of AF spin torques phenomenologically [34, 35, 24, 27, 36, 37], and microscopic theories have identified their origins [29]. Experiments on AF spintronics remain limited as the lack of leakage magnetic field hinders detection of magnetic information, while the immunity to external fields forbids easy manipulation of the AF spins. Compensated ferrimagnets have been used to overcome these

[1] AF have spin waves that can reach frequencies in the terahertz range while FM spin waves remain in the gigahertz range. This difference stems from the gap in the spin wave dispersion; while the gap for FM spin waves is given by the magnetic anisotropy K, it is given by the square root of the product of magnetic anisotropy and exchange coupling, $\sqrt{JK}$, in AF.

difficulties, in which AF spin dynamics is realized at the angular momentum compensation temperature while a finite macroscopic magnetic moment allows detection and manipulation of the magnetic texture [16, 63].

In this chapter, we microscopically explore the effect of electric current on AF spin dynamics, and study the spin-wave properties in particular. We first derive the equations of motion for AF spins with two kinds of adiabatic STT. The coefficients of the STTs are then calculated based on a microscopic electron model. With nearest-neighbor (n.n.) and next-nearest-neighbor (n.n.n.) electron hopping considered, the model incorporates two typical transport regimes, namely, strongly-coupled AF and two decoupled FMs. By interpolating these two limiting cases, we identify several characteristic features of the STT in AF compared to FM. In particular, we point out that the STT responsible for the spin-wave Doppler shift in AF is different from the STT that acts on AF domain walls [24, 27, 29]. This distinction is a new feature of AF STT, not present in FM.

4.2 Antiferromagnetic spin dynamics and Doppler shift

We consider a metallic AF consisting of localized spins and conduction electrons, interacting mutually via the s-d exchange interaction. The Hamiltonian is

$$H = H_S + H_{\rm el} + H_{\rm sd}. \tag{4.1}$$

The localized spins and their coupling to the electrons are described, respectively, by

$$H_S = J \sum_{\langle i,j \rangle} \boldsymbol{S}_i \cdot \boldsymbol{S}_j - K \sum_i (S_i^z)^2, \tag{4.2}$$

$$H_{\rm sd} = -J_{\rm sd} \sum_i \boldsymbol{S}_i \cdot c_i^\dagger \boldsymbol{\sigma} c_i, \tag{4.3}$$

where $\boldsymbol{S}_i$ is a classical spin at site i, $J > 0$ is the AF exchange coupling constant between the n.n. sites, and $K > 0$ is the easy-axis anisotropy constant. In $H_{\rm sd}$, $c_i^\dagger = (c_{i\uparrow}^\dagger, c_{i\downarrow}^\dagger)$ are electron creation operators at site i, $\boldsymbol{\sigma}$ is a vector of Pauli matrices, and $J_{\rm sd}$ is the s-d exchange coupling constant. The Hamiltonian $H_{\rm el}$ for the electrons will be specified later.

We first describe the AF spin dynamics by considering a general Bravais (primitive) lattice in d spatial dimensions. We adopt the exchange approximation, in which J is considered the largest energy scale in the spin system[42, 18]. Then the description is simplified by introducing the Néel vector and uniform moment[41],

$$\boldsymbol{n}_m = \frac{\boldsymbol{S}_{A,m} - \boldsymbol{S}_{B,m}}{2S}, \quad \boldsymbol{l}_m = \frac{\boldsymbol{S}_{A,m} + \boldsymbol{S}_{B,m}}{2S}, \tag{4.4}$$

respectively. The localized spins at A and B sites in unit cell m are denoted by $\boldsymbol{S}_{A,m}$ and $\boldsymbol{S}_{B,m}$, and S is their constant magnitude. We also adopt the continuum approximation, $\boldsymbol{n}_m \to \boldsymbol{n}(\boldsymbol{r})$ and $\boldsymbol{l}_m \to \boldsymbol{l}(\boldsymbol{r})$, assuming that their spatial variations are slow. Further simplifications can be made by introducing the physical magnetization [43]

$$\tilde{\boldsymbol{l}} \equiv \boldsymbol{l} + \frac{a}{2}\partial_x \boldsymbol{n}, \tag{4.5}$$

where a is the lattice constant and ∂_x is a spatial derivative in the direction from A to B site in the unit cell.

The Lagrangian density for localized spins is then given by

$$\mathcal{L}_S = s_n\big\{\tilde{\boldsymbol{l}} \cdot (\boldsymbol{n} \times \dot{\boldsymbol{n}}) - \mathcal{H}_S - \mathcal{H}_{\rm sd}\big\}, \tag{4.6}$$

$$\mathcal{H}_S = \frac{1}{2}\left\{ \tilde{J}\,\tilde{\boldsymbol{l}}^2 + \frac{c^2}{\tilde{J}} \sum_{i=1}^{d} (\partial_i \boldsymbol{n})^2 - \tilde{K}\,(n^z)^2 \right\}, \tag{4.7}$$

$$\mathcal{H}_{\rm sd} = -\frac{M}{s_n}(\tilde{\boldsymbol{l}} \cdot \hat{\boldsymbol{\sigma}}_\ell + \boldsymbol{n} \cdot \hat{\boldsymbol{\sigma}}_n), \tag{4.8}$$

where $\hat{\boldsymbol{\sigma}}_n$ and $\hat{\boldsymbol{\sigma}}_\ell$ are the staggered and uniform spin densities of the conduction electrons. We defined $\tilde{J} = 2zJS/\hbar$, $c = (zJSa)/(\hbar\sqrt{d})$, $\tilde{K} = 2SK/\hbar$, $s_n = 2\hbar S/(2a^d)$ and $M = J_{\rm sd}S$, where z is the coordination number (number of n.n. sites). This leads to the equations of motion,

$$\dot{\boldsymbol{n}} = \boldsymbol{H}_\ell \times \boldsymbol{n} + \boldsymbol{t}_n, \tag{4.9}$$

$$\dot{\tilde{\boldsymbol{l}}} = \boldsymbol{H}_n \times \boldsymbol{n} + \boldsymbol{H}_\ell \times \tilde{\boldsymbol{l}} + \boldsymbol{t}_\ell, \tag{4.10}$$

where $\boldsymbol{H}_n = \partial\mathcal{H}_S/\partial\boldsymbol{n}$ and $\boldsymbol{H}_\ell = \partial\mathcal{H}_S/\partial\tilde{\boldsymbol{l}}$ are the effecive fields determined by the spin Hamiltonian, and

$$\boldsymbol{t}_n = \frac{M}{s_n}\boldsymbol{n} \times \langle\hat{\boldsymbol{\sigma}}_\ell\rangle, \tag{4.11}$$

$$\boldsymbol{t}_\ell = \frac{M}{s_n}\big\{\, \boldsymbol{n} \times \langle\hat{\boldsymbol{\sigma}}_n\rangle + \tilde{\boldsymbol{l}} \times \langle\hat{\boldsymbol{\sigma}}_\ell\rangle \,\big\}, \tag{4.12}$$

are the torques due to the conduction electrons. Note that Eqs. (4.9) and (4.10) are consistent with the constraints, $\tilde{\boldsymbol{l}} \cdot \boldsymbol{n} = 0$ and $|\boldsymbol{n}| = 1$.

Under a current flow or time-dependent $\boldsymbol{n}$ and $\tilde{\boldsymbol{l}}$, the spin densities $\langle \hat{\boldsymbol{\sigma}}_n \rangle$ and $\langle \hat{\boldsymbol{\sigma}}_\ell \rangle$ are expected to acquire nonequilibrium components as

$$\langle \hat{\boldsymbol{\sigma}}_n \rangle = \frac{s_n}{M} \big\{ -\beta_n (\boldsymbol{v}_n \cdot \nabla)\, \boldsymbol{n} + \boldsymbol{n} \times (\boldsymbol{v}_\ell \cdot \nabla)\, \tilde{\boldsymbol{l}} - \alpha_n \dot{\boldsymbol{n}} \big\}, \tag{4.13}$$

$$\langle \hat{\boldsymbol{\sigma}}_\ell \rangle = \frac{s_n}{M} \big\{ \boldsymbol{n} \times (\boldsymbol{v}_n \cdot \nabla)\, \boldsymbol{n} - \alpha_\ell \dot{\tilde{\boldsymbol{l}}} \big\}, \tag{4.14}$$

where $\boldsymbol{v}_n$ and $\boldsymbol{v}_\ell$ are coefficients for the current-induced torques, β_n characterizes the so-called β-torque, and α_n and α_ℓ are damping coefficients. The microscopic expressions of $\boldsymbol{v}_n$, β_n, α_n and α_ℓ have been derived in Ref. [29], while $\boldsymbol{v}_\ell$ is often overlooked (see, however, Refs. [24, 38]). Note that the above spin densities respect the sublattice symmetry $\boldsymbol{n} \to -\boldsymbol{n}$, $\tilde{\boldsymbol{l}} \to \tilde{\boldsymbol{l}}$ in Eqs. (4.9) and (4.10).

The equations of motion can then be written explicitly as

$$\dot{\boldsymbol{n}} = \tilde{J}\, \tilde{\boldsymbol{l}} \times \boldsymbol{n} - (\boldsymbol{v}_n \cdot \nabla)\boldsymbol{n} \tag{4.15}$$

$$\begin{aligned} \dot{\tilde{\boldsymbol{l}}} = & -\big(\tilde{J}^{-1} c^2 \nabla^2 \boldsymbol{n} + \tilde{K} n^z \hat{z}\big) \times \boldsymbol{n} \\ & + \big\{ \beta_n (\boldsymbol{v}_n \cdot \nabla)\boldsymbol{n} + \alpha_n \dot{\boldsymbol{n}} \big\} \times \boldsymbol{n} \\ & - (\boldsymbol{v}_\ell \cdot \nabla)\, \tilde{\boldsymbol{l}} + \boldsymbol{n} [\tilde{\boldsymbol{l}} \cdot (\boldsymbol{v}_n \cdot \nabla)\boldsymbol{n} + \boldsymbol{n} \cdot (\boldsymbol{v}_\ell \cdot \nabla)\tilde{\boldsymbol{l}}]. \end{aligned} \tag{4.16}$$

The terms with α_ℓ are dropped in the exchange approximation. One may eliminate $\tilde{\boldsymbol{l}}$ from these equations to obtain

$$\begin{aligned} \boldsymbol{n} \times \ddot{\boldsymbol{n}} = & \boldsymbol{n} \times \big(c^2 \nabla^2 \boldsymbol{n} + \tilde{J}\tilde{K} n^z \hat{z}\big) \\ & - \tilde{J} \boldsymbol{n} \times \big[\beta_n (\boldsymbol{v}_n \cdot \nabla)\boldsymbol{n} + \alpha_n \dot{\boldsymbol{n}}\big] \\ & - \boldsymbol{n} \times [(\boldsymbol{v}_n + \boldsymbol{v}_\ell) \cdot \nabla] \dot{\boldsymbol{n}} \\ & - \boldsymbol{n} \times (\boldsymbol{v}_\ell \cdot \nabla)(\boldsymbol{v}_n \cdot \nabla)\boldsymbol{n}. \end{aligned} \tag{4.17}$$

Linearizing this equation around a uniform state $\boldsymbol{n} = \hat{z}$ by considering a small transverse component $\delta\boldsymbol{n}$ such that $\boldsymbol{n}(\boldsymbol{r}) = \hat{z} + \delta\boldsymbol{n}\, e^{i\boldsymbol{q}\cdot\boldsymbol{r} - i\omega t}$, one obtains a dispersion relation,

$$\begin{aligned} \omega^2 = & c^2 q^2 + \tilde{J}\tilde{K} + i\tilde{J} \big\{ \beta_n (\boldsymbol{v}_n \cdot \boldsymbol{q}) - \omega \alpha_n \big\} \\ & + [(\boldsymbol{v}_n + \boldsymbol{v}_\ell) \cdot \boldsymbol{q}]\, \omega - (\boldsymbol{v}_\ell \cdot \boldsymbol{q})(\boldsymbol{v}_n \cdot \boldsymbol{q}). \end{aligned} \tag{4.18}$$

Solving for ω to the leading order in $\boldsymbol{v}_n$ and $\boldsymbol{v}_\ell$ leads to

$$\omega = \Bigg(c^2q^2 + \tilde{J}\tilde{K} + \tilde{J}\beta_n(\boldsymbol{v}_n \cdot i\boldsymbol{q}) - (\boldsymbol{v}_\ell \cdot \boldsymbol{q})(\boldsymbol{v}_n \cdot \boldsymbol{q}) + \frac{[i\alpha_n\tilde{J} - (\boldsymbol{v}_n + \boldsymbol{v}_\ell)\cdot \boldsymbol{q}]^2}{4} \Bigg)^{1/2} \mp \frac{i\alpha_n\tilde{J} - (\boldsymbol{v}_n + \boldsymbol{v}_\ell)\cdot \boldsymbol{q}}{2} \tag{4.19}$$

$$\simeq \sqrt{c^2q^2 + \tilde{J}\tilde{K}} \pm \frac{(\boldsymbol{v}_n + \boldsymbol{v}_\ell)\cdot \boldsymbol{q}}{2}. \tag{4.20}$$

In the last expression, we dropped the effects of damping and dissipative β-torques. We see that the Doppler shift of AF spin waves is given by $(\boldsymbol{v}_n + \boldsymbol{v}_\ell)/2$; this is one of the main results of this chapter. A similar result was obtained in Ref. [35] but without account for $\boldsymbol{v}_\ell$.

4.3 Current-induced torques

To determine the magnitude of $\boldsymbol{v}_n$ and $\boldsymbol{v}_\ell$, we next perform a microscopic calculation. To be explicit, we consider electrons on a two-dimensional square lattice,

$$H_{\rm el} = -t\sum_{\langle i,j\rangle}(c_i^\dagger c_j + \text{H.c.}) - t'\sum_{\langle\langle l,m\rangle\rangle}(c_l^\dagger c_m + \text{H.c.}) + V_{\rm imp}, \tag{4.21}$$

with n.n. hopping (first term), n.n.n. hopping (second term), and subject to impurity potentials (last term). To calculate $\boldsymbol{v}_n$ and $\boldsymbol{v}_\ell$, it is sufficient to consider nonmagnetic impurities,

$$V_{\rm imp} = u_{\rm i}\sum_{j\in C} c_j^\dagger c_j, \tag{4.22}$$

where $u_{\rm i}$ is the strength of the impurity potential and C is a set of impurity positions. The number of impurities is assumed equal for the two sublattices, with density $n_{\rm i}$. Combining $H_{\rm el}$ with $H_{\rm sd}$ completes the model for the conduction electrons.

To treat the spatial variation of the Néel vector, we employ the method of spin gauge field [17]. For this, it is convenient to assume that $\boldsymbol{n}$ and $\tilde{\boldsymbol{l}}$ are

defined at each site i, and write[28]

$$\boldsymbol{S}_i = S\left\{\tilde{\boldsymbol{l}}_i + (-)^i \boldsymbol{n}_i\right\}. \tag{4.23}$$

This will be justified, and is consistent with Eqs. (4.4) and (4.5) [43], if $\tilde{\boldsymbol{l}}_i$ and $\boldsymbol{n}_i$ are smooth enough and do not contain large-wavevector components. We then perform a local SU(2) rotation U_i that brings the Néel vector at each site i to the z direction, $U_i^\dagger(\boldsymbol{n}_i\cdot\boldsymbol{\sigma})U_i = \sigma^z$. The hopping term is then modified through $U_i^\dagger U_j = e^{iA_{ij}}$, which introduces the spin gauge field A_{ij}. We also define the corresponding 3×3 rotation matrix $\mathcal{R}_i$ by $U_i^\dagger \boldsymbol{\sigma} U_i = \mathcal{R}_i\boldsymbol{\sigma}$.

The Hamiltonian then becomes $H_{\rm el}+H_{\rm sd} = H_0 + H' + V_{\rm imp}$,

$$H_0 = \sum_{i,j} t_{ij}\tilde{c}_i^\dagger \tilde{c}_j - M\sum_i (-)^i \tilde{c}_i^\dagger \sigma^z \tilde{c}_i, \tag{4.24}$$

$$H' = \sum_{i,j} t_{ij}\tilde{c}_i^\dagger iA_{ij}\tilde{c}_j - M\sum_i (\mathcal{R}_i^{-1}\tilde{\boldsymbol{l}}_i)\cdot \tilde{c}_i^\dagger \boldsymbol{\sigma}\tilde{c}_i, \tag{4.25}$$

up to $O(A_{ij}^2)$, where $\tilde{c}_i = U_i^\dagger c_i$ is defined in the rotated frame, and t_{ij} is $-t$ ($-t'$) if i,j are n.n. (n.n.n.) pairs and zero otherwise. Since A_{ij} and $\tilde{\boldsymbol{l}}$ are considered small, we treat H' perturbatively [23].

The unperturbed part H_0 describes electrons interacting with a uniform AF moment with dispersion

$$E_{\boldsymbol{k},\pm} = \pm E_{\boldsymbol{k}} + \varepsilon'_{\boldsymbol{k}}, \tag{4.26}$$

where $E_{\boldsymbol{k}} = \sqrt{\varepsilon_{\boldsymbol{k}}^2 + M^2}$, $\varepsilon_{\boldsymbol{k}} = -2t(\cos k_x + \cos k_y)$ comes from the n.n. hopping, and $\varepsilon'_{\boldsymbol{k}} = -4t'\cos k_x \cos k_y$ from the n.n.n. hopping. At $t'=0$, it reduces to $E_{\boldsymbol{k},\pm} = \pm E_{\boldsymbol{k}}$. For $t=0$, it becomes $E_{\boldsymbol{k},\pm} = \varepsilon'_{\boldsymbol{k}} \pm |M|$, and the model describes two decoupled FMs with opposite magnetization (hence vanishing total magnetization). We call the former the "AF transport limit", and the latter the "FM transport limit". More generally, the model is in the "AF transport regime" for $t \gg t'$, and in the "FM transport regime" for $t \ll t'$.

In the following, we calculate the electron spin densities, $\langle\hat{\boldsymbol{\sigma}}_n\rangle$ and $\langle\hat{\boldsymbol{\sigma}}_\ell\rangle$, in response to an applied electric field $\boldsymbol{E}$, using the linear response theory and the Green's function method [44, 45, 29]. The effects of impurities are considered in the Born approximation together with ladder vertex corrections. Details of the calculation are presented in the appendices.

4.3.1 Spin-transfer torque via uniform spin density: $\boldsymbol{v}_n$

The STT $\boldsymbol{v}_n$ that arises through the uniform spin density $\langle\hat{\boldsymbol{\sigma}}_\ell\rangle$ is obtained as

$$\boldsymbol{v}_n = \frac{-e\hbar\boldsymbol{E}}{s_n} M^2\Lambda \sum_{\eta=\pm1} \frac{1}{N}\sum_{\boldsymbol{k}} \frac{(v_i^0)^2-(v_i')^2}{2E_{\boldsymbol{k}}|\eta E_{\boldsymbol{k}}\gamma_0 + M\gamma_3|} \times \frac{\eta E_{\boldsymbol{k}}\gamma_3 + M\gamma_0}{\eta E_{\boldsymbol{k}}\gamma_0 + M\gamma_3}\delta(\mu-\varepsilon'_{\boldsymbol{k}}-\eta E_{\boldsymbol{k}}), \tag{4.27}$$

where $v_i^0 = \partial_i\varepsilon_{\boldsymbol{k}}$ is the velocity coming from the n.n. hopping, and $v_i' = \partial_i\varepsilon'_{\boldsymbol{k}}$ from the n.n.n. hopping. The effects of damping surface through $\gamma_0 = \pi n_{\rm i} u_{\rm i}^2 \sum_{\eta=\pm1}\frac{1}{N}\sum_{\boldsymbol{k}}\delta(\mu-\varepsilon'_{\boldsymbol{k}}-\eta E_{\boldsymbol{k}})$ and $\gamma_3 = \pi n_{\rm i} u_{\rm i}^2 M \sum_{\eta=\pm1}\frac{1}{N}\sum_{\boldsymbol{k}}\delta(\mu-\varepsilon'_{\boldsymbol{k}}-\eta E_{\boldsymbol{k}})/(\eta E_{\boldsymbol{k}})$, where N is the total number of sites. The chemical potential μ is measured from the AF gap center at $t'=0$. The impurity ladder vertex correction is considered through $\Lambda = (1-\Lambda_1)^{-1}$, where

$$\Lambda_1 = \frac{\pi n_{\rm i} u_{\rm i}^2}{\gamma_0}\sum_{\eta=\pm1}\frac{1}{N}\sum_{\boldsymbol{k}}\frac{\varepsilon_{\boldsymbol{k}}^2}{E_{\boldsymbol{k}}}\frac{\delta(\mu-\varepsilon'_{\boldsymbol{k}}-\eta E_{\boldsymbol{k}})}{|\eta E_{\boldsymbol{k}} + M(\gamma_3/\gamma_0)|}. \tag{4.28}$$

In the AF transport limit, $t'=0$, one has $\Lambda = (\mu^2+M^2)/(2M^2)$, and $\boldsymbol{v}_n$ reduces to

$$\boldsymbol{v}_n = -\frac{\hbar}{2es_n}\frac{\mu M}{\mu^2-M^2}\,\sigma_{xx}\boldsymbol{E} \qquad (t'=0), \tag{4.29}$$

where $\sigma_{xx} = 2e^2 D\nu$ is the longitudinal conductivity, $D = \frac{1}{N}\sum_{\boldsymbol{k}}(\partial_x E_{\boldsymbol{k}})^2\delta(|\mu|-E_{\boldsymbol{k}})\tau/\nu$ is the diffusion constant, $\tau = (1/2)(\gamma_0 + M\gamma_3/\mu)^{-1}$ is the scattering time, and $\nu = \frac{1}{N}\sum_{\boldsymbol{k}}\delta(|\mu|-E_{\boldsymbol{k}})$ is the density of states per spin, all evaluated at $t'=0$. This result agrees with the one reported in Ref. [29] (See chapter 3).

In the opposite limit, $t=0$, we retrieve the STT for FMs [44, 45]

$$\boldsymbol{v}_n = -\frac{\hbar}{2es_n}\left(\sigma_\uparrow - \sigma_\downarrow\right)\boldsymbol{E} \qquad (t=0), \tag{4.30}$$

where $\sigma_{\uparrow/\downarrow}$ is the longitudinal conductivity of electrons in band $\varepsilon'_{\boldsymbol{k}} \mp M$. We find that the sign of the STT in the AF transport regime, Eq. (4.29), is opposite to that in the FM transport regime, Eq. (4.30).

Numerical plots of $\boldsymbol{v}_n$ are shown in the upper panel in Fig. 4.1, including those with other values of t and t'. We set $t = (1-x)\,t_0$ and $t' = x\,t_0$, which

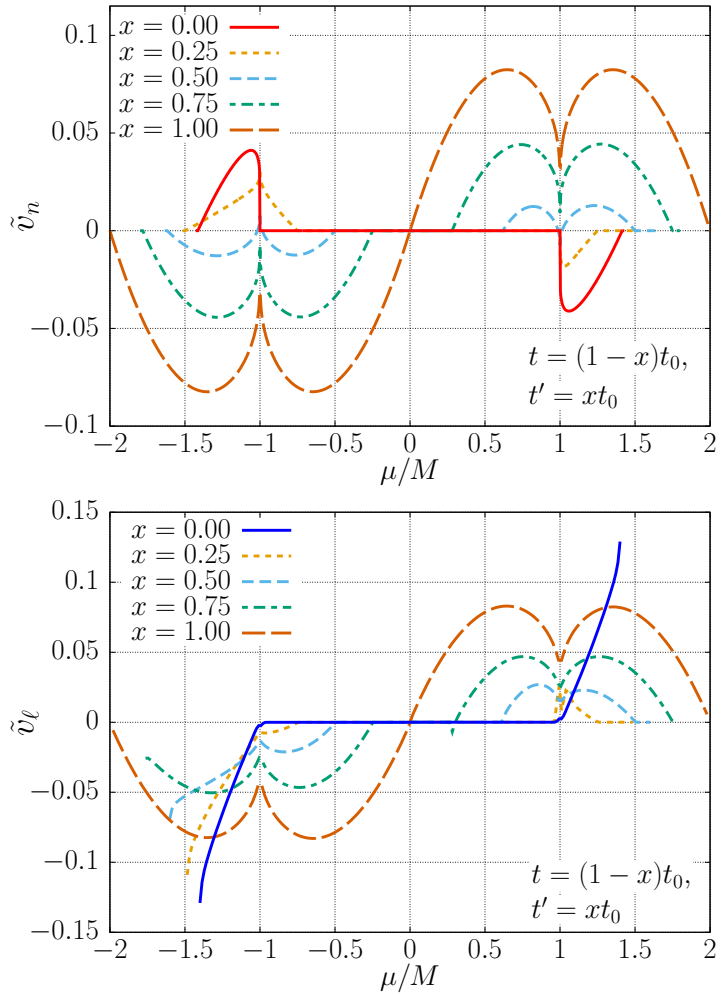

Figure 4.1: The STT coefficients, v_n (upper panel) and v_ℓ (lower panel), as functions of chemical potential μ for several choices of x, where $t = (1-x)\,t_0$ and $t' = x\,t_0$ with $t_0/M = 0.25$. Plotted are the normalized values, $\tilde{v}_n = (\boldsymbol{v}_n \cdot \boldsymbol{E}) s_n \tilde{\gamma}/(e\hbar|\boldsymbol{E}|^2)$ and $\tilde{v}_\ell = (\boldsymbol{v}_\ell \cdot \boldsymbol{E}) s_n \tilde{\gamma}/(e\hbar|\boldsymbol{E}|^2)$, where $\tilde{\gamma} = \pi n_{\rm i} u_{\rm i}^2/M^2$ is the dimensionless damping parameter. The choice $t_0/M = 0.25$ corresponds to a "strong AF", in which the upper and lower bands do not overlap. The following features are seen. (i) v_n changes sign as x is increased from $x = 0$ (AF transport limit) to $x = 1$ (FM transport limit), whereas v_ℓ keeps the same sign throughout. (ii) v_ℓ coincides with v_n at $x = 1$. (iii) v_n and v_ℓ are odd functions of μ at $x = 0$ and 1 because of the presence of particle-hole symmetry, but not for general x.

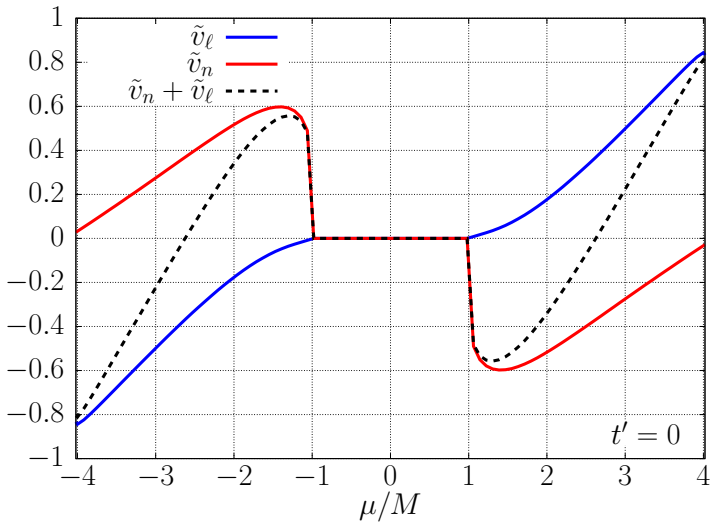

Figure 4.2: Normalized STT coefficients, $\tilde{v}_n$ (red), $\tilde{v}_\ell$ (blue) and $\tilde{v}_n + \tilde{v}_\ell$ (black), calculated with $t/M = 1$ and $t' = 0$. The total Doppler shift $v_n + v_\ell$ changes sign as a function of μ.

interpolate the AF transport regime ($x \sim 0$) and the FM transport regime ($x \sim 1$). As seen, v_n changes sign as x is increased from $x = 0$ to 1. This means that the STT due to $\boldsymbol{v}_n$ has opposite sign between FM and AF. This fact has been used in Ref. [29] to interpret the experimental result of domain wall motion in a compensated ferrimagnet GdFeCo, [16] which is expected to be in the AF transport regime [54].

4.3.2 Spin-transfer torque via staggered spin density: $\boldsymbol{v}_\ell$

The STT $\boldsymbol{v}_\ell$ arising from the staggered spin density $\langle \hat{\boldsymbol{\sigma}}_n \rangle$ is calculated by considering the canting moment $\tilde{\boldsymbol{l}}$ [23]. In the AF transport limit $t' = 0$, we obtain

$$\boldsymbol{v}_\ell = \frac{\hbar}{2es_n} M\tau \left[\frac{\mu^2 - M^2}{\mu D d} + 2\zeta \right] \sigma_{xx} \boldsymbol{E} \qquad (t' = 0), \tag{4.31}$$

where ζ comes from the impurity correction to the $\tilde{\boldsymbol{l}}$-vertex (see Fig. 4.3 (c) and Eq. (4.44) in appendix). As seen from Fig. 4.1 (blue line in the lower panel) and Fig. 4.2, the sign of $\boldsymbol{v}_\ell$ relative to $\boldsymbol{E}$ is negative (hence positive

relative to the electron flow) in the lower band, and $\boldsymbol{v}_\ell$ remains finite at the band bottom. These are in contrast to $\boldsymbol{v}_n$. As a result, the total Doppler shift $(\boldsymbol{v}_n + \boldsymbol{v}_\ell)/2$ is dominated by $\boldsymbol{v}_\ell$, hence is negative, at the band bottom. As the chemical potential is shifted to the AF gap edge, $\boldsymbol{v}_n$ starts to take over and the Doppler shift undergoes a sign change.

In the FM transport limit $t = 0$, we find

$$\boldsymbol{v}_\ell = -\frac{\hbar}{2es_n}(\sigma_\uparrow - \sigma_\downarrow)\,\boldsymbol{E} \qquad (t = 0), \tag{4.32}$$

which coincides with $\boldsymbol{v}_n$ in Eq. (4.30). Thus, the AF spin waves receive a Doppler shift by $(\boldsymbol{v}_n + \boldsymbol{v}_\ell)/2 = \boldsymbol{v}_\ell$, and this is exactly the Doppler shift in FM.

For other t, t' values, we have numerically evaluated Eqs. (4.59)-(4.62) given in appendix C, and the results are plotted in the lower panel in Fig. 4.1. In contrast to $\boldsymbol{v}_n$, it does not change sign with x, hence its sign is always that of FM.

While both $\boldsymbol{v}_n$ and $\boldsymbol{v}_\ell$ appear in the spin-wave Doppler shift, only $\boldsymbol{v}_n$ appears in the collective-coordinate equations of AF domain wall motion [24, 27, 29]. Thus, in contrast to FM, in which there is only one kind of STT, AFs allow two kinds of STT that play different roles depending on the physical phenomena.

4.4 Summary

In this chapter, we have studied STTs in AF that induce a Doppler shift in spin-wave spectrum. Unlike in FM, the Doppler shift is induced by two kinds of adiabatic STTs, identified as $\boldsymbol{v}_n$ and $\boldsymbol{v}_\ell$, which arise through uniform and staggered electron spin densities, respectively, and are proportional to the spatial gradient of the Néel vector and the uniform moment, respectively. Both STTs contribute to the spin-wave Doppler shift equally. This contrasts with the effects on AF domain walls, to which only $\boldsymbol{v}_n$ is relevant.

We next determined the STTs microscopically using a tight-binding model with n.n. and n.n.n. hopping. In the AF transport regime dominated by n.n. hopping, $\boldsymbol{v}_n$ and $\boldsymbol{v}_\ell$ have opposite signs, and the sign of the Doppler shift depends on band filling. In the FM transport limit with only the n.n.n. hopping, both $\boldsymbol{v}_n$ and $\boldsymbol{v}_\ell$ coincide with the well-known STT in FM, and add up to reproduce the Doppler shift in FM.

4.A Appendix: Green's function

In the following appendices, we present the calculation of the uniform spin density $\mathcal{R}^{-1}\langle\hat{\boldsymbol{\sigma}}_\ell\rangle$ and the staggered spin density $\mathcal{R}^{-1}\langle\hat{\boldsymbol{\sigma}}_n\rangle$ (in the rotated frame), or $\langle\hat{\boldsymbol{\sigma}}_\ell\rangle$ and $\langle\hat{\boldsymbol{\sigma}}_n\rangle$ (in the original frame), in response to an external electric field, to obtain $\boldsymbol{v}_n$ and $\boldsymbol{v}_l$, respectively.

The unperturbed Hamiltonian is written as

$$H_0 = \sum_{\boldsymbol{k}} c_{\boldsymbol{k}}^\dagger h_{\boldsymbol{k}} c_{\boldsymbol{k}}, \tag{4.33}$$

where $c_{\boldsymbol{k}} = {}^t(c_{\boldsymbol{k}\uparrow,A}, c_{\boldsymbol{k}\downarrow,A}, c_{\boldsymbol{k}\uparrow,B}, c_{\boldsymbol{k}\downarrow,B})$ and

$$h_{\boldsymbol{k}} = \varepsilon'_{\boldsymbol{k}} + \varepsilon_{\boldsymbol{k}}\tau_1 - M\sigma^z\tau_z. \tag{4.34}$$

The Pauli matrices that act in the sublattice (spin) space are denoted by $\boldsymbol{\tau}$ ($\boldsymbol{\sigma}$). The retarded Green's function of the unperturbed Hamiltonian is

$$G^R = \mu^R + T^R\tau_1 + J^R\sigma^3\tau_3, \tag{4.35}$$

where $\mu^R = (\mu - \varepsilon'_{\boldsymbol{k}} + i\gamma_0)/D^R$, $T^R = \varepsilon_{\boldsymbol{k}}/D^R$, $J^R = (-M + i\gamma_3)/D^R$, and $D^R = (\mu - \varepsilon'_{\boldsymbol{k}} + i\gamma_0)^2 - \varepsilon_{\boldsymbol{k}}^2 - (-M + i\gamma_3)^2$, and the advanced Green's function is given by its Hermitian conjugate, $G^A = (G^R)^\dagger$. The velocity operator is given by

$$v_i = v_i^0\tau_1 + v'_i. \tag{4.36}$$

The spin gauge field appears through the perturbative Hamiltonian, $H_A = \sum_{\boldsymbol{k}} c_{\boldsymbol{k}}^\dagger v_i A_i c_{\boldsymbol{k}}$, and the anomalous velocity, $(\partial_j v_i)A_j$. The spin gauge field is expanded using Pauli matrices as $A_i = \boldsymbol{A}_i \cdot \boldsymbol{\sigma}/2$, where the perpendicular component of the spin gauge field is given by $\boldsymbol{A}_i - A_i^z\hat{z} = -\mathcal{R}^{-1}(\boldsymbol{n} \times \partial_i \boldsymbol{n})$.

The effect of $V_{\rm imp}$ is considered in the Born approximation and ladder type vertex correction, as shown in Fig. 4.3 (a), (b), and (c).

4.B Appendix: Calculation of $\boldsymbol{v}_n$

Here, we calculate the uniform spin density $\mathcal{R}^{-1}\langle\hat{\boldsymbol{\sigma}}_\ell\rangle$. The first two diagrams in Fig. 4.3 are given by

$$\text{(e1)} + \text{(e2)} = \frac{1}{2\pi}\frac{1}{N}\sum_{\boldsymbol{k}} \mathrm{tr}\left[\sigma^\alpha G^R v_i A_i G^R v_i (-eE_i) G^A\right] + \text{c.c.}, \tag{4.37}$$

and the third diagram in Fig. 4.3 is given by

$$(\mathrm{e3}) = \frac{1}{2\pi}\frac{1}{N}\sum_{\boldsymbol{k}} \mathrm{tr}\big[\sigma^\alpha G^R(\partial_i v_i)A_i(-eE_i)G^A\big]. \tag{4.38}$$

Adding up the terms (e1), (e2), and (e3) determines the spin density $(\mathcal{R}^{-1}\boldsymbol{\sigma}_\ell)^\alpha$ in response to an electric field E_i, without the effect of vertex correction taken into account. Note that we are only interested in $\alpha = x, y$ because $\hat{\boldsymbol{\sigma}}_\ell \perp \boldsymbol{n}$. From this it follows that the z component of the spin gauge field A_i^z does not contribute.

Integrating by parts, and using the relation $\partial_i G^R = G^R v_i G^R$, (e3) can be merged with (e1)+(e2),

$$\begin{aligned}(\mathrm{e1})+(\mathrm{e2})+(\mathrm{e3}) = \frac{1}{4\pi}A_i^\beta\frac{1}{N}\sum_{\boldsymbol{k}}\Big[&(v_i^0)^2\,\mathrm{tr}\big\{\sigma^\alpha G^R\tau_1(\sigma^\beta G^R - G^R\sigma^\beta)\tau_1 G^A\big\}\\ &+(v_i')^2\,\mathrm{tr}\big\{\sigma^\alpha G^R(\sigma^\beta G^R - G^R\sigma^\beta)G^A\big\}\Big](-eE_i) + \mathrm{c.c.}\end{aligned} \tag{4.39}$$

Evaluating the trace and approximating the product of the Green's functions by a delta function, one obtains

$$\begin{aligned}&(\mathrm{e1})+(\mathrm{e2})+(\mathrm{e3})\\ &= -MA_i^\alpha\sum_{\eta=\pm1}\frac{1}{N}\sum_{\boldsymbol{k}}\frac{(v_i^0)^2-(v_i')^2}{2E_{\boldsymbol{k}}|\eta E_{\boldsymbol{k}}\gamma_0+M\gamma_3|}\frac{\eta E_{\boldsymbol{k}}\gamma_3+M\gamma_0}{\eta E_{\boldsymbol{k}}\gamma_0+M\gamma_3}\\ &\qquad\times\delta(\mu-\varepsilon'_{\boldsymbol{k}}-\eta E_{\boldsymbol{k}})(-eE_i).\end{aligned} \tag{4.40}$$

These are for diagrams without vertex corrections. The effect of vertex corrections is taken into account by multiplying the above result by Λ, and we can now write the current induced uniform spin density as

$$\begin{aligned}\langle\boldsymbol{\sigma}_\ell\rangle = M\boldsymbol{n}\times\partial_i\boldsymbol{n}\,\Lambda\sum_{\eta=\pm1}\frac{1}{N}\sum_{\boldsymbol{k}}&\frac{(v_i^0)^2-(v_i')^2}{2E_{\boldsymbol{k}}|\eta E_{\boldsymbol{k}}\gamma_0+M\gamma_3|}\frac{\eta E_{\boldsymbol{k}}\gamma_3+M\gamma_0}{\eta E_{\boldsymbol{k}}\gamma_0+M\gamma_3}\\ &\times\delta(\mu-\varepsilon'_{\boldsymbol{k}}-\eta E_{\boldsymbol{k}})(-eE_i).\end{aligned} \tag{4.41}$$

4.C Appendix: Calculation of $\boldsymbol{v}_\ell$

Here, we calculate the staggered spin density $\mathcal{R}^{-1}\langle\hat{\boldsymbol{\sigma}}_n\rangle$ in response to an external electric field, and obtain $\boldsymbol{v}_\ell$. We are interested in the first-order

terms in the uniform moment $\tilde{\boldsymbol{l}}$, perturbed through

$$H_\ell = -M \sum_{\boldsymbol{k}} (\mathcal{R}^{-1}\tilde{\boldsymbol{l}}) \cdot \boldsymbol{\sigma}. \tag{4.42}$$

The relevant diagrams are depicted in Fig. 4.3 (f). The first four diagrams (without vertex correction) give

$$\begin{aligned}
&\text{(f1)} + \cdots + \text{(f4)} \\
&= \frac{1}{2\pi}(1+i\zeta)(-M\mathcal{R}^{-1}\tilde{\boldsymbol{l}})^\beta(-eE_i) \\
&\quad \times \frac{1}{N}\sum_{\boldsymbol{k}} \Big\{ \mathrm{tr}\big[\boldsymbol{\sigma}^\perp \tau_3 G^R \sigma^\beta G^R v_j A_j G^R v_i G^A\big] + \mathrm{tr}\big[\boldsymbol{\sigma}^\perp \tau_3 G^R v_j A_j G^R \sigma^\beta G^R v_i G^A\big] \\
&\qquad\qquad + \mathrm{tr}\big[\boldsymbol{\sigma}^\perp \tau_3 G^R \sigma^\beta G^R v_i G^A v_j A_j G^A\big] + \mathrm{tr}\big[\boldsymbol{\sigma}^\perp \tau_3 G^R \sigma^\beta G^R (\partial_j v_i) A_j G^A\big] \Big\},
\end{aligned} \tag{4.43}$$

where ζ comes from the impurity correction to the $\tilde{\boldsymbol{l}}$-vertex, Fig. 4.3 (c),

$$\zeta = n_{\mathrm{i}} u_{\mathrm{i}}^2 \,\mathrm{Im}\left[\frac{2}{N}\sum_{\boldsymbol{k}} (\mu^R)^2 + (T^R)^2 - (J^R)^2\right]. \tag{4.44}$$

The trace is nonvanishing only for $A^z\sigma^z/2$ in A_j, which is, however, not gauge-invariant. Note also that the $\boldsymbol{k}$-integrals vanish by symmetry unless $j = i$. Integrating by parts and evaluating the traces, one has

$$\begin{aligned}
&\text{(f1)} + \cdots + \text{(f4)} \\
&= \frac{1}{2\pi}(1+i\zeta)(-M\mathcal{R}^{-1}\tilde{\boldsymbol{l}})^\beta 4A_i^z\,(-eE_i) \\
&\quad \times \frac{1}{N}\sum_{\boldsymbol{k}} \Big[(v_i^0)^2 \big\{ ((\mu^R)^2 + 3(T^R)^2 - (J^R)^2)(\mu^A J^R - J^A \mu^R) \big\} \\
&\qquad + (v_i')^2 \big\{ ((\mu^R)^2 + (T^R)^2 - (J^R)^2)(\mu^A J^R - J^A \mu^R) \\
&\qquad\qquad - 2\mu^R T^R (T^R J^A - J^R T^A) - 2T^R J^R (T^R \mu^A - \mu^R T^A) \big\} \\
&\qquad - 2v_i^0 v_i' \big\{ 2\mu^R T^R (\mu^R J^A - \mu^A J^R) \\
&\qquad\qquad + ((\mu^R)^2 - (J^R)^2 + (T^R)^2)(T^R J^A - J^R T^A) \big\} \Big].
\end{aligned} \tag{4.45}$$

Next we look at the fifth diagram in Fig. 4.3 (f),

$$\begin{aligned}(\mathrm{f5}) = \frac{1}{2\pi}(1+i\zeta)(-M\mathcal{R}^{-1}\tilde{\boldsymbol{l}})^\beta(-eE_i) \\ \times \frac{1}{N}\sum_{\boldsymbol{k}} \mathrm{tr}[\boldsymbol{\sigma}^\perp\tau_3 G_+^R\sigma^\beta G_-^R(\partial_i v_{i-})\tau_1 G_-^A],\end{aligned} \tag{4.46}$$

in which the wave vector $\boldsymbol{q}$ needs to be extracted from the Green's functions, $G_\pm^{R/A} \equiv G^{R/A}_{\boldsymbol{k}\pm\boldsymbol{q}/2}$, or from the velocity vertex, $v_{i\pm} = v_{i,\boldsymbol{k}\pm\boldsymbol{q}/2}$. To first order in $\boldsymbol{q}$, and after integrating by parts, one has

$$\begin{aligned}(\mathrm{f5}) = \frac{1}{2\pi}(1+i\zeta)(-M\mathcal{R}^{-1}\tilde{\boldsymbol{l}})^\beta q_i(-eE_i) \\ \times \frac{1}{N}\sum_{\boldsymbol{k}} \mathrm{tr}[\boldsymbol{\sigma}^\perp\tau_3 G^R v_i G^R\sigma^\beta G^R v_i\tau_1 G^A].\end{aligned} \tag{4.47}$$

The trace is evaluated to give

$$\begin{aligned}(\mathrm{f5}) = \frac{1}{2\pi}(1+i\zeta)\,4\hat{z}\times(-M\mathcal{R}^{-1}\tilde{\boldsymbol{l}}\,)\,iq_i(-eE_i) \\ \times\frac{1}{N}\sum_{\boldsymbol{k}}\Big\{(v_i^0)^2((\mu^R)^2+3(T^R)^2-(J^R)^2)(J^R\mu^A-\mu^R J^A) \\ +(v_i')^2\Big[((\mu^R)^2+(T^R)^2-(J^R)^2)(\mu^A J^R-\mu^R J^A) \\ -2\mu^R T^R(T^R J^A-J^R T^A)-2T^R J^R(T^R\mu^A-T^A\mu^R)\Big] \\ -2v_i^0 v_i'\Big[((\mu^R)^2+(T^R)^2-(J^R)^2)(T^R J^A-J^R T^A) \\ +2\mu^R T^R(\mu^R J^A-J^R\mu^A)\Big]\Big\}.\end{aligned} \tag{4.48}$$

Taking $iq_i \to \partial_i$ and using the relation

$$\hat{z}\times(\partial_i\mathcal{R}^{-1})\,\tilde{\boldsymbol{l}} = \hat{z}\times(\boldsymbol{A}_i\times\mathcal{R}^{-1}\tilde{\boldsymbol{l}}\,) \tag{4.49}$$

$$= -A_i^z\mathcal{R}^{-1}\tilde{\boldsymbol{l}}, \tag{4.50}$$

we see that (f5) cancels the gauge-noninvariant terms in (f1) + ⋯ + (f4).

The vertex correction is taken into account by the replacement,

$$\sigma^\perp\tau_3 \to i\sigma^\perp\sigma^3\Lambda_3, \tag{4.51}$$

where Λ_3 is given by

$$\Lambda_3 = \frac{2\pi n_{\rm i} u_{\rm i}^2}{1-\Lambda_1}\frac{1}{N}\sum_{\boldsymbol{k}}\frac{(\mu-\varepsilon'_{\boldsymbol{k}})\gamma_3 + M\gamma_0}{|(\mu-\varepsilon'_{\boldsymbol{k}})\gamma_0 + M\gamma_3|}\delta((\mu-\varepsilon'_{\boldsymbol{k}})^2 - E_{\boldsymbol{k}}^2). \tag{4.52}$$

This is simplified in the AF transport limit,

$$\Lambda_3 = \frac{\gamma_0}{M} \qquad (t'=0), \tag{4.53}$$

and also in the FM transport limit,

$$\Lambda_3 = \frac{\gamma_0}{M} \qquad (t=0). \tag{4.54}$$

The next four diagrams (with vertex corrections) give

$$\begin{aligned}
&\text{(f1V)} + \cdots + \text{(f4V)} \\
=&\frac{1}{2\pi} i\Lambda_3(1+i\zeta)(-M\mathcal{R}^{-1}\tilde{\boldsymbol{l}})^\beta(-eE_i) \\
&\times\frac{1}{N}\sum_{\boldsymbol{k}}\Big\{\mathrm{tr}[\sigma^\perp\sigma^3 G^R\sigma^\beta G^R A_i v_i G^R v_i G^A] \\
&\qquad + \mathrm{tr}[\sigma^\perp\sigma^3 G^R A_i v_i G^R\sigma^\beta G^R v_i G^A] \\
&\qquad + \mathrm{tr}[\sigma^\perp\sigma^3 G^R\sigma^\beta G^R v_i G^A A_i v_i G^A] \\
&\qquad + \mathrm{tr}[\sigma^\perp\sigma^3 G^R\sigma^\beta G^R A_i(\partial_i v_i) G^A]\Big\}
\end{aligned} \tag{4.55}$$

and the trace is evaluated as

$$\begin{aligned}
&\text{(f1V)} + \cdots + \text{(f4V)} \\
=&\frac{1}{2\pi} i\Lambda_3(1+i\zeta)(-M\mathcal{R}^{-1}\tilde{\boldsymbol{l}})\,4A_i^z(-eE_i) \\
&\times\frac{1}{N}\sum_{\boldsymbol{k}}\Big\{(v_i^0)^2\Big[((\mu^R)^2+(T^R)^2-(J^R)^2)(\mu^R\mu^A + T^RT^A - J^RJ^A) \\
&\qquad + 2\mu^RT^R(T^R\mu^A + \mu^RT^A) - 2T^RJ^R(J^RT^A + T^RJ^A)\Big] \\
&\quad + (v_i')^2\Big[((\mu^R)^2-(T^R)^2-(J^R)^2)(\mu^R\mu^A - T^RT^A - J^RJ^A) \\
&\qquad + 4\mu^RT^R(\mu^AT^R + \mu^RT^A)\Big] \\
&\quad + 2v_i^0v_i'\Big[((\mu^R)^2+(T^R)^2-(J^R)^2)(T^R\mu^A + \mu^RT^A) \\
&\qquad + 2\mu^RT^R(\mu^R\mu^A + T^RT^A - J^RJ^A)\Big]\Big\}.
\end{aligned} \tag{4.56}$$

The last diagram in Fig. 4.3 (f) gives

$$\begin{aligned}(\mathrm{f5V}) =&\frac{1}{2\pi} i\Lambda_3(1+i\zeta)(-M\mathcal{R}^{-1}\tilde{\boldsymbol{l}})^\beta q_i\,(-eE_i)\\ &\times\frac{1}{N}\sum_{\boldsymbol{k}}\mathrm{tr}[\sigma^\perp\sigma^3 G^R v_i G^R\sigma^\beta G^R v_i G^A] \qquad (4.57)\\ =&\frac{1}{2\pi} i\Lambda_3(1+i\zeta)(-M\mathcal{R}^{-1}\tilde{\boldsymbol{l}})\,q_i\,(-eE_i)\,\mathrm{tr}[\sigma^\perp\sigma^3\sigma^\beta]\\ &\times\frac{1}{N}\sum_{\boldsymbol{k}}\Big\{(v_i^0)^2\Big[((\mu^R)^2+(T^R)^2-(J^R)^2)(\mu^R\mu^A+T^RT^A-J^RJ^A)\\ &\qquad+2\mu^RT^R(T^R\mu^A+\mu^RT^A)-2T^RJ^R(J^RT^A+T^RJ^A)\Big]\\ &+(v_i')^2\Big[((\mu^R)^2-(T^R)^2-(J^R)^2)(\mu^R\mu^A-T^RT^A-J^RJ^A)\\ &\qquad+4\mu^RT^R(\mu^AT^R+\mu^RT^A)\Big]\\ &+2v_i^0v_i'\Big[((\mu^R)^2+(T^R)^2-(J^R)^2)(\mu^RT^A+T^R\mu^A)\\ &\qquad+2\mu^RT^R(\mu^R\mu^A+T^RT^A-J^RJ^A)\Big]\Big\}. \qquad (4.58)\end{aligned}$$

Thus, we see that the gauge-noninvariant terms in (f5V) are canceled out by (f1V) $+\cdots$ (f4V). It is clear that the effect of vertex correction is absent when $t=0$. When $t'=0$, (f5V) is equal to (f5) $\times\,(\mu^2-M^2)/(2M^2)$. Adding up all diagrams in Fig. 4.3 (f), the current induced staggered spin density is given by

$$\langle\boldsymbol{\sigma}_n\rangle=\frac{2}{\pi}\,(-M\boldsymbol{n}\times\partial_i\tilde{\boldsymbol{l}}\,)\,(-eE_i)\,\frac{1}{N}\sum_{\boldsymbol{k}}\Big\{(v_i^0)^2C_1+(v_i')^2\,C_2+2v_i^0v_i'\,C_3\Big\} \qquad (4.59)$$

where the coefficient of $(v_i^0)^2$ is given by

$$\begin{aligned}C_1=&(1+i\zeta)\Big[((\mu^R)^2+3(T^R)^2-(J^R)^2)(J^R\mu^A-\mu^RJ^A)\\ &+i\Lambda_3\Big\{((\mu^R)^2+(T^R)^2-(J^R)^2)(\mu^R\mu^A+T^RT^A-J^RJ^A)\\ &\qquad+2\mu^RT^R(T^R\mu^A+\mu^RT^A)-2T^RJ^R(J^RT^A+T^RJ^A)\Big\}\Big]+\mathrm{c.c.}\end{aligned} \qquad (4.60)$$

the coefficient of $(v_i')^2$ is given by

$$\begin{aligned} C_2 =&(1+i\zeta)\Big[((\mu^R)^2+(T^R)^2-(J^R)^2)(\mu^A J^R-\mu^R J^A) \\ &-2\mu^R T^R(T^R J^A-J^R T^A)-2T^R J^R(T^R\mu^A-T^A\mu^R) \\ &+i\Lambda_3\Big\{((\mu^R)^2-(T^R)^2-(J^R)^2)(\mu^R\mu^A-T^R T^A-J^R J^A) \\ &\quad+4\mu^R T^R(\mu^A T^R+\mu^R T^A)\Big\}\Big]+\text{c.c.} \end{aligned} \tag{4.61}$$

and the coefficient of $2v_i^0 v_i'$ is given by

$$\begin{aligned} C_3 =&(1+i\zeta)\Big[-((\mu^R)^2+(T^R)^2-(J^R)^2)(T^R J^A-J^R T^A) \\ &-2\mu^R T^R(\mu^R J^A-J^R\mu^A) \\ &+i\Lambda_3\Big\{((\mu^R)^2+(T^R)^2-(J^R)^2)(\mu^R T^A+T^R\mu^A) \\ &\quad+2\mu^R T^R(\mu^R\mu^A+T^R T^A-J^R J^A)\Big\}\Big]+\text{c.c.} \end{aligned} \tag{4.62}$$

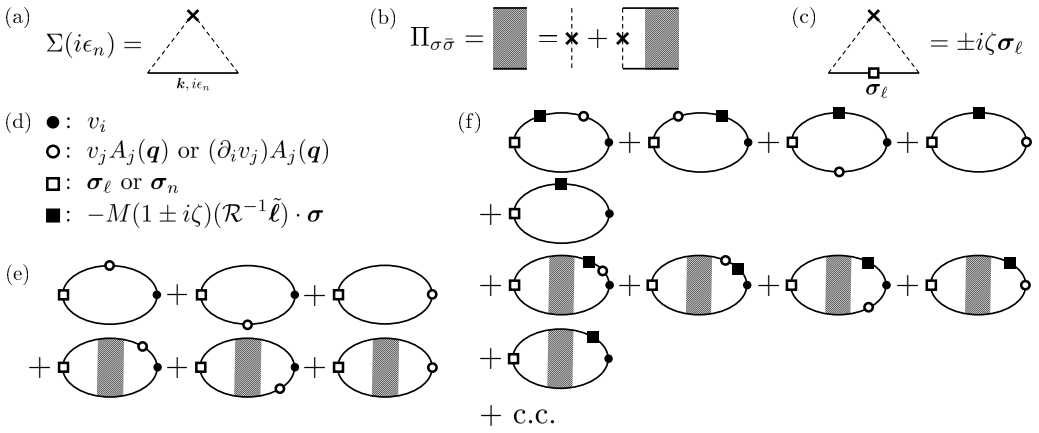

Figure 4.3: Feynman diagrams considered in the calculation. The impurities are treated as in (a)-(c), and the calculated electron spin polarizations are shown in (e) and (f), with the vertices defined in (d). The solid line represents the electron Green's function, and the dashed line with a cross represents nonmagnetic impurity scattering. (a) Self-energy in the Born approximation. (b) Four-point vertex in the ladder approximation. The upper (lower) electron line is in the retarded (advanced) branch and has spin σ ($\bar{\sigma}$). (c) Impurity correction to the (static) $\tilde{\boldsymbol{l}}$-vertex. The plus (minus) sign is for the retarded (advanced) branch. (d) Definition of vertices. The filled circle (●) represents the current vertex v_i^0 that couples to the external electric field E_i. The empty circle (○) is associated with the spin gauge field A_i, coming either from the perturbation Hamiltonian, $v_l A_l(\boldsymbol{q})$, or from the current vertex, $(\partial_i v_i)\boldsymbol{A}_i(\boldsymbol{q})$. The empty square (□) represents the uniform ($\boldsymbol{\sigma}_\ell$) or staggered ($\boldsymbol{\sigma}_n$) spin density. The filled square (■) is the $\tilde{\boldsymbol{l}}$-vertex with impurity correction. In (e) and (f), the right vertex represents the charge current that couples to $\boldsymbol{E}$, and the upper (lower) electron lines are in the retarded (advanced) branch. (e) Diagrams for the "uniform" spin density, $\boldsymbol{\sigma}_\ell$, in first order in A_i. (f) Diagrams for the "staggered" spin density, $\boldsymbol{\sigma}_n$, in first order in $\tilde{\boldsymbol{l}}$. The diagrams with ○ (spin gauge field) only give gauge-noninvariant terms ($\propto A_i^z$), which cancel those arising from $(\partial_i \mathcal{R}^{-1})\tilde{\boldsymbol{l}}$ in the remaining diagrams.

Chapter 5

Summary

Spin electronics, or spintronics for short, aims to utilize both the magnetic and electric properties of electrons to expand upon the conventional physics of electronics. So far, spintronics has proven itself useful through the discovery of the Nobel prize winning giant magneto resistance and magnetoresistive random access memories.

Such remarkable discoveries were made in ferromagnets, and research in other classes of materials such as antiferromagnets (AFs) remain relatively limited. AF is another class of magnetic material that has a number of advantages over ferromagnets, such as the robustness to magnetic perturbations, THz range spin dynamics, and absence of stray fields. Immunity to external magnetic fields and absence of stray fields is however a double-edged sword, and makes the manipulation and measurement of AFs a challenge compared to ferromagnets. In this thesis, I theoretically explore different ways to tame AFs to our advantage.

A domain wall is a topologically stable texture in magnetic materials that is expected to play an important role as information carriers in spintronic devices. Dynamics of domain walls is one of the most fundamental processes in magnetic materials, and is of interest from both theory and application perspectives. In the first part of my thesis, I explored the dynamics of AF domain walls driven by inhomogeneous magnetic fields. The Lagrangian and the equation of motion of AF spins under an inhomogeneous magnetic field are derived. The dynamics of AF domain walls is investigated using the method of collective coordinates. A solution is found that describes the actuation of a domain wall by an inhomogeneous field, in which the motion is initiated by a paramagnetic response of wall magnetization, which is then

driven by a Stern-Gerlach like force. The validity of the theory is backed up by atomistic simulations.

In the second part of the thesis, I explored the effect of conduction electrons on AF spins. A microscopic calculation is presented for current-induced spin-transfer torques (STT) and damping torques in metallic AFs. It is found that the sign of STT is opposite to that in ferromagnets because of the AF transport character. Enhancement of the current-to-STT conversion factor near the AF gap edge is observed. The dissipative torque parameter and damping parameter arise from spin relaxation of electrons. Physical consequences are demonstrated for AF domain wall dynamics. Similarities to the ferromagnetic case are pointed out such as the intrinsic pinning and the specialty of $\alpha_n/\beta_n = 1$. Finally, I give a possible explanation for the experiment on domain wall motion in ferrimagnetic GdFeCo near its angular-momentum compensation temperature.

Spin waves are collective excitations in magnetically ordered systems that carry energy and angular momentum. In the last part of the thesis, I investigate the effect of electric current on AF spin wave dispersions. I identify two different sources of spin-wave Doppler shift induced by electric current, while in ferromagnets there is only one. The two STTs that give rise Doppler shift have opposite signs and compete against each other; one dominates at the AF band bottom, and the other dominates near the AF gap edge. The effect of next nearest-neighbor hopping is investigated, where the crossover from ferromagnetic STT to antiferromagnetic STT can be observed by tuning the hopping parameters. In the limit of only the next-nearest neighbor hopping, the two STTs coincide to form the ferromagnetic STT.

To conclude, I have investigated the effects of magnetic field and electric current on AF spin dynamics. It is shown that AF domain walls can be driven by inhomogeneous magnetic fields, and an analytic solution for the domain wall dynamics is derived. Spin-transfer torques and damping torques on AF spins are also studied starting from a microscopic Hamiltonian. The differences between AF domain wall motion and ferromagnetic domain wall motion are demonstrated. The effect of current on AF spin waves is also discussed.

Acknowledgements

This thesis would not have existed if it were not for the tremendous support that I have received from all the people I came in touch with over the years.

First and for most, I would like to thank my supervisor, Hiroshi Kohno, for guiding me through all the hardships during the last six years. Not only was he very patient and generous every time I needed his assistance, he also was a role-model to me as an ideal researcher.

Prof. Ai Yamakage for helping me out, and answering any questions no matter how basic.

I would like to thank my colleagues in my laboratory, T. Funato, Y. Imai, K. Nakazawa, Y. Ogawa, T. Yamaguchi, and Y. Yamazaki for many valuable discussions.

Thank you Prof. John Wojdylo for making physics interesting during my bachelors. All the faculty members in Nagoya university for going through the trouble of making the G30 program possible.

All my friends in Japan and overseas for keeping me company. The trips, karaoke-sessions, gaming, Skype-calls etc. made my day, and I am always up for more.

I would like to thank my family for all the unconditional financial and mental support. I feel blessed for being born in this understanding family letting me pursue my interests.

Bibliography

[1] N. Jones: Nature **561** (2018) 163.

[2] S. S. P. Parkin, M. Hayashi, and L. Thomas: Science **320** (2008) 190.

[3] G. Tatara: *Supintoronikusu no butsuri: ba no riron no tachiba kara* (Uchida rokakuho, 2019).

[4] T. Jungwirth, X. Marti, P. Wadley, and J. Wunderlich: Nature Nanotechnology **11** (2016) 231.

[5] Z. Qiu, J. Li, D. Hou, E. Arenholz, A. T. N'diaye, A. Tan, K.-I. Uchida, K. Sato, S. Okamoto, Y. Tserkovnyak, Z. Q. Qiu, and E. Saitoh: Nature Communications **7** (2016) 12670.

[6] A. H. MacDonald and M. Tsoi: Philosophical Transactions of the Royal Society of London Series A **369** (2011) 3098.

[7] O. Gomonay, T. Jungwirth, and J. Sinova: Physica Status Solidi Rapid Research Letters **11** (2017) 1700022.

[8] V. Baltz, A. Manchon, M. Tsoi, T. Moriyama, T. Ono, and Y. Tserkovnyak: Reviews of Modern Physics **90** (2018) 015005.

[9] H. Kohno and J. J. Nakane, CHAPTER 5 - Spintronics, In A. Yamaguchi, A. Hirohata, and B. Stadler (eds), *Nanomagnetic materials*. Elsevier, Amsterdam, 2021.

[10] E. G. Tveten, A. Qaiumzadeh, and A. Brataas: Phys. Rev. Lett. **112** (2014) 147204.

[11] O. Gomonay, T. Jungwirth, and J. Sinova: Phys. Rev. Lett. **117** (2016) 017202.

[12] T. Shiino, S.-H. Oh, P. M. Haney, S.-W. Lee, G. Go, B.-G. Park, and K.-J. Lee: Phys. Rev. Lett. **117** (2016) 087203.

[13] D. Herranz, R. Guerrero, R. Villar, F. G. Aliev, A. C. Swaving, R. A. Duine, C. van Haesendonck, and I. Vavra: Phys. Rev. B **79** (2009) 134423.

[14] S.-H. Yang, K.-S. Ryu, and S. Parkin: Nature Nanotechnology **10** (2015) 221.

[15] K.-J. Kim, S. K. Kim, Y. Hirata, S.-H. Oh, T. Tono, D.-H. Kim, T. Okuno, W. S. Ham, S. Kim, G. Go, Y. Tserkovnyak, A. Tsukamoto, T. Moriyama, K.-J. Lee, and T. Ono: Nature Materials **16** (2017) 1187.

[16] T. Okuno, D.-H. Kim, S.-H. Oh, S. K. Kim, Y. Hirata, T. Nishimura, W. S. Ham, Y. Futakawa, H. Yoshikawa, A. Tsukamoto, Y. Tserkovnyak, Y. Shiota, T. Moriyama, K.-J. Kim, K.-J. Lee, and T. Ono: Nature Electronics **2** (2019) 389.

[17] G. Tatara, H. Kohno, and J. Shibata: Physics Reports **468** (2008) 213.

[18] E. G. Tveten, T. Müller, J. Linder, and A. Brataas: Phys. Rev. B **93** (2016) 104408.

[19] H. Y. Yuan, W. Wang, M.-H. Yung, and X. R. Wang: Phys. Rev. B **97** (2018) 214434.

[20] N. B. Weber, H. Ohldag, H. Gomonaj, and F. U. Hillebrecht: Phys. Rev. Lett. **91** (2003) 237205.

[21] T. Dombre and N. Read: Phys. Rev. B **38** (1988) 7181.

[22] F. D. M. Haldane: Phys. Rev. Lett. **61** (1988) 1029.

[23] J. J. Nakane, K. Nakazawa, and H. Kohno: Phys. Rev. B **101** (2020) 174432.

[24] K. M. D. Hals, Y. Tserkovnyak, and A. Brataas: Phys. Rev. Lett. **106** (2011) 107206.

[25] A. Brataas, H. Skarsvåg, E. G. Tveten, and E. Løhaugen Fjærbu: Phys. Rev. B **92** (2015) 180414.

[26] B. A. Ivanov and A. K. Kolezhuk: Phys. Rev. Lett. **74** (1995) 1859.

[27] E. G. Tveten, A. Qaiumzadeh, O. A. Tretiakov, and A. Brataas: Phys. Rev. Lett. **110** (2013) 127208.

[28] F. D. M. Haldane: Phys. Rev. Lett. **50** (1983) 1153.

[29] J. J. Nakane and H. Kohno: Phys. Rev. B **103** (2021) L180405.

[30] D. Ralph and M. Stiles: Journal of Magnetism and Magnetic Materials **320** (2008) 1190.

[31] Y. B. Bazaliy, B. A. Jones, and S.-C. Zhang: Phys. Rev. B **57** (1998) R3213.

[32] A. Brataas, A. D. Kent, and H. Ohno: Nature Materials **11** (2012) 372.

[33] R. Duine: Nature Materials **10** (2011) 344.

[34] Y. Xu, S. Wang, and K. Xia: Phys. Rev. Lett. **100** (2008) 226602.

[35] A. C. Swaving and R. A. Duine: Phys. Rev. B **83** (2011) 054428.

[36] Y. Yamane, J. Ieda, and J. Sinova: Phys. Rev. B **94** (2016) 054409.

[37] H.-J. Park, Y. Jeong, S.-H. Oh, G. Go, J. H. Oh, K.-W. Kim, H.-W. Lee, and K.-J. Lee: Phys. Rev. B **101** (2020) 144431.

[38] J. Fujimoto: Phys. Rev. B **103** (2021) 014436.

[39] H. Kohno and G. Tatara, CHAPTER 5 - Theoretical Aspects of Current-Driven Magnetization Dynamics, In T. Shinjo (ed), *Nanomagnetism and Spintronics*, pp. 189–229. Elsevier, Amsterdam, 2009.

[40] S. Zhang and Z. Li: Phys. Rev. Lett. **93** (2004) 127204.

[41] H. J. Mikeska and M. Steiner: Advances in Physics **40** (1991) 191.

[42] E. M. Lifshitz and L. P. Pitaevskii: *Statistical Physics, Part II, Course of Theoretical Physics* (Pergamon, Oxford, 1980).

[43] J. J. Nakane and H. Kohno: Journal of the Physical Society of Japan **90** (2021) 034702.

[44] H. Kohno, G. Tatara, and J. Shibata: Journal of the Physical Society of Japan **75** (2006) 113706.

[45] H. Kohno and J. Shibata: Journal of the Physical Society of Japan **76** (2007) 063710.

[46] A. Manchon: Journal of Physics Condensed Matter **29** (2017) 104002.

[47] J. J. Nakane and H. Kohno: Submitted to Journal of the Physical Society of Japan .

[48] Q. Liu, H. Y. Yuan, K. Xia, and Z. Yuan: Phys. Rev. Materials **1** (2017) 061401.

[49] H. Y. Yuan, Q. Liu, K. Xia, Z. Yuan, and X. R. Wang: EPL (Europhysics Letters) **126** (2019) 67006.

[50] H. T. Simensen, A. Kamra, R. E. Troncoso, and A. Brataas: Phys. Rev. B **101** (2020) 020403.

[51] G. Tatara and H. Kohno: Phys. Rev. Lett. **92** (2004) 086601.

[52] T. Koyama, D. Chiba, K. Ueda, K. Kondou, H. Tanigawa, S. Fukami, T. Suzuki, N. Ohshima, N. Ishiwata, Y. Nakatani, K. Kobayashi, and T. Ono: Nature Materials **10** (2011) 194.

[53] K. Hoshi, T. Yamaguchi, A. Takeuchi, H. Kohno, and J.-i. Ohe: Applied Physics Letters **117** (2020) 062404.

[54] J. Park, Y. Hirata, J.-H. Kang, S. Lee, S. Kim, C. Van Phuoc, J.-R. Jeong, J. Park, S.-Y. Park, Y. Jo, A. Tsukamoto, T. Ono, S. K. Kim, and K.-J. Kim: Phys. Rev. B **103** (2021) 014421.

[55] J. Shibata and H. Kohno: Phys. Rev. B **84** (2011) 184408.

[56] M. W. Daniels, R. Cheng, W. Yu, J. Xiao, and D. Xiao: Phys. Rev. B **98** (2018) 134450.

[57] P. Lederer and D. L. Mills: Phys. Rev. **148** (1966) 542.

[58] V. Vlaminck and M. Bailleul: Science **322** (2008) 410.

[59] S.-M. Seo, K.-J. Lee, H. Yang, and T. Ono: Phys. Rev. Lett. **102** (2009) 147202.

[60] K. Sekiguchi, K. Yamada, S.-M. Seo, K.-J. Lee, D. Chiba, K. Kobayashi, and T. Ono: Phys. Rev. Lett. **108** (2012) 017203.

[61] J.-Y. Chauleau, H. G. Bauer, H. S. Körner, J. Stigloher, M. Härtinger, G. Woltersdorf, and C. H. Back: Phys. Rev. B **89** (2014) 020403.

[62] A. Roldán-Molina, A. S. Nunez, and R. A. Duine: Phys. Rev. Lett. **118** (2017) 061301.

[63] D.-H. Kim, S.-H. Oh, D.-K. Lee, S. K. Kim, and K.-J. Lee: Phys. Rev. B **103** (2021) 014433.